Ferromagnetic Resonance of Magnetite Films and Iron Nanowires

L. McGuigan

August 17, 2010

Abstract

Ferromagnetic resonance (FMR) measurements were carried out at 9.6 GHz on thin magnetite films and iron nanowire arrays, produced by molecular beam epitaxy (MBE). The aims of the studies were to examine how the magnetic anisotropy is affected by film thickness, the deposition substrate material, post-deposition annealing, and deposition on a stepped substrate. For films deposited on MgO, we found that the cubic anisotropy field, $H_{4||}$, decreased with an increase in film thickness. This decrease was accompanied by an increase in the mean FMR peak-to-peak linewidth, which indicates a decrease in the film quality. $H_{4||}$ was seen to increase after annealing for just 4 minutes in air at 250°C, with this change being accompanied by a significant decrease in the linewidth. We propose that the annealing treatment is altering the defects within the films, and increasing the magnetic ordering. A further anneal of 156 minutes did not affect the observed $H_{4||}$, and the linewidth was seen to decrease only a little further. For all magnetite films deposited on $MgAl_2O_4$, we found the easy axis of magnetisation lie along [010] type directions as opposed to the expected [110] type directions. The cause of this unexpected result is not immediately apparent. Again, we propose that the film with higher cubic anisotropy is of better quality, as is shown by the quality of the FMR signal observed. $H_{4||}$ again increased after annealing - however, in this case, almost no change is observed after 5 minutes annealing in air at 250°C, whereas a large increase in $H_{4||}$ is observed after 160 minutes annealing. Similarly, the greatest change in linewidth is observed after 160 minutes of annealing. This suggests that the annealing treatment is again having an effect on the film quality, but that more extensive annealing is required to improve the quality of films on $MgAl_2O_4$ than is required for films on MgO. We propose that this is due to the difference in the type of defects likely to be present. For films of magnetite deposited on vicinal MgO, we found that the stepped structure of the substrates induced an in-plane uniaxial anisotropy, with easy axis parallel to the step edge. The strength of this anisotropy was observed to increase with the substrate miscut angle, and to increase with a decrease in film thickness. We propose that the induced anisotropy is associated with antiphase boundaries (APBs) preferentially aligned with the step edges. We found arrays of Fe nanowires deposited on stepped sapphire substrates exhibited a uniaxial anisotropy with axis within the plane of the array, but perpendicular to the wires – this axis being is a hard axis of magnetisation. The magnitude of the anisotropy field, was found to be almost equal for all samples investigated, despite differences in wire width and spacing. We suggest that this originates at the step edges at the substrate-iron interface.

Declaration

The work contained in this thesis has not been submitted as an exercise for a degree at this or any other university. It is entirely my own work, apart from that presented in Section 4.4.1, which is acknowledged in the text. The library is free to lend or copy the thesis as is seen fit.

Louise McGuigan

Summary

Ferromagnetic resonance (FMR) measurements were carried out at 9.6 GHz on a number of magnetite films and iron nanowire arrays, with the aim of characterising the magnetic anisotropy of the samples investigated. All films and nanowires were produced by members of Prof. Shvets group in Trinity College, and all of the FMR measurements were conducted in Dr. Barklie's laboratory in Trinity College, except where otherwise indicated.

The aims of the studies on magnetite films were to examine how the magnetic anisotropy is affected by a number of different factors, namely the film thickness, the deposition substrate material, post-deposition annealing, and deposition on a stepped substrate. To achieve these, we investigated three sets of films, all of which were produced by molecular beam epitaxy (MBE). The first set were deposited on flat MgO and $MgAl_2O_4$ substrates, with thickness in the range 5nm to 700nm. The second set consisted of 100nm thick films, again deposited on flat MgO and $MgAl_2O_4$ substrates, which were annealed in air after deposition for periods between 4 and 160min. The third set were 30 and 70nm thick, deposited on substrates of MgO miscut by between 3° and 10°.

We found that the cubic anisotropy of the films was greatly affected by the film's quality, with a higher anisotropy being observed for films of better quality. In the study of films of different thickness, for the samples deposited on MgO, we found that the cubic anisotropy field, $H_{4||}$, decreased from -315 Oe to -75Oe with an increase in film thickness from 38 to 700nm. This decrease was accompanied by an increase in the mean FMR peak-to-peak linewidth, which indicates a decrease in the film quality. For films of 100nm thickness, $H_{4||}$ was seen to increase from -93 Oe to -278 Oe after annealing for just 4 minutes in air at 250°C, with this change being accompanied by a significant decrease in the linewidth. Again we propose that the increase in $H_{4||}$ is related to an increase in film quality, as is indicated by the reduction in linewidth. Thus, we propose that the annealing treatment is altering the defects within the films, and increasing the magnetic ordering. A further anneal of 156 minutes did not affect the observed $H_{4||}$, and the linewidth was seen to decrease only a little further.

For the films deposited on $MgAl_2O_4$, we found one startling result, which was a change in the easy axis of magnetisation from [110] type directions (as was observed for the films on MgO, and as is expected) to [010] type directions. This was observed for all of the films examined with $MgAl_2O_4$ substrate, and its cause is not immediately apparent. We found that, in this case, the thinnest film exhibited the lowest magnitude of $H_{4||}$, with an increase from 85 to 168 Oe being observed with an increase in thickness from 5nm to 33nm. Again, we propose that the film with higher cubic anisotropy is of better quality, as is shown by the quality of the FMR signal observed. For the 100nm films, we again observe an increase in anisotropy after annealing - however, in this case, almost no change is observed after 5 minutes annealing in air at 250°C, whereas an increase in $H_{4||}$ from 112 to 330 Oe is observed after 160 minutes annealing. Similarly, the linewidth shows only a small change after 5 minutes annealing, but decreases significantly after 160 minutes of annealing. This suggests that the annealing treatment is again having an effect on the film quality, but that more extensive annealing is required to improve the quality of films on $MgAl_2O_4$ than is required for films on MgO. We propose that this is due to the difference in the type of defects likely to be present in the two types of films.

In our study of films deposited on vicinal substrates, we found that the stepped structure of the substrates did induce an in-plane uniaxial anisotropy, with easy axis parallel to the step edge. The strength of this anisotropy was observed to increase with the substrate miscut angle, and to increase with a decrease in film thickness. We propose that the induced anisotropy is associated with antiphase boundaries (APBs) preferentially aligned with the step edges. A second, weaker, in-plane uniaxial anisotropy is present in the film on the 10° miscut substrate, which we attribute to an uneven step edge configuration.

The final aim of the studies presented here was to characterise the magnetic anisotropy of arrays of Fe nanowires deposited on stepped sapphire substrates. In order to do this, we examined three nanowire arrays, again produced by MBE. We found the arrays exhibited a uniaxial anisotropy with axis within the plane of the array, but perpendicular to the wires – this axis being is a hard axis of magnetisation. The magntiude of the anisotropy field, H_Z, was found to be -16.1 $\pm$ 0.4 kOe for all samples investigated, despite differences in wire width and spacing. It is unclear whether this effect is caused by dipolar interactions between the wires or by the step edges at the substrate-iron interface, and we suggest that further study is necessary.

Acknowledgments

I would firstly like to thank my supervisors, Dr. Robert Barklie and Prof. Igor Shvets for all of their help and support through my time in the School of Physics, and for the great opportunities they have given me.

I would like to thank Trinity College, SFI and PRTLI for providing the funding for my work, and the School of Physics for being my host for so many years.

I would like to thank all of the members of Prof. Shvets research group for their help with my research, especially Yang Zhou, Sunil Arora, Sumesh Sofin and Floriano Cuccureddu for producing the samples for me to study.

I would like to extend special thanks to Sandra Wright for keeping me company in the lab over my time there, and for all of her help with my work.

Finally, I would like to thank my friends and family for all of their support over the years.

Conversion factors - CGS and SI Units

Given below is a table of conversion factors, as a reference for conversion between cgs and SI units for the magnetic quantities referred to in the text.

Magnetic Term	cgs Unit	SI Unit	Conversion
Magnetic field (**B**)	Gauss (G)	Tesla (T)	1 G = 10^{-4} T
Field intensity (**H**)	Oersted (Oe)	A/m	1 Oe = 1-$^3/4\pi$ A/m
Magnetic moment (**m**)	emu	Am^2	1 emu = 10^{-3} Am^2
Magnetisation (**M**)	emu/cm^3	A/m	1 emu/cm^3 = 10^3 A/m

Contents

Chapter 1

Introduction

In this thesis we present a ferromagnetic resonance study on thin magnetite films and iron nanowires. We will examine three sets of magnetite (Fe_3O_4) films, all of which were deposited by molecular beam epitaxy (MBE). We also examine one set of iron (Fe) nanowires, deposited on stepped sapphire substrates using the ATLAS procedure as described later in the thesis. In each case we use the ferromagnetic resonance (FMR) response of the samples as a function of the direction of the applied field to characterise the magnetic anisotropy of the sample. All films and nanowires were produced by members of Prof. Shvets group in Trinity College, and all of the FMR measurements were conducted in Dr. Barklie's laboratory in Trinity College, except where otherwise indicated.

Magnetite has, for many years, been of great scientific interest due to its interesting magnetic properties. It has a wide range of technological applications including uses in the cores of electromagnets, in computer memory cores, and in high density recording media. The field of spin electronics has been the subject of much recent study [1–4]. Magnetite's 100% spin polarisation and relative ease of production means that it has great potential for uses in spin electronics [5–8] and so, many studies have been carried out on the production and characterisation of thin films of magnetite [9–21]. Magnesium oxide (MgO) and spinel ($MgAl_2O_4$) are commonly used as substrates for the deposition of these films [9,12,13,16–23] as their oxygen sublattice dimensions both match that of magnetite to within 4%.

These possible technological applications are the motivation for the studies presented in this thesis - if magnetite thin films are to be successfully utilised in nanoscale devices, it is necessary that all of their magnetic properties be accurately characterised. It is also of technological interest if these magnetic properties can be manipulated, and so we investigate how they are affected by deposition substrate, and by post-deposition treatment.

The first aims of this study were to examine how the magnetic anisotropy of thin magnetite films is affected by the film thickness, and the deposition substrate. We did this by examining a set of five films of different thicknesses in the range 5nm to 700nm, deposited on flat MgO and $MgAl_2O_4$ substrates. The second set of samples studied consisted of six films, again deposited on flat MgO and $MgAl_2O_4$ substrates but all of 100nm thickness, which were annealed in air after deposition for periods between 4 and 160min. The aim of this set of experiments was to examine how post-deposition annealing affects the film's magnetic anisotropy, and also to examine whether the deposition substrate had any impact on this. The third set of samples consisted of five films, of thickness between 30 and 70nm, deposited on substrates of MgO miscut by between 3 and 10 degrees. The aim in examining these films was to see whether depositing magnetite on a stepped substrate would induce a uniaxial anisotropy, and to examine whether this anisotropy was affected by the film thickness or miscut angle.

We found that the cubic anisotropy of the films was greatly affected by the degree of magnetic ordering present, which we relate to the FMR linewidth. A film of higher quality (that is, a film possessing fewer defects such as antiphase boundaries, or misfit dislocations, as described later), should have a higher degree of magnetic ordering, and so should exhibit a narrower FMR linewidth. We found, in the study of films of different thickness, for the samples deposited on MgO, that the cubic anisotropy field, $H_{4||}$, decreased with an increase in film thickness. This decrease was accompanied by an increase in the mean FMR peak-to-peak linewidth, which indicates a decrease in the film quality. For the 100nm films studied, $H_{4||}$ was seen to increase after a short anneal in air (4 minutes at 250°C), with this change being accompanied by a significant decrease in the linewidth. Again we suggest that this linewidth behaviour is evidence of an increase in magnetic ordering, being brought about by the annealing treatment.

For the films deposited on $MgAl_2O_4$, we found one startling result, which was a change in the easy axis of magnetisation from [110] type directions (as was observed

for the films on MgO, and as has been observed previously [9,12]) to [010] type directions. This was observed for all of the films examined with $MgAl_2O_4$ substrate. Again in this case we found that the value of $H_{4||}$ increased with a decrease in the observed FMR linewidth. In this case however, we found the lowest value of $H_{4||}$ was exhibited by the thinnest film. For the 100nm films, we again observe an increase in anisotropy after annealing - however, we found that more extensive annealing is required to improve the quality of films on $MgAl_2O_4$ than is required for films on MgO. We propose that this is due to the difference in the type of defects likely to be present in the two types of films.

We were also interested in the question of whether an addition anisotropy field could be induced by depositing films on a stepped substrate. We found that the stepped structure of the substrates did in fact induce an in-plane uniaxial anisotropy, with easy axis parallel to the step edge. The strength of this anisotropy increased with an increase in the substrate miscut angle, with a decrease in film thickness. We propose that the induced anisotropy is associated with antiphase boundaries (APBs) tend to align along the step edges. A second, weaker, in-plane uniaxial anisotropy is present for higher miscut angle, which we attribute to an uneven step edge configuration.

The fabrication of metallic nanowires has become an extremely popular topic for scientific research [24–29], [30–34] due to their many potential uses in nanotechnology. One-dimensional systems are of particular interest [35], and a new method of producing such arrays has been produced by members of Prof Shvets group, namely the ATLAS method [24,36]. We examine three such nanowire arrays, which consist of 1-2nm high wires deposited on stepped sapphire substrates, with the aim of extracting the magnetic anisotropy of the systems. In each case, we find an extremely large uniaxial anisotropy, with axis within the plane of the array, but perpendicular to the wires. The magnitude of the associated anisotropy field is not affected by wire spacing. We suggest that this effect is caused by the step edges at the substrate-iron interface, and we suggest that further study is necessary.

The outline of the thesis is as follows. We will begin with a chapter giving detailed background information on all of the materials studied, and on the production of the samples investigated. In chapter 3, we will provide a thorough description of the the theory of FMR, and a derivation of the theoretical model used in the analysis of our experimental results. In chapters 4 to 7, we present our experimental results, as outlined above, along with detailed analysis and discussion of the extracted results. In the final chapter, chapter 8, we will provide a final overview of the experimental results, along with the conclusions reached.

Chapter 2

Magnetite Films and Iron Nanowires: Properties and Preparation

2.1 Introduction

Magnetic thin films and nanowires have for many years been of scientific interest, due to their interesting magnetic properties, and their potential for use in nanoscale devices. In this thesis, we present the results of FMR studies on thin films of magnetite, and on nanowires of iron. In this chapter, we will provide a detailed description of the materials investigated, along with details of the production of the samples investigated.

In Chapters 4, 5 and 6, we present FMR studies on magnetite films deposited by molecular beam epitaxy (MBE) on substrates of MgO and $MgAl_2O_4$. We will therefore begin this chapter with a detailed description of magnetite and its properties, followed by details of the substrates used, a description of the defects likely to be present in magnetite thin films, and details of the deposition procedure.

In Chapter 7, we present FMR studies on nanowires of iron deposited on vicinal sapphire using the ATLAS procedure. In Section 2.3 of this chapter, therefore, we will provide a description of both iron and the sapphire substrate, and details of the deposition method.

2.2 Magnetite films on MgO and $MgAl_2O_4$

2.2.1 Magnetite

Magnetite is a naturally magnetic oxide of iron, with formula Fe_3O_4. More specifically, the formula can be written $Fe^{3+}(Fe^{2+}Fe^{3+})O_4$, and the structure is inverse spinel, as shown in Figure 2.1 (space group $Fd\bar{3}m$). The unit cell contains 32 O^{2-} anions in face centered cubic (FCC) configuration. There are eight formula units per unit cell. The Fe cations are arranged between 8 A sites (with tetrahedral configuration with the oxygen), and 16 B sites (with octahedral configuration with oxygen). The A sites are occupied solely by Fe^{3+} ions, whereas half of the the occupied B sites are occupied by Fe^{2+} and half by Fe^{3+}. Thus, 1/8 of the A sites are occupied, and 1/2 of the B sites. The lattice constant, a, is 8.3963Å. As can be seen in Figure 2.1, there are 4 oxygen sublattice layers within the unit cell. The arrangement of atoms in a cross section of the bulk is illustrated in Figure 2.2. The cross section is taken along one layer of the oxygen sublattice, with Figure 2.2(b) illustrating the layer directly above/below that shown in Figure 2.2(a) (layers are numbered 1 to 4 from the bottom of the diagram in Figure 2.1). The octahedral and tetrahedral arrangements are described in the captions.

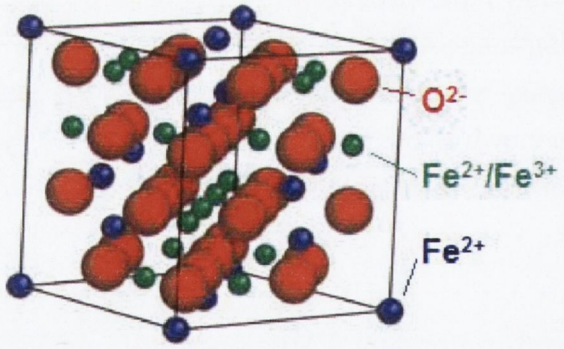

Figure 2.1: Structure of one magnetite unit cell. The red spheres represent oxygen atoms. The green spheres represent B-site Fe ions, octahedrally configured with oxygen. These sites are populated half by Fe^{+3} and half by Fe^{+2} ions. The blue spheres represent A-site Fe ions, tetrahedrally configured with oxygen. These sites are populated solely by Fe^{+3} ions.

The Fe spins in the inverse spinel configuration of magnetite show ferrimagnetic order. Magnetic exchange interactions between the 3d Fe cations are antiferromagnetic superexchange couplings, via the the intervening O anion p orbital. This exchange would be strongest if the three ions were colinear [23]. In the spinel structure, the

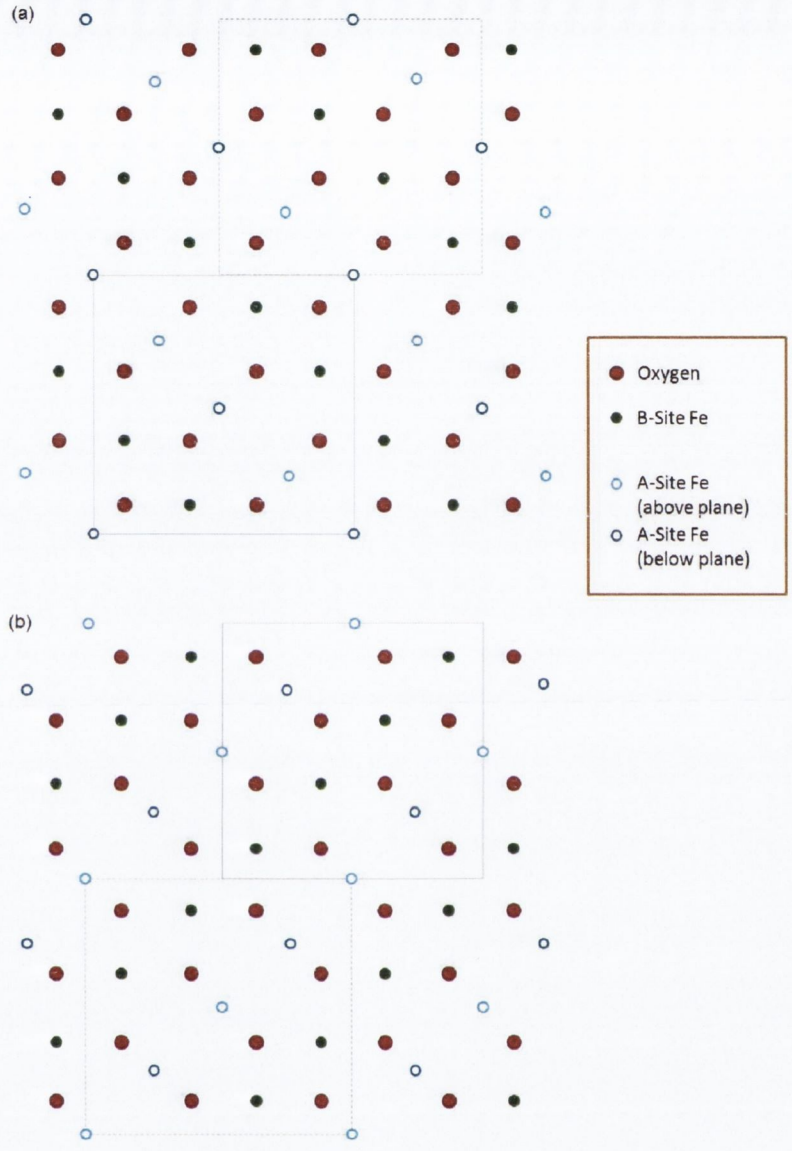

Figure 2.2: Atomic configuration within magnetite bulk, with cross section taken across one plane of the oxygen sublattice - figures (a) and (b) show layers 1,3 and layers 2,4 respectively. The full red circles represent oxygen atoms, which are arranged in FCC configuration. The full green circles represent the B-site Fe ions, which lie within the oxygen plane, and are coupled in octahedral arrangement with 6 oxygen atoms (with the 4 nearest neighbours in the plane, and with 2 further nearest neighbours directly above and below). The open blue circles represent the A-site Fe ions, which lie 1/2 of the oxygen lattice spacing above and below the oxygen plane. They are coupled in tetrahedral arrangement with 4 oxygen atoms (2 nearest neighbours in the plane above and 2 in the plane below). In (a) the grey lines show the magnetite unit cell, layer 1, and the grey dashed lines show the magnetite unit cell, layer 3. In (b) the grey lines show the magnetite unit cell, layer 2, and the grey dashed lines show the magnetite unit cell, layer 4.

A-O-B bond angle is 125^o and the B-O-B bond angle is 90^o (there are no A-O-A bonds). Since the number of Fe^{3+} ions is split evenly between A sites and B sites, their exchange is strong and purely antiferromagnetic, and so their moments cancel each other out. This leaves the $4\mu_B$ moment of the Fe^{+2} as the total moment per formula unit.

Above 120K, magnetite is a half metallic ferromagnet (HMFM) and thus shows 100% spin polarisation. It has a high Curie temperature of 858K [37]. At room temperature, its electrical conductivity is approximately 200 $\Omega^{-1}cm^{-1}$.
Bickford's original FMR study of magnetite single crystals [38] found synthetic crystals of magnetite to have a g-factor of 2.12, first order cubic anisotropy constant K_1 of -1.10 x 10^4 joule/m^3 (-1.10 x 10^5 erg/cm^3) and saturation magnetisation of 4.6 x 10^5 amp/m (460 emu/cm^3). At a temperature of 120K, bulk magnetite exhibits a metal-insulator transition, known as the Verwey transition [39], below which its conductivity decreases by some two orders of magnitude. This transition is associated with a lattice distortion from cubic to monoclinic.

When producing thin films of magnetite, it is imperative that the crystalline structure of the substrate be as close as possible to that described above, in order to preserve the magnetite structure and reduce mismatch induced defects as much as possible. Two commonly used substrates are MgO and $MgAl_2O_4$, whose oxygen sublattices match that of magnetite to within 4%. However, even this small mismatch leads to a number of lattice defects, as we will describe in the next section.

2.2.2 Substrates - MgO and $MgAl_2O_4$

MgO and $MgAl_2O_4$ (or MAO) are both well suited for use as substrates for the deposition of magnetite films due to the close matching of their oxygen substructures with that of magnetite, and both have been used successfully for the production of thin films in a number of previous studies [9–18].

MgO is simply an oxide of magnesium, with two point basis in face centered cubic configuration (space group $Fm\bar{3}m$). The structure is a simple rock salt crystal structure. The oxygen lattice constant is 4.21 Å. Comparing this to magnetite (oxygen lattice constant 8.39Å) gives lattice mismatch of +0.3%.

The chemical formula for MAO (also known as spinel) is $MgAl_2O_4$. It has spinel

structure, similar to that of magnetite, but with Mg^{+2} on A sites (tetrahedral configuration with O) and Al^{+3} on B sites (octahedral configuration with O). The oxygen lattice constant is 8.08Å, which gives lattice mismatch of -3.8% with magnetite (oxygen lattice constant 8.39Å). Its space group is $Fd\bar{3}m$.
Neither MgO nor MAO have exact lattice matching with magnetite, but both are quite close (within 4%). However, due to the differences in lattice mismatch, films deposited on the two substrates can be expected to have very different properties.

The mismatch between the oxygen sublattice in magnetite and MgO (+0.3%) is less than one tenth of the mismatch between magnetite and MAO (-3.8%). This means that the strain involved in maintaining a 1:1 fit with the substrate is much higher in the case of a film deposited on MAO than it would be for a film on MgO. When the deposited film reaches a certain critical thickness, t_c, strain reaches critical levels, and will be relaxed within the film by the formation of misfit dislocations, disturbing the crystalline structure of the film.

However, the oxygen lattice constant of MgO is approximately half that of magnetite and this can lead to the the formation of antiphase boundaries - a defect formed within magnetite due to symmetry breaking in iron sublattice. In contrast, the structure and lattice constant of MAO are very similar to those of magnetite, and so this sort of symmetry breaking is much less likely. In the next section, we will discuss in detail the formation of these antiphase boundaries, and their effects on the properties of the films in which they are present.

2.2.3 Mismatch Induced Defects

Due to the fact that magnetite possesses higher symmetry in the oxygen sublattice than in the iron sublattice, a common defect seen in the material is the antiphase boundary (APB) [23,40,41]. At these boundaries, the oxygen substructure is unaffected, but the iron substructure is displaced, altering the magnetic exchange interactions. The normal ferromagnetic order is disturbed, with antiferromagnetic and frustrated exchange dominating at the boundary. As shown by Margulies et.al [23] intrasublattice exchange dominates across the boundaries and thus they separate oppositely magnetised regions.

Magnetite's oxygen sublattice possesses both rotational and translational symmetry - more specifically, it can be rotated by any multiple of 90° or translated in a num-

ber of ways, and remain unaffected. However, for the iron sublattice, this is not the case - it is only left unchanged by a 180° rotation, or translation by one full lattice constant in any of [100], [010] or [001] directions.

Magnetite films such as those investigated in this study grow in layer-by-layer fashion [18]. Formation begins by the growth of individual islands. These islands then merge to form the base layer, with subsequent layers growing on top of this. As the lattice constant of MgO is approximately one half the lattice constant of magnetite, its oxygen substructure corresponds almost 1:1 with that of magnetite, and so the islands can form translated or rotated in any of the ways mentioned above relative to the other neighbouring islands. At their joining point, if the structure of the islands does not match, an antiphase boundary is formed [42]. These can produce a number of APB configurations, illustrated in Figures 2.3 and 2.4. In these figures only the oxygen and B-site Fe ions within a given oxygen sublayer are shown. The configuration shown in Figure 2.3 is the rotational type of APB – Figure 2.3(a) shows the APB aligned along the $[01\bar{1}]$ direction, while Figures 2.3(b) and 2.3(c) show two possible configurations where the APB is aligned along the [011] direction. Figure 2.4 shows the translation type APBs – two possible types are shown in Figures 2.4(a) and 2.4(b), both aligned along the $[01\bar{1}]$ direction.

As was mentioned earlier, magnetic exchange interactions between the Fe cations are via the intervening oxygen atoms and are antiferromagnetic in order, and are strongest if the three ions were colinear. Examining Figures 2.3 and 2.4 we can see that the reordering across the APBs introduces B-O-B bonds with angle 180° i.e. strong antiferromagnetic exchange not seen elsewhere in the undisturbed bulk structure.

Due to the presence of APBs, the properties of thin magnetite films differ significantly from those of the bulk. They exhibit increased magnetoresistance (MR) [16,43], larger electrical resistivity [44] and most significantly for this study, the magnetisation is found not to saturate even in high fields [23]. Films below 5nm in thickness show superparamagnetic behaviour [22]. These properties have been attributed to the frustrated exchange across the APBs and high density of oppositely magnetised domains in the material.

It has been reported [11,18] that thin films of magnetite grown on MgO remain fully strained up to thicknesses of 700nm - far greater than the critical thickness (t_c) of 60

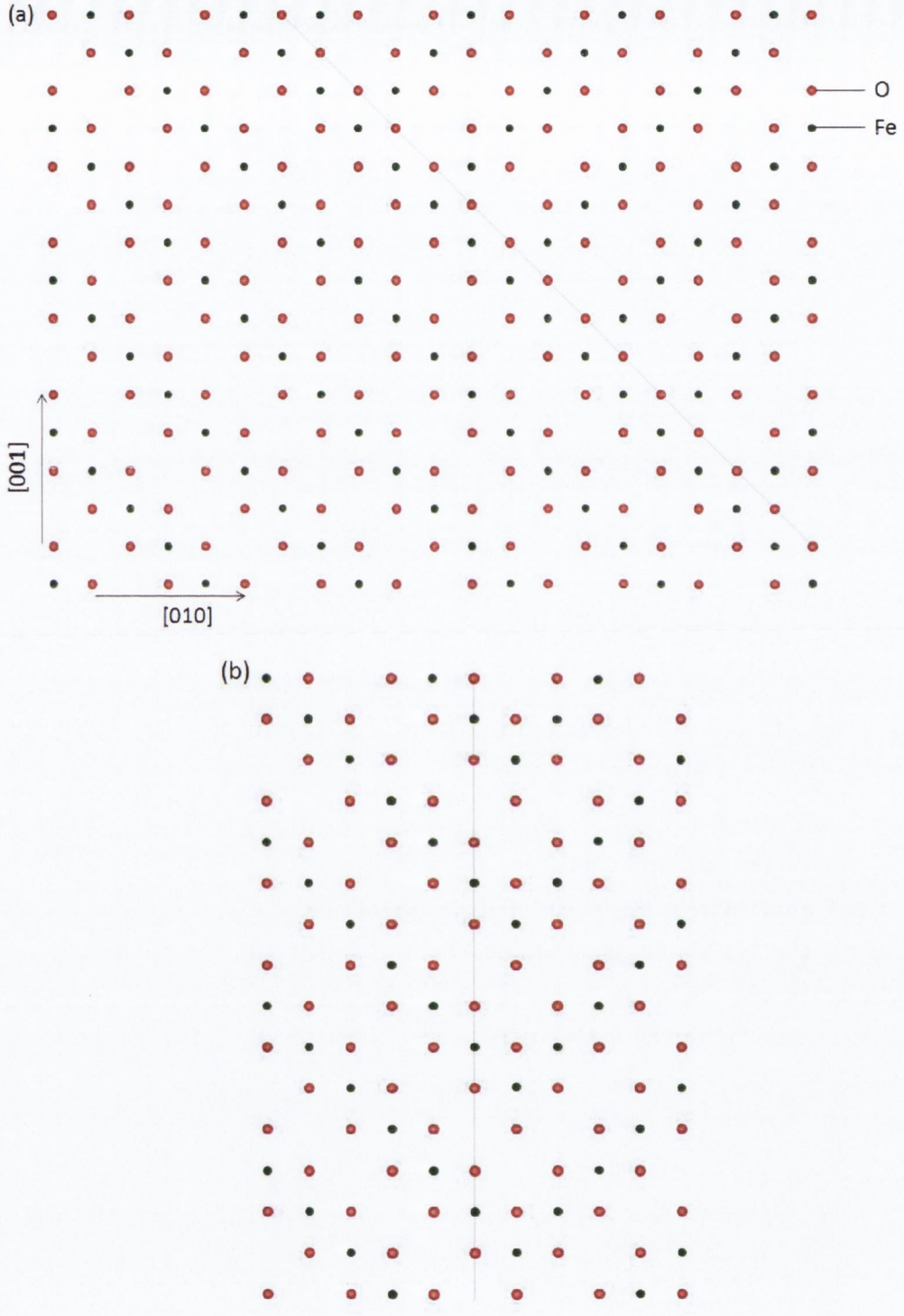

Figure 2.3: Atomic configuration along rotation type APBs, with cross section taken across one plane of the oxygen sublattice. The red circles represent oxygen atoms, and green circles represent the B-site Fe ions. Antiphase boundaries are shown by the grey lines. Image (a) shows an APB directed along $[01\bar{1}]$ direction, while image (b) shows an APB directed along [001] direction.

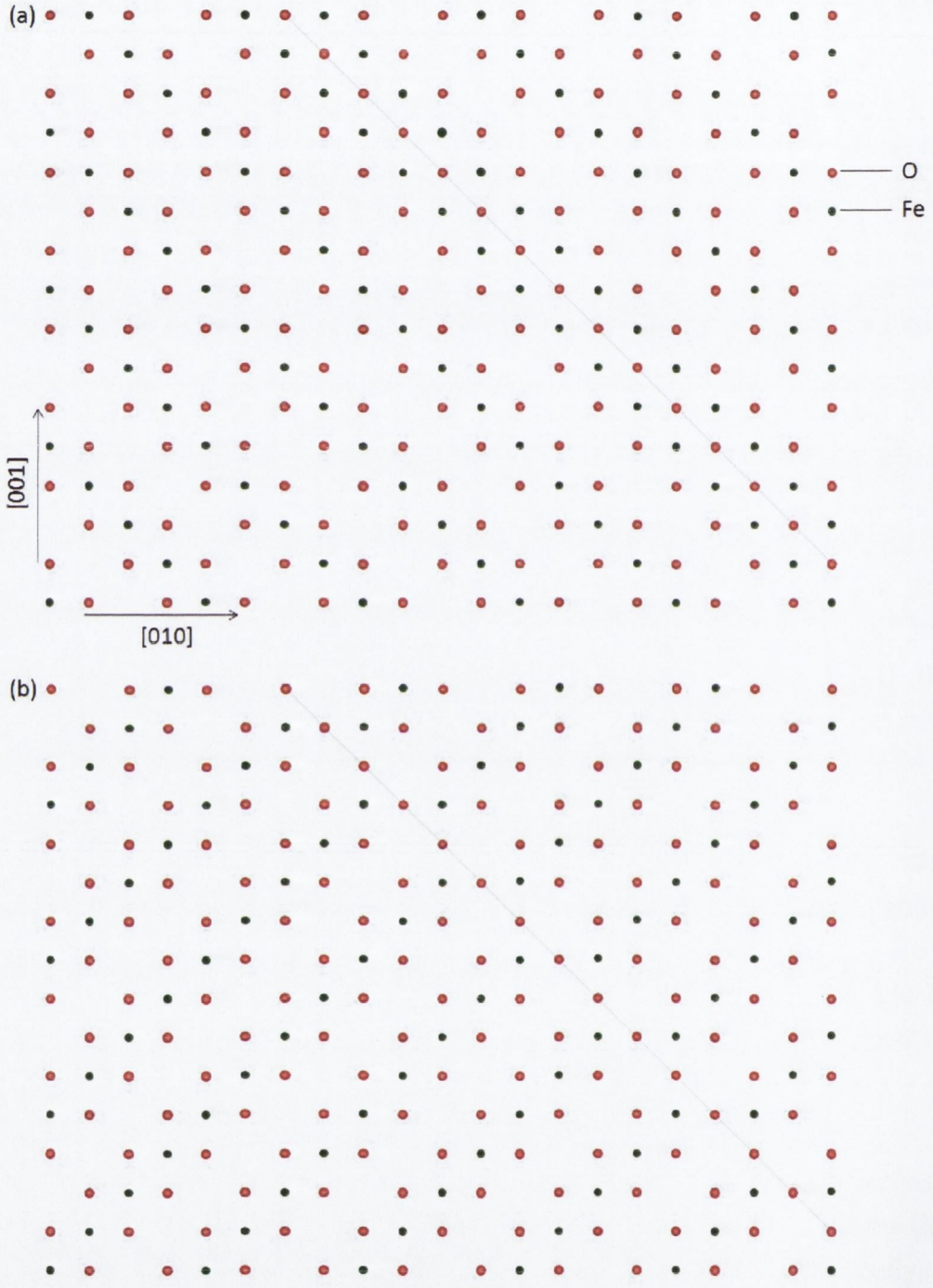

Figure 2.4: Atomic configuration along translation type APBs, with cross section taken across one plane of the oxygen sublattice. The red circles represent oxygen atoms, and green circles represent the B-site Fe ions. Antiphase boundaries are shown by the grey lines. Images (a) and (b) show 2 configurations for APBs directed along $[01\bar{1}]$ direction.

nm estimated from the mismatch strain [18]. This phenomenon is attributed to the presence of APBs in the film. It is suggested that compressive strain generated by the APBs compensates for the tensile strain within the growth islands, allowing the film to remain fully coherent with the substrate. This, however, would not be the case for films deposited on MAO. Due to the higher substrate mismatch and much lower density of APBs in this system, it is to be expected that significant strain relaxation would occur, as was found in studies on pulsed laser deposited films of thickness 300-2000Å [12].

2.2.4 Molecular Beam Epitaxy

The magnetite films used in this study were deposited by oxygen plasma assisted molecular beam epitaxy (MBE), as is described in [16] and [19]. The films were all produced by members of Prof. Shvets' group in TCD.

Metallic iron is evaporated in the presence of free oxygen radicals, combining to form Fe_3O_4 which is then deposited on the substrate. The iron is evaporated by electron beam evaporation, and the oxygen plasma is produced by electron cyclotron resonance (ECR).

For these films, the substrates were cleaned chemically before being placed in the growth chamber, then cleaned in situ at 600°C in UHV for 1hr, followed by annealing in 10^{-5} Torr oxygen for another 6 hours. Metallic Fe of purity 99.999% was used, with the ECR source operating at 80W in an oxygen atmosphere of 10^{-5} Torr. Conditions for deposition were a substrate temperature of 250°C and base pressure $5x10^{-10}$ Torr. Growth mode and crystalline quality of the films were monitored in situ by reflection high energy electron diffraction (RHEED). Film thickness was controlled by quartz crystal thickness monitors, calibrated using X-ray reflectivity (XRR). RHEED results suggest that the films grow epitaxially in layer by layer mode, at 0.3Å/s. All films were deposited on substrates cut in the (100) plane (edges [010] and [001]).

2.3 Iron Nanowires on Sapphire

2.3.1 Iron

Iron is a transition metal element, with atomic number 26 (group 8 and period 4). Iron and iron alloys (steels) are by far the most common metals and the most common ferromagnetic materials in everyday use. Pure iron is a metal but is rarely found in this form on the surface of the earth because it oxidizes readily in the presence of oxygen and moisture. Its outer electron configuration is $3d^6\ 4s^2$. It is a solid below 1811K, and at room temperature crystallizes in a body centered cubic (BCC) structure, with lattice parameter of = 2.87Å.

In recent years there has been increasing interest in the production and properties of nanostructured materials, motivated by their potential applications in the fabrication of nanoscale devices. Iron is a desirable material to investigate for these purposes, as it is both conducting and magnetic. One way of forming one-dimensional structures is to use a stepped substrate, as was originally suggested by Basset [45] and Bethge [46]. This idea has been extended to form the ATLAS procedure (Atomic-Terrace Low-Angle Shadowing), which was formulated by members of Prof. Shvets group in TCD, and has successfully been used to produce arrays of nanowires of different metals [36]. This procedure is explained in detail in section 2.3.3

The substrate used to produce the nanowires examined for this thesis was miscut sapphire, and so in the next section we will present a description of this material, and of the production of the stepped substrate used for the nanowire deposition.

2.3.2 Sapphire

Aluminium (III) oxide is an amphoteric oxide of aluminium with the chemical formula Al_2O_3, commonly known as sapphire. It has hexagonal crystal structure, (a = 4.758Å and c = 12.991Å) with rhombohedral primitive cell and space group $R\bar{3}c$. The primitive cell contains two formula units of aluminum oxide. The oxygen ions nearly form a hexagonal close-packed structure with aluminum ions filling two-thirds of the octahedral interstices.

Planes within the hexagonal structure are defined in terms of 4 unit vectors, $\vec{a_1}$, $\vec{a_2}$,

$\vec{a_3}$ and $\vec{c}$ as shown in Figure 2.5. Planes within the structure are defined in terms of these four indices - the example of c-plane (0001) is shown in the diagram.

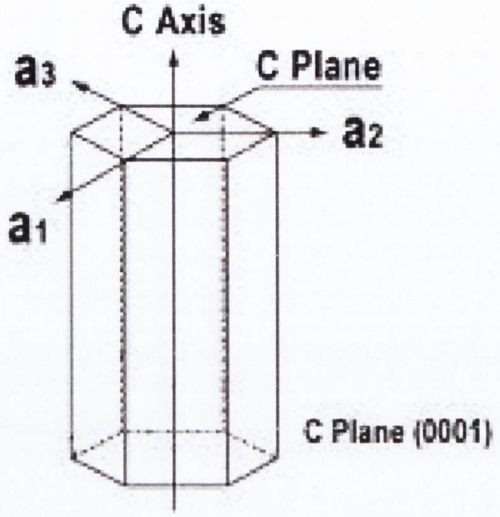

Figure 2.5: Hexagonal crystal structure, as that of sapphire (Al_2O_3). Unit vectors $\vec{a_1}$, $\vec{a_2}$, $\vec{a_3}$ and $\vec{c}$ are shown, and the c-plane (0001) is indicated.

Vicinal surfaces can be formed by annealing a surface that is off cut from a low-index orientation [47]. The vicinal surface will then consist of atomic terraces separated by steps, with the terrace width being controlled by the miscut angle. The substrates used for deposition of the Fe nanowires were vicinal Al_2O_3 miscut by 3° off the (0001) plane along the $[1\bar{2}10]$ direction. The substrates were annealed in air at 1100°C for 6-12 hours to produce the stepped surface [36]. The surface topography is characterised by a staircase arrangement of 30-80nm wide terraces with a step height of 2-4nm (private communication from Floriano Cuccureddu). These substrates were subsequently deposited with iron to form nanowire arrays, with the method used for production explained in the next section.

2.3.3 ATLAS Procedure

The iron nanowire arrays studied were produced by the ATLAS procedure (Atomic-Terrace Low-Angle Shadowing) [24,36]. In this technique, the atomic step-and-terrace morphology of vicinal substrates is used to produce a shadowing effect on a highly collimated molecular beam at an oblique incidence to the substrate.

A highly collimated beam is achieved by placing the stepped substrate a large working distance from the evaporation source (370-800mm). The deposition system is a

100mm diameter stainless steel ultrahigh vacuum (UHV) chamber. The base pressure is of the order of 10^{-10} Torr. The primary source is a 10 cc high-temperature effusion cell. The sample is mounted at the main focal point of the chamber and can be tilted through 200° with a precision of ±0.5°. The sample is mounted onto to Ta electrode, and is heated by driving a current through the Ta foil beneath it.

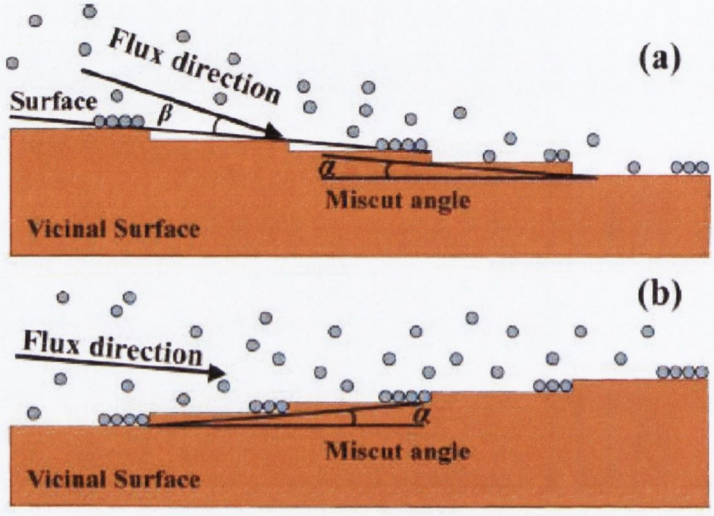

Figure 2.6: Schematics for deposition of nanowires on vicinal substrate (miscut by angle α) using the ATLAS techniques. Two methods are illustrated; (a) deposition of nanowires on the outer step edges. Here the molecular beam is directed in descending step direction, at angle β to the surface. (b) deposition of nanowires on inner step faces. Here the molecular beam is directed in ascending step direction.

In the ATLAS approach, wires can be grown in two ways, as illustrated in Figure 2.6 (reproduced from [36]). For the first method, shown in Figure 2.6(a), a collimated beam of evaporated atoms is directed in descending step direction at angle β to the vicinal surface (as illustrated). The angle β is in the range 1-3°. In this way, the outer edges of the atomic terraces are exposed to the beam, while the inner regions are geometrically shadowed by the atomic steps, and so material only grows along the terrace step edges.

For the second method, shown in Figure 2.6(b), the evaporated atom beam is directed in ascending step direction, nearly parallel to the atomic terraces. The step faces provide the bonding sites and the deposited material grows along the steps similar to the step-flow growth mechanism. This is the method which was used to produce the films we studied.

In our case the iron source was heated to a temperature of 1462°C – this was expected to give a deposition rate of 2.37 Å per minute for normal incidence but the beam was directed up the terrace at only 3° to the level of each terrace and so the actual deposition rate is much less, producing wires of thickness 1-2nm. Further details are given in chapter 7, and in [36].

Chapter 3

Magnetic Resonance

3.1 Introduction

In the presence of a magnetic field, the magnetic moment associated with an electron or nucleus precesses around the direction of the local magnetic field at a particular frequency (the Larmor frequency). If a sample is irradiated with electromagnetic radiation of appropriate polarisation, a resonant absorption of energy by the spin system occurs when the frequency of the electromagnetic radiation is equal to the Larmor Frequency: this is magnetic resonance. The terms NMR, EPR (or ESR) and FMR are used when the magnetic moments are associated with nuclei, unpaired electrons that do not exhibit long-range magnetic ordering, and electrons that are coupled as a ferro- or ferri-magnet respectively.

There are two main differences between EPR and FMR. In the case of EPR, the presence of an external magnetic field causes the unpaired electron's magnetic moment to align itself either parallel (m_S = -1/2) or antiparallel (m_S = +1/2) to the field; m_S here is the magnetic quantum number corresponding to a component $m_S\hbar$ of spin angular momentum in the direction of magnetic field $\vec{H}$. At resonance, the magnetic moments are flipped over, corresponding to the transition $\Delta m_S = \pm 1$. This spin flip does not happen in FMR because in the ferro- or ferrimagnet there is a strong exchange interaction between the spins that keeps them parallel and so to induce a change of $\Delta m_S = \pm 1$ in each spin would require a very large change in energy. Instead the spins remain parallel but at resonance precess at a slightly larger angle to the magnetic field. The second major difference is that in FMR there may be strong internal magnetic fields, and these must be added to the external field in deducing the resonance condition.

The layout of this chapter will be as follows. We will first introduce the basic concepts behind magnetic resonance by explaining the phenomenon of Electron Paramagnetic Resonance. We will then describe the phenomenon of Ferromagnetic Resonance and show how the resonance condition is affected by the presence of a demagnetising field and magnetic anisotropy. We also consider the approach of Smit and Beljers [48] in which the resonance condition is derived from the relevant expression for the energy of the spin system; we use this approach to derive the resonance conditions appropriate to the situations dealt with in this thesis. We also consider the factors that can affect the linewidth. Finally we give details of the equipment used and procedures followed in obtaining the FMR spectra.

3.1.1 Electron Paramagnetic Resonance

Many textbooks (such as Abragam and Bleaney [49], Pake and Estle [50]) describe the phenomenon of EPR and therefore only a brief description of the essential features is given here.

When a particle with angular momentum $\vec{G}$ and magnetic moment $\vec{\mu} = -\gamma\vec{G}$ (where γ is positive) is placed in a magnetic field $\vec{H}$ the equation of motion is

$$\frac{d\vec{G}}{dt} = \vec{\mu} \times \vec{H}$$

or

$$\frac{d\vec{\mu}}{dt} = -\gamma\vec{\mu} \times \vec{H} \tag{3.1}$$

where γ is the gyromagnetic ratio.

The solution to this is one in which both $\vec{G}$ and $\vec{\mu}$ precess about $\vec{H}$ with angular frequency $\vec{\omega_L} = \gamma\vec{H}$. To cause $\vec{\mu}$ to flip over it is necessary to apply another magnetic field $\vec{H_1}$ at right angles to $\vec{H}$ that remains in step with $\vec{\mu}$ as as it precesses around $\vec{H}$. This corresponds to a circularly polarised field $\vec{H_1}$ and the resonance condition is

$$\omega = \omega_L = \gamma H \tag{3.2}$$

or

$$\hbar\omega = g\mu_B H \tag{3.3}$$

where ω is the angular frequency of $\vec{H_1}$ and μ_B is the Bohr magneton. g is the g-value - a dimensionless quantity which is the ratio between magnetic moment and spin angular momentum.

The more relevant case is that of an ensemble of magnetic dipoles and for this case the equation of motion is analogous to equation 3.1 with $\vec{\mu}$ replaced by $\vec{M}$, the magnetisation i.e. the net magnetic moment per unit volume, and so

$$\frac{d\vec{M}}{dt} = -\gamma\vec{M} \times \vec{H} \tag{3.4}$$

Resonance is again induced by a field $\vec{H_1}$ with angular frequency $\omega = \omega_L$.

For real samples equation 3.4 must be modified to take account of spin relaxation which attempts to maintain the spin system in thermal equilibrium. Abragam and Bleaney [49] show that under slow passage conditions, when at all times steady-state conditions prevail, $\vec{M}$ precesses around $\vec{H}$ at an angle which, for ordinary values of H_1, is very small even at resonance for which $\tan\theta = (H_1/\Delta H)$; ΔH is the linewidth which is usually much greater than H_1.

3.2 Ferromagnetic Resonance

3.2.1 Motion of the Magnetisation Vector

For a ferromagnetic material the equation of motion for $\vec{M}$, in the absence of relaxation, is the same as for a paramagnetic material, namely

$$\frac{d\vec{M}}{dt} = -\gamma\vec{M} \times \vec{H}$$

and, as before, resonance is induced by the application of a circularly polarised field $\vec{H_1}$ with $\omega = \omega_L = \gamma H$.

The effects of relaxation need to be included and this is done by Landau and Lifshitz [51] in the first phenomenological equation suggested for the motion of the magnetisation of a ferromagnet

$$\frac{d\vec{M}}{dt} = -\gamma\vec{M} \times \vec{H} - \frac{\lambda}{M^2}\left(\vec{M} \times \vec{M} \times \vec{H}\right) \tag{3.5}$$

where λ stands for the relaxation frequency. If $\vec{M} \times \vec{H}$ is replaced by the left hand side of equation 3.4, then the Gilbert equation [52] is obtained

$$\frac{d\vec{M}}{dt} = -\gamma\vec{M} \times \vec{H} + \frac{G}{\gamma M^2}\left(\vec{M} \times \frac{d\vec{M}}{dt}\right) \tag{3.6}$$

where G is the Gilbert damping parameter and has the dimensions of angular frequency. The damping is sometimes expressed in terms of a dimensionless parameter α = G/(γM). Usually $\alpha << 1$ [53] and therefore, the resonance condition is unaffected by damping and remains $\omega = \omega_L = \gamma H$. At resonance, as in EPR, the precession angle θ between $\vec{M}$ and $\vec{H}$ increases slightly but, unlike the situation in a paramagnetic material, the exchange interaction keeps the spins parallel and creates uniform precession spin waves (k = 0 magnons) [54]. Another major difference between EPR and FMR is that the field $\vec{H}$, appearing in the resonance condition $\omega = \gamma H$, usually has a significant contribution from the internal magnetic field arising from the relatively large magnetisation $\vec{M}$; this is referred to as the magnetising field and in the next section we consider how it affects the resonance condition.

3.2.2 The Effect of Demagnetising Fields

To see how the demagnetising field arises consider a ferromagnetic insulator with a uniform magnetisation $\vec{M}$ in an externally applied field $\vec{H}_0$. The existence of $\vec{M}$ gives rise to an additional magnetic field that can in effect be associated with fictitious surface poles and within the sample these give rise to a field - the demagnetising field, $\vec{H}_d$, which tends to oppose $\vec{H}_0$. For an ellipsoid sample the uniform magnetisation produces a uniform demagnetising field. The demagnetising field may be written as

$$\vec{H}_d = -\overleftrightarrow{N}\vec{M} \tag{3.7}$$

where $\overleftrightarrow{N}$ is the demagnetising tensor. For an ellipsoid sample with principal axes x, y and z, $\overleftrightarrow{N}$ becomes diagonal and in cgs units, $N_x + N_y + N_z = 4\pi$ (the sum is 1 in SI units).

To illustrate the effect on the resonance condition of $\vec{H}_d$ we will ignore damping and look for the solution to equation 3.4 with

$$\vec{H} = \vec{H_0} + \vec{H_d} + \vec{H}(t)$$

where the static field $\vec{H_0} = \mathrm{H_0}\hat{k}$ ($\hat{k}$ parallel to z), the demagnetising field $\vec{H_d}$ = -$\mathrm{N}_d\vec{M}$ and $\vec{H}$(t) is the oscillating field that is applied perpendicular to $\vec{H_0}$ and with $\vec{H}$(t) = $\mathrm{H_1 e}^{i\omega t}$. We assume $\mathrm{H_1} << \mathrm{H_0}$. To first order $\mathrm{dM}_z/\mathrm{dt} = 0$ and $\mathrm{M}_z = \mathrm{M}_S$, the saturation magnetisation. Solutions to equation 3.4 with M_x, M_y having the time dependence $\mathrm{e}^{i\omega t}$ can be shown to exist provided

$$\omega_0 = \gamma \left\{ \left[H_0 + 4\pi \left(N_d^y - N_d^z \right) M_s \right] \left[H_0 + 4\pi \left(N_d^x - N_d^z \right) M_s \right] \right\}^{\frac{1}{2}} \tag{3.8}$$

which is Kittel's equation [55].

Table 3.1 lists the resonance condition for some special sample shapes.

Table 3.1: Resonance condition (cgs) for special sample shapes

Sample	Magnetisation Direction	Demagnetising Factors N_x	N_y	N_z	Resonance Frequency
Thin Film	$\perp$ Film	0	0	4π	$\omega_0 = \gamma \left(H_0 - 4\pi M_s \right)$
(x-y plane)	In-Plane	0	4π	0	$\omega_0 = \gamma \left\{ H_0 \left[H_0 + 4\pi M_s \right] \right\}^{\frac{1}{2}}$
Thin Cylinder	$\parallel$ axis	2π	2π	0	$\omega_0 = \gamma \left(H_0 + 2\pi M_s \right)$
axis z	$\perp$ axis	2π	0	2π	$\omega_0 = \gamma (H_0 \left(H_0 - 2\pi M_s \right))^{1/2}$
Sphere		$4\pi/3$	$4\pi/3$	$4\pi/3$	$\omega_0 = \gamma H_0$

Except for those samples containing nanowires, discussed in Chapter 7, FMR measurements were made on thin films with width, w $\approx$ length, l, $\approx$ 5mm and mostly of thickness, t $\leq$ 100 nm but in one case with t = 700nm. We briefly consider to what extent it is a good approximation to use the values given for a thin film in Table 3.1. For the case of $\vec{M}$ in the film plane (x-y), with w = l, O'Handley [56] gives $\mathrm{N}_x = \mathrm{N}_y = 2\mathrm{t}/\pi\mathrm{w}$ and hence for even the thickest film N_x and N_y are only 8.9 x 10^{-5}; therefore the expressions given in Table 3.1 are very good approximations.

Although the anisotropy of the demagnetising field gives rise in general to an angular dependence of the resonance field (at fixed frequency) a more important cause of such angular dependence is the magnetocrystalline anisotropy that is discussed in the next section.

3.2.3 Magnetocrystalline Anisotropy Effects

The energy in a ferromagnetic crystal that directs the magnetisation along certain crystallographic axes — the so-called easy axes — is called the magnetocrystalline anisotropy energy. An illustration of the origin of this anisotropy is given in Figure 3.1. If the electron distribution on an atom is non-spherical and if, through spin-orbit interaction, the orbital orientation is tied to the spin direction, then a change in the direction of the magnetisation will lead to a change in energy as a result of changes in both the exchange energy and the electrostatic interaction of the charge distribution on neighbouring spins.

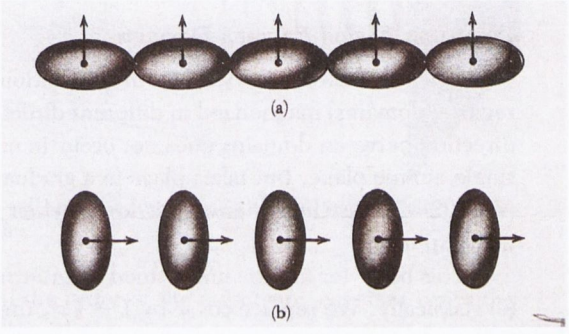

Figure 3.1: Illustration of magnetocrystalline anisotropy. Configurations (a) and (b) will have different energy because of differences in both the exchange and electrostatic interaction energies. Reproduced from Kittel - Introduction to Solid State Physics [57]

Although the magnetocrystalline energy is usually small compared with the exchange energy, it is the former anisotropic energy that determines the direction of magnetisation. Anisotropy energies are written as power series expansions that take into account crystal symmetry. For the case of uniaxial anisotropy, the energy density E can be written as

$$E_K = -K_1 \cos^2\theta - K_2 \cos^4\theta$$

where θ is the angle between the direction of magnetisation and the unique axis. In most cases $K_1 >> K_2$ so that

$$E_K = -K_1 \cos^2\theta$$

If K_1 is positive then the axis of anisotropy is the easy axis of magnetisation. It should be mentioned that the uniaxial energy density may also be written as

$$E_K = -K_1' \sin^2\theta, K_1 \neq K_1'$$

For a more general case (not necessarily uniaxial) the energy can be written in terms of powers of the directional cosines (α_i) of the direction of the magnetisation in relation to the crystal axes [57]. By symmetry, for a cubic crystal this must be in even powers of each α_i. The lowest order is $(\alpha_1^2 + \alpha_2^2 + \alpha_3^2)$, but this is equal to unity and so does not describe any anisotropy effects. A higher order term is given by the fourth degree - $(\alpha_1^2\alpha_2^2+\alpha_2^2\alpha_3^2+\alpha_3^2\alpha_1^2)$, or $(\alpha_1^4+\alpha_2^4+\alpha_3^4)$, and then by the sixth degree - e.g $(\alpha_1^2\alpha_2^2\alpha_3^2)$, and so on. So we can write an equation for cubic anisotropy energy as:

$$E_K = K_0 + K_1(\alpha_1^4 + \alpha_2^4 + \alpha_3^4) + K_2(\alpha_1^2\alpha_2^2\alpha_3^2) + \ldots$$

In the case of a thin film, it is likely that there exists some tetragonal distortion, that is, that the crystal dimensions are slightly distorted and the direction perpendicular to the film plane is no longer equivalent to those within the film plane. In this case, K_1 will not be equal for the three directions 1, 2,and 3, and so we should write:

$$E_K = K_0 + K_{1\parallel}(\alpha_1^4 + \alpha_2^4) + K_{1\perp}(\alpha_3^4) + \ldots$$

We may equate the effect of this magnetic anisotropy energy density to the action of an equivalent field $\vec{H}_a$ in the direction of the crystal axis. Its value can be obtained by calculating the value of the magnetic field that would exert the same torque on the magnetisation as does the anisotropy interaction. This gives a mechanism to incorporate the effects of the magnetocrystalline anisotropies in formulating the resonance conditions, by considering them as additional magnetic fields. An example of this is given in the paper by Kohmoto [58].

We can examine briefly the example of a uniaxial anisotropy (where $E_K = -K_1\cos^2\theta$). The torque is given by $\tau = \vec{M} \times \vec{H}$ and the energy is $-\vec{M}.\vec{H}$, so $dE = \tau d\theta$. So for uniaxial anisotropy, taking small angle approximation ($\sin\theta \approx \theta$), we get:

$$H_a M_s \theta = 2K_1 \theta \qquad or \qquad H_a = \frac{2K_1}{M_s}$$

Another method of incorporating the effects of magnetocrystalline anisotropy is to formulate the resonance condition entirely in terms of the system's free energy, as was described by Suhl [59] and Smit and Beljers [48]. We will present a derivation of this method in the next section, and ultimately use this to formulate the resonance conditions used in the rest of this thesis.

3.2.4 Resonance in Terms of System Energy - Suhl/Smit & Beljers equation

A convenient way of giving the resonance condition for any given orientation of $\vec{M}$ and $\vec{H}$ was derived by Suhl [59] and Smit & Beljers [48]. In this formulation, the resonance condition is derived from the free energy of the system, using equation (3.4) along with the formulation

$$\vec{H}_{eff} = -\frac{dE}{d\vec{M}} \tag{3.9}$$

Here $\vec{H}_{eff}$ is the total effective magnetic field (including both externally applied fields, and the internal anisotropy fields), and E is the magnetic free energy density of the system.

We will change coordinate systems from cartesian to polar (as shown in Figure 3.2) using the following transformations:

$$\begin{aligned} M_x &= M \sin\theta \cos\phi \\ M_y &= M \sin\theta \sin\phi \\ M_z &= M \cos\theta \end{aligned}$$

Calculating $\vec{H}$ components for equation (3.9) gives:

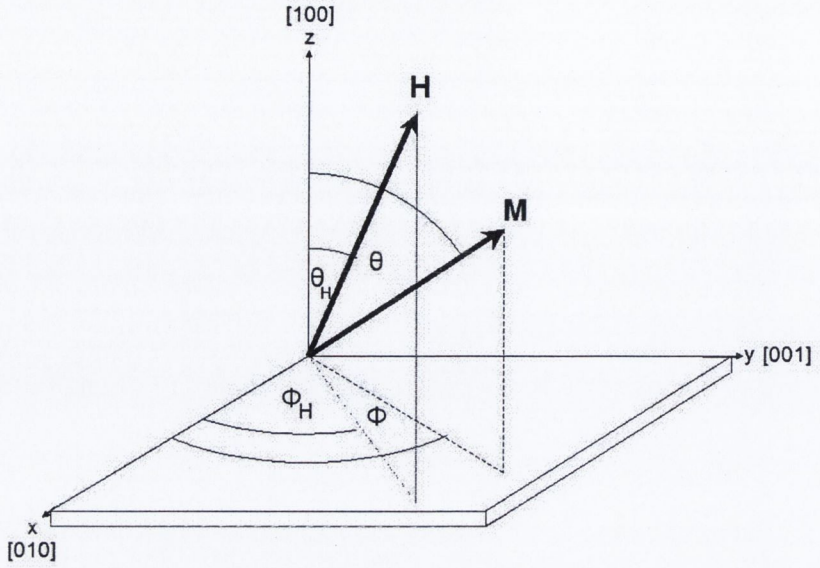

Figure 3.2: Notation used for orientation of $\vec{M}$ and $\vec{H}$, defined by angles ϕ_H, ϕ_M, θ_H and θ_M. Miller notations indicated are in reference to the cubic magnetite films studied, deposited on (100) surfaces.

$$\begin{aligned} H_x &= -\frac{\partial E}{\partial M_x} \\ &= \frac{\partial E}{\partial \phi} \frac{1}{M \sin\theta \sin\phi} \end{aligned}$$

$$\begin{aligned} H_y &= -\frac{\partial E}{\partial M_y} \\ &= -\frac{\partial E}{\partial \phi} \frac{1}{M \sin\theta \cos\phi} \end{aligned}$$

$$\begin{aligned} H_z &= -\frac{\partial E}{\partial M_z} \\ &= \frac{\partial E}{\partial \theta} \frac{1}{M \sin\theta} \end{aligned}$$

Calculating x, y and z components of equation (3.4):

$$\begin{aligned}\frac{\partial \vec{M}}{\partial t} &= -\gamma \vec{M} \times \vec{H}_{eff} \\ &= \hat{x}(\gamma M_z H_y - \gamma M_y H_z) + \hat{y}(\gamma M_x H_z - \gamma M_z H_x) + \hat{z}(\gamma M_y H_x - \gamma M_x H_y) \\ &= \hat{x}\frac{\partial M_x}{\partial t} + \hat{y}\frac{\partial M_y}{\partial t} + \hat{z}\frac{\partial M_z}{\partial t}\end{aligned}$$

Equating the $\hat{x}$ components, $\hat{y}$ components and $\hat{z}$ components, we have:

$$\begin{aligned}\frac{\partial M_x}{\partial t} &= \gamma M_z H_y - \gamma M_y H_z \\ \frac{\partial M_y}{\partial t} &= \gamma M_x H_z - \gamma M_z H_x \\ \frac{\partial M_z}{\partial t} &= \gamma M_y H_x - \gamma M_x H_y\end{aligned}$$

Using these, we can calculate the time derivatives of θ and ϕ (A):

$$\begin{aligned}\frac{\partial \theta}{\partial t} &= \frac{\partial \theta}{\partial M_x}\frac{\partial M_x}{\partial t} + \frac{\partial \theta}{\partial M_y}\frac{\partial M_y}{\partial t} + \frac{\partial \theta}{\partial M_z}\frac{\partial M_z}{\partial t} \\ &= \frac{\partial \theta}{\partial M_x}(\gamma M_z H_y - \gamma M_y H_z) \\ &\quad + \frac{\partial \theta}{\partial M_y}(\gamma M_x H_z - \gamma M_z H_x) \\ &\quad + \frac{\partial \theta}{\partial M_z}(\gamma M_y H_x - \gamma M_x H_y) \\ &= -\frac{\gamma}{M \sin\theta}\frac{\partial E}{\partial \phi}\end{aligned}$$

$$
\begin{aligned}
\frac{\partial \phi}{\partial t} &= \frac{\partial \phi}{\partial M_x}\frac{\partial M_x}{\partial t} + \frac{\partial \phi}{\partial M_y}\frac{\partial M_y}{\partial t} + \frac{\partial \phi}{\partial M_z}\frac{\partial M_z}{\partial t} \\
&= \frac{\partial \phi}{\partial M_x}(\gamma M_z H_y - \gamma M_y H_z) \\
&\quad + \frac{\partial \phi}{\partial M_y}(\gamma M_x H_z - \gamma M_z H_x) \\
&\quad + \frac{\partial \phi}{\partial M_z}(\gamma M_y H_x - \gamma M_x H_y) \\
&= \gamma \frac{1}{M \sin\theta}\frac{\partial E}{\partial \phi}
\end{aligned}
$$

The equilibrium position for $\vec{M}$ is (θ_0, ϕ_0), is given by the condition:

$$
\left.\frac{\partial E}{\partial \theta}\right|_{\theta_0,\phi_0} = \left.\frac{\partial E}{\partial \phi}\right|_{\theta_0,\phi_0} = 0
$$

Expanding the derivatives of E (B):

$$
\begin{aligned}
\frac{\partial E}{\partial \theta} &= \frac{\partial^2 E}{\partial \theta^2}\delta\theta + \frac{\partial^2 E}{\partial \theta \partial \phi}\delta\phi \\
&= E_{\theta\theta}\delta\theta + E_{\theta\phi}\delta\phi
\end{aligned}
$$

$$
\begin{aligned}
\frac{\partial E}{\partial \phi} &= \frac{\partial^2 E}{\partial \phi^2}\delta\phi + \frac{\partial^2 E}{\partial \theta \partial \phi}\delta\theta \\
&= E_{\phi\phi}\delta\phi + E_{\theta\phi}\delta\theta
\end{aligned}
$$

The instantaneous position of the magnetisation vector is given by (C):

$$
\theta = \theta_0 + \delta\theta = \theta_0 + \Delta_\theta e^{i\omega t}
$$

$$
\phi = \phi_0 + \delta\phi = \phi_0 + \Delta_\phi e^{i\omega t}
$$

Substituting (B) and (C) into (A):

$$\begin{aligned}\frac{\partial\theta}{\partial t} &= \Delta_\theta i\omega e^{i\omega t} \\ &= -\frac{\gamma}{M\sin\theta}\left(E_{\theta\theta}\Delta_\theta e^{i\omega t} + E_{\theta\phi}\Delta_\phi e^{i\omega t}\right)\end{aligned}$$

$$\begin{aligned}\frac{\partial\phi}{\partial t} &= \Delta_\phi i\omega e^{i\omega t} \\ &= \frac{\gamma}{M\sin\theta}\left(E_{\phi\phi}\Delta_\phi e^{i\omega t} + E_{\theta\phi}\Delta_\theta e^{i\omega t}\right)\end{aligned}$$

This gives two equations:

$$\begin{aligned}\Delta_\theta\left(i\omega + E_{\theta\phi}\frac{\gamma}{M\sin\theta}\right) + \Delta_\phi\left(E_{\phi\phi}\frac{\gamma}{M\sin\theta}\right) &= 0 \\ \Delta_\theta\left(-\frac{\gamma}{M\sin\theta}E_{\theta\theta}\right) + \Delta_\phi\left(i\omega - \frac{\gamma}{M\sin\theta}E_{\theta\phi}\right) &= 0\end{aligned}$$

These equations can be solved by converting to matrix form - nonzero solution is given for:

$$\begin{vmatrix} i\omega + E_{\theta\phi}\frac{\gamma}{M\sin\theta} & E_{\phi\phi}\frac{\gamma}{M\sin\theta} \\ -\frac{\gamma}{M\sin\theta}E_{\theta\theta} & i\omega - \frac{\gamma}{M\sin\theta}E_{\theta\phi} \end{vmatrix} = 0$$

$$\rightarrow \quad \left(i\omega + E_{\theta\phi}\frac{\gamma}{M\sin\theta}\right)\left(i\omega - \frac{\gamma}{M\sin\theta}E_{\theta\phi}\right) + \frac{\gamma^2}{M^2\sin^2\theta}E_{\phi\phi}E_{\theta\theta} = 0$$

Rearranging gives the Suhl or Smit & Beljers equation:

$$\left(\frac{\omega}{\gamma}\right)^2 = \left(\frac{1}{M\sin\theta}\right)^2\left[E_{\theta\theta}E_{\phi\phi} - (E_{\theta\phi})^2\right] \tag{3.10}$$

For the case of nonzero damping, the equation is extended to

$$\left(\frac{\omega}{\gamma}\right)^2 = \left(\frac{1+\alpha^2}{M\sin\theta}\right)^2 \left[E_{\theta\theta}E_{\phi\phi} - (E_{\theta\phi})^2\right] \tag{3.11}$$

where α is the Landau-Lifschitz loss parameter ($\alpha = \mathrm{G}/(\gamma \mathrm{M})$) as defined in section 3.2.1.

3.2.5 Resonance Condition for a Thin Magnetite Film

In this section we will use the Suhl or Smit and Beljers equation 3.10 to derive the expected resonance conditions for our magnetite films; that for the nanowire samples will be derived in Chapter 7. The magnetite samples examined for this thesis are all (100) plane films with edges cut along [010] and [001] directions corresponding to x and y axes respectively in Figure 3.2. In the FMR measurements the magnetic field $\vec{H}$ is rotated either in the film plane ("in-plane") or out of plane but within the (001) plane. We will derive the resonance condition for these two cases.

Following the approach taken by Liu et. al. [60] and Farle [53] we will take the free energy density (in cgs units) to be

$$E = -\vec{M}.\vec{H} + 2\pi M^2\alpha_3^2 - K_{4||}(\alpha_1^4 + \alpha_2^4) - K_{4\perp}\alpha_3^4 - K_{2\perp}\alpha_3^2 \tag{3.12}$$

where α_1, α_2 and α_3 are the directional cosines of the magnetisation vector with regard to the axes x, y, z respectively as defined in Figure 3.2.

The first term in equation (3.12) is the Zeeman energy and the second is the demagnetising energy (corresponding to the "shape anisotropy") for an infinite plane that in our case is a good approximation. Bulk Fe_3O_4 exhibits cubic magnetocrystalline anisotropy with [111] as the easy axis [38] and therefore one might expect to include a term in $(\alpha_1^4 + \alpha_2^4 + \alpha_3^4)$. However, because of the mismatch between film and substrate we follow Liu et. al. [60] and Farle [53] and allow for the possibility of a tetragonal distortion normal to the film plane in which case $\mathrm{K}_{4||} \neq \mathrm{K}_{4\perp}$. It is also possible that there is a perpendicular uniaxial anisotropy given by the term in $\mathrm{K}_{2\perp}$.

It is convenient to express equation 3.12 in terms of spherical polar coordinates shown in Figure 3.2 and therefore we make the substitutions:

$$\vec{H} = (H\cos\phi_H \sin\theta_H)\hat{x} + (H\sin\phi_H \sin\theta_H)\hat{y} + (H\cos\theta_H)\hat{z}$$

$$\vec{M} = (M\cos\phi_M \sin\theta_M)\hat{x} + (M\sin\phi_M \sin\theta_M)\hat{y} + (M\cos\theta_M)\hat{z}$$

$$\begin{aligned} \alpha_1 &= \sin\theta\cos\phi \\ \alpha_2 &= \sin\theta\sin\phi \\ \alpha_3 &= \cos\theta \end{aligned}$$

so that equation (3.12) becomes:

$$\begin{aligned} E = \frac{1}{2}M[&-2H\left(\cos\theta\cos\theta_H + \sin\theta\sin\theta_H\cos(\phi-\phi_H)\right) + 4\pi M\cos^2\theta - H_{2\perp}\cos^2\theta \\ &-\frac{1}{2}H_{4\perp}\cos^4\theta - \frac{1}{2}H_{4||}\frac{1}{4}\left(3+\cos 4\phi\right)\sin^4\theta] \end{aligned}$$

Here we have used the formulation $H_i = 2K_i/M$ as described in section 3.2.3.

The equilibrium conditions are obtained by evaluating E_ϕ and E_θ at the equilibrium angles and setting them equal to zero.

$$\begin{aligned} E_\theta = \frac{1}{2}M[&2H\left(\sin\theta\cos\theta_H - \cos\theta\sin\theta_H\cos(\phi-\phi_H)\right) \\ &+\sin 2\theta\left(-(4\pi M - H_{2\perp}) + H_{4\perp}\cos^2\theta - H_{4||}\frac{1}{4}\left(3+\cos 4\phi\right)\sin^2\theta\right)] = 0 \end{aligned} \tag{3.13}$$

$$E_\phi = \frac{1}{2}M[2H\left(\sin\theta\sin\theta_H\sin(\phi-\phi_H)\right) + \frac{1}{2}H_{4||}\left(\sin 4\phi\right)\sin^4\theta] = 0 \tag{3.14}$$

We will now use the Suhl/Smit and Beljers equation (3.10) as derived before:

$$\left(\frac{\omega}{\gamma}\right)^2 = \left(\frac{1}{M\sin\theta}\right)^2 \left[E_{\theta\theta}E_{\phi\phi} - (E_{\theta\phi})^2\right]$$

Evaluating the derivatives $E_{\theta\theta}$, $E_{\phi\phi}$ and $E_{\theta\phi}$ and substituting into equation (3.10),

the applied field, H, at resonance is given by [60]:

$$\left(\frac{\omega}{\gamma}\right)^2 = \left[(H \times a_1 + b_1)(H \times a_1 + b_2) - b_3^2\right] \tag{3.15}$$

where

$$\begin{aligned}
a_1 &= \cos\theta\cos\theta_H + \sin\theta\sin\theta_H\cos(\phi - \phi_H) \\
b_1 &= (H_{2\perp} - 4\pi M)\cos 2\theta + H_{4\perp}\frac{\cos 2\theta + \cos 4\theta}{2} + H_{4||}\frac{(\cos 4\theta - \cos 2\theta)}{2}\frac{(3 + \cos 4\phi)}{4} \\
b_2 &= (H_{2\perp} - 4\pi M)\cos^2\theta + H_{4||}\sin^2\theta\left(\cos 4\phi - \cos^2\theta\frac{3 + \cos 4\phi}{4}\right) + H_{4\perp}\cos^4\theta \\
b_3 &= \frac{1}{2}\cos\theta\left(\frac{3}{2}H_{4||}\sin 4\phi\sin^2\theta\right)
\end{aligned}$$

In-Plane Rotation

Here we will derive the general resonance equation for the case where the applied magnetic field is at an arbitrary direction within the film plane, that is within the (x, y) plane (i.e. $\theta_H = 90°$).

Following Liu et. al. [60] we also take $\vec{M}$ to lie in plane so that $\theta = \theta_H = 90°$.

Evaluating equation(3.15) for $\theta = \theta_H = 90°$ gives:

$$\begin{aligned}
a_1 &= \cos(\phi - \phi_H) \\
b_1 &= 4\pi M - H_{2\perp} + H_{4||}\frac{3 + \cos 4\phi}{4} \\
b_2 &= H_{4||}\cos 4\phi \\
b_3 &= 0
\end{aligned}$$

and so we get the resonance equation:

$$\left(\frac{\omega}{\gamma}\right)^2 = \left(H\cos(\phi - \phi_H) + 4\pi M - H_{2\perp} + H_{4||}\frac{3 + \cos 4\phi}{4}\right)\left(H\cos(\phi - \phi_H) + H_{4||}\cos 4\phi\right)$$

Evaluating (3.14) for $\theta = \theta_H = 90°$:

$$2H\sin(\phi - \phi_H) + \frac{1}{2}H_{4||}\sin 4\phi = 0$$

so

$$\sin(\phi - \phi_H) = -\frac{H_{4||}}{4H}\sin 4\phi$$

If, as we find to be so, H >> $H_{4||}$ then $\sin(\phi - \phi_H)$ is almost equal to zero and hence $\phi \approx \phi_H$.

It is useful to group the shape and uniaxial anisotropy terms as they act in the same manner. Using the notation $4\pi M - H_{2\perp} = 4\pi M_{eff}$, and setting $\phi = \phi_H$, we obtain the final resonance equation:

$$\left(\frac{\omega}{\gamma}\right)^2 = \left(H + 4\pi M_{eff} + H_{4||}\frac{3 + \cos 4\phi}{4}\right)\left(H + H_{4||}\cos 4\phi\right) \tag{3.16}$$

Out-Of-Plane Rotation

We will now examine the case where we vary the angle between the applied field and the plane of the film. Specifically, with reference to figure 3.2, the applied field direction is within the (z, x) plane (i.e. $\phi_H = 0°$), and we vary the angle θ_H.

Following Liu et. al. [60] we again take $\vec{M}$ to lie within the (z-x) plane so that $\phi = \phi_H = 90°$.

Evaluating equation(3.15) for $\phi = \phi_H = 90°$:

$$\begin{aligned}
a_1 &= \cos(\theta - \theta_H) \\
b_1 &= (H_{2\perp} - 4\pi M)\cos 2\theta + H_{4\perp}\frac{\cos 2\theta + \cos 4\theta}{2} + H_{4||}\frac{\cos 4\theta - \cos 2\theta}{2} \\
b_2 &= (H_{2\perp} - 4\pi M)\cos^2\theta + H_{4||}\sin^4\theta + H_{4\perp}\cos^4\theta \\
b_3 &= 0
\end{aligned}$$

which, using the formulation $4\pi M - H_{2\perp} = 4\pi M_{eff}$ as before, gives the resonance equation:

$$\begin{aligned}
\left(\frac{\omega}{\gamma}\right)^2 = &\left(H\cos(\theta - \theta_H) - \left[4\pi M_{eff} - \frac{H_{4\perp}}{2} + \frac{H_{4||}}{2}\right]\cos 2\theta + \left[H_{4\perp} + H_{4||}\right]\frac{\cos 4\theta}{2}\right) \\
&\times \left(H\cos(\theta - \theta_H) - 4\pi M_{eff}\cos^2\theta + H_{4||}\sin^4\theta + H_{4\perp}\cos^4\theta\right)
\end{aligned}$$

or:

$$\left(\frac{\omega}{\gamma}\right)^2 = \left(H\cos(\theta-\theta_H) - \left[4\pi M_{eff} - \frac{H_{4\perp}}{2} + \frac{H_{4||}}{2}\right]\cos 2\theta + \left[H_{4\perp} + H_{4||}\right]\frac{\cos 4\theta}{2}\right) \times \left(H\cos(\theta-\theta_H) - \left(4\pi M_{eff} + 2H_{4||}\right)\cos^2\theta + \left(H_{4||} + H_{4\perp}\right)\cos^4\theta + H_{4||}\right) \tag{3.17}$$

The equilibrium position for the angle θ for a given θ_H is given by evaluating equation (3.13) for $\phi = \phi_H = 90°$:

$$H\sin(\theta-\theta_H) - \cos\theta\sin\theta(4\pi M_{eff} - H_{4\perp}\cos^2\theta + H_{4||}\sin^2\theta) = 0 \tag{3.18}$$

3.2.6 Modifications to the Resonance Condition for a Thin Film with In-Plane Uniaxial Anisotropy

Here we will examine the modifications to the model used in section 3.2.5 necessary to derive the a resonance equation for the case of a single-crystal thin film with cubic symmetry in its crystalline structure, but with an additional induced in-plane twofold or uniaxial anisotropy. This sort of anisotropy results from symmetry-breaking within the system - for example, that induced by deposition on a stepped surface, as we investigate in Chapter 6. We will model the energy as before, but this time we will include the in-plane first order anisotropy constant, $K_{2||}$, which characterises any uniaxial anisotropy.

Since we are considering a uniaxial anisotropy energy, it will have terms in the second degree, i.e. of the form α_i^2. However, the combination of terms used will depend on the direction along which the anisotropy is oriented. For example, if the anisotropy is directed along the [010] or [001] axes, the energy term will involve only α_1^2 or α_2^2 respectively. However, if the anisotropy is in another direction, not co-directed with one of the crystal axes, the energy term will involve a combination of the two. Relevant energy expressions are given in Table 3.2.

We can then add the relevant energy term into the overall film energy (equation (3.12), and compute the resonance condition using equation (3.10) as in section 3.2.5. We will use this method to incorporate observed step-induced anisotropy in later chapters.

Anisotropy Direction	Energy Term	
[010]	$E = -K_{2\|\|}\alpha_1^2$	$E = -K_{2\|\|}\sin^2\theta\cos^2\phi$
[001]	$E = -K_{2\|\|}\alpha_2^2$	$E = -K_{2\|\|}\sin^2\theta\sin^2\phi$
[011]	$E = -K_{2\|\|}\frac{1}{\sqrt{2}}(\alpha_1+\alpha_2)^2$	$E = -K_{2\|\|}\sin^2\theta\cos^2\left(\phi-\frac{\pi}{4}\right)$
$[0\bar{1}1]$	$E = -K_{2\|\|}\frac{1}{\sqrt{2}}(\alpha_2-\alpha_1)^2$	$E = -K_{2\|\|}\sin^2\theta\sin^2\left(\phi-\frac{\pi}{4}\right)$

Table 3.2: Energy expressions for in-plane uniaxial anisotropy, following the form used by Liu et. al. [60]. Energy expressions are given in terms of the directional cosines ($\alpha_i s$) with respect to the principal crystal axes, and in terms of θ and ϕ as shown in Figure 3.2.

3.2.7 Linewidth Interpretation

The linewidth in ferromagnetic resonance is generally considered to consist of two main elements:

$$\Delta H_{pp} = \Delta H_{hom} + \Delta H_{inhom}$$

The first is the homogeneous contribution, ΔH_{hom}, arising from the intrinsic damping of the magnetisation and ΔH_{inhom} comes from the magnetic inhomogeneities of the sample; both can have an angular dependence. The homogeneous contribution is given by [59]:

$$\Delta H = \frac{\alpha}{|\partial\omega/\partial H|}\frac{\gamma}{M}\left(E_{\theta\theta} + \frac{1}{sin^2\theta}E_{\phi\phi}\right) \tag{3.19}$$

ΔH in equation 3.19 is the full width at half maximum of the absorption lineshape; for a Lorentzian $\Delta H_{pp} = \sqrt{3}^{-1}\Delta H_{1/2}$. Using the relation mentioned in Section 3.2.1, that is $\alpha = G/(\gamma M)$, the final dependence is given as [61]:

$$\Delta H_{hom} = \frac{1}{\sqrt{3}}\frac{1}{|\partial\omega/\partial H|}\frac{G}{M^2}\left(\frac{\partial^2 E}{\partial\theta^2} + \frac{1}{\sin^2\theta}\frac{\partial^2 E}{\partial\phi^2}\right) \tag{3.20}$$

We can use this equation in a similar manner to the general resonance equation (3.10) to formulate an equation for the linewidth for a given orientation using the free energy of the system.

Magnetic inhomogeneities, arising from sample imperfections, such as mosaic structure and defects, can give rise to a distribution in the directions of both the crystal and magnetic anisotropy axes as well as a spread in the magnitudes of the internal fields. So, following Chappert et al [62], we can write

$$\Delta H_{inhom} = \Delta H_0 + \sum_i \frac{\partial H_R}{\partial \phi_i} \Delta \phi_i + \sum_j \frac{\partial H_R}{\partial H_j} \Delta H_j \tag{3.21}$$

The term in $\Delta\phi_i$ allows for a possible angular distribution of the crystalline-axis orientation about the average direction, and that in ΔH_j allows for a difference in internal anisotropy fields experienced within the sample. ΔH_0 is a constant.

3.3 Experimental Details

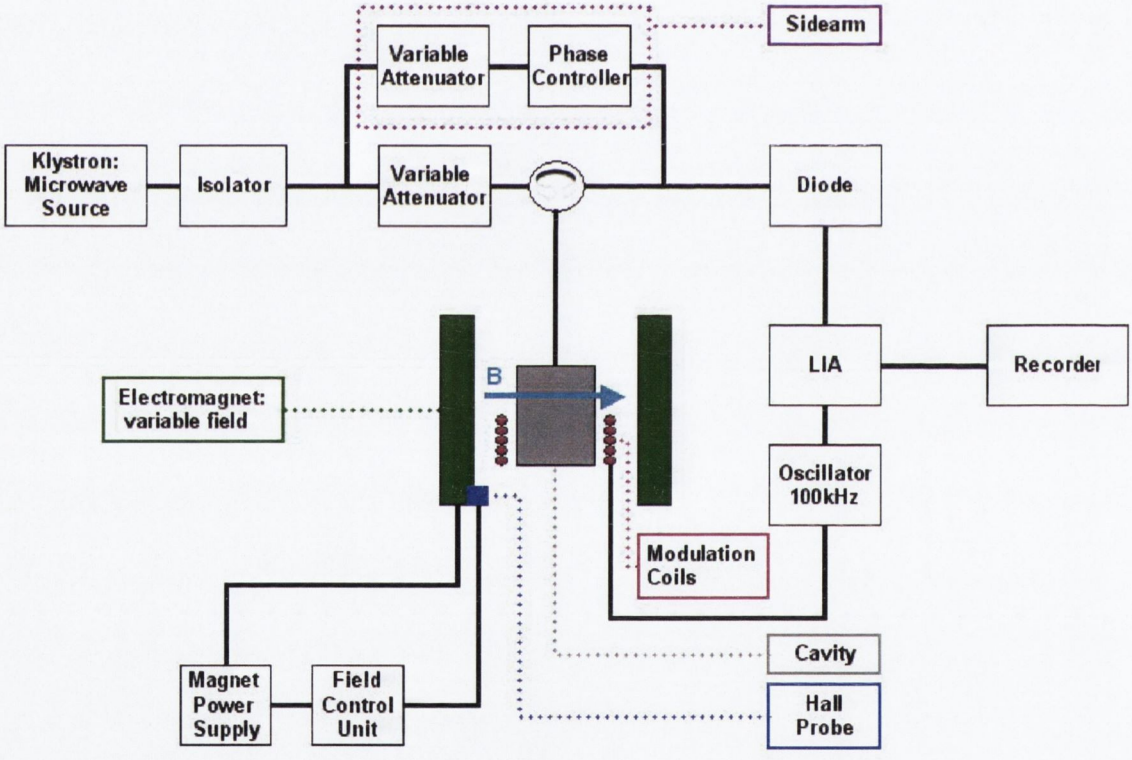

Figure 3.3: Schematic of FMR setup

Figure 3.3 shows the layout of the equipment that is essentially that of a Bruker EPR spectrometer, model ER-420. It operates at X-band (9-10 GHz) with a microwave frequency of about 9.6GHz with 100kHz field modulation. The sample is placed at the center of a TE_{102} mode cavity. The microwaves from the klystron pass through an isolator, variable attenuator and circulator before reaching the microwave cavity.

Before recording an FMR signal the klystron frequency is adjusted to equal the cavity mode frequency so that standing waves are set up in the cavity; an automatic frequency control keeps the klystron frequency equal to the cavity mode frequency. It was usual to critically couple the cavity so that, off resonance, no microwave power was reflected from the cavity. Under these conditions it is necessary to bias the detector diode by allowing a small amount of power to reach it via the side arm. To detect resonance the field provided by the electromagnet is swept slowly at fixed microwave frequency. At resonance, power is absorbed by the sample and this alters the matching between waveguide and cavity leading to power being reflected to the detector diode via the circulator. The diode rectifies the input and gives a change in D.C. voltage output that is a measure of the change in reflected power. To improve the signal to noise ratio a small 100kHz magnetic field modulation is applied using the modulation coils. This in turn modulates the reflected power and hence also the diode output. The diode output is amplified and then fed into the lock-in-amplifier (LIA), the output of which is a D.C. voltage proportional to the amplitude of the 100kHz A.C. input. As a result the resonance signal corresponds to the first derivative of absorbed power with respect to magnetic field. The LIA output is sent to a PC for collection and subsequent analysis.

In order to determine the field position of the resonance it was necessary to calibrate the field. The field range was calibrated using both a Hall probe gaussmeter and also an NMR probe; the latter was more accurate but only covered a limited range. In addition the field at a particular channel number could be found by recording, together with the FMR signal, the EPR signal from F^+ centers in MgO which have a known g-value of 2.0023. By choosing a suitable size for the MgO:F^+ sample it was possible to ensure that its signal was clearly visible but did not obscure or distort the FMR signal.

3.3.1 Sample Mounting Procedure

While examining the dependence of resonance field H_R on the direction of the applied field with respect to the crystal axes, we performed two types of experiments: an in plane rotation, in which the magnetic field is rotated within the film plane, and an out of plane rotation, in which the magnetic field is rotated between in plane and out of plane directions.

The coordinate system used to specify the directions of $\vec{M}$ and $\vec{H}$ is shown in figure

3.2. For the in plane rotation, we fix θ_H at 90°, and vary ϕ_H as shown in figure 3.4(a). For the out of plane rotation, we fix ϕ_H at 0°, and vary θ_H, as shown in figure 3.4(b).

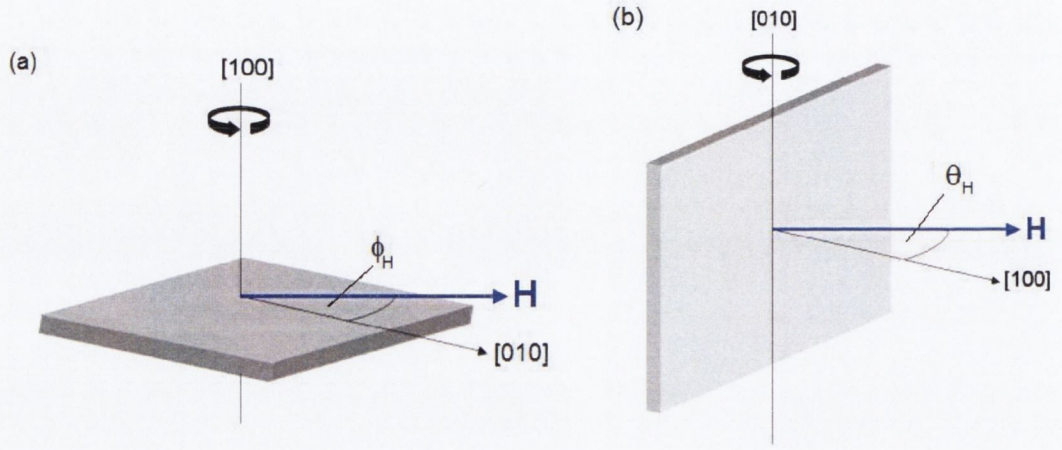

Figure 3.4: Illustration of sample orientation for (a) in plane, and (b) out of plane rotations.

For the in-plane rotation, the sample was mounted flat on the end of a spin-free quartz rod (as illustrated in Figure 3.5(a)), so that the magnetic field is applied in the plane of the film. Since the demagnetising factor has a very pronounced effect on the resonance condition, and since its value will change if the the direction of the applied field is moved out of the film plane, it was imperative that the magnetic field remained always within the film plane. To check that this was so for the samples with cubic symmetry, test scans were taken for field orientations separated by 90° within the plane of the film. If these gave the same resonance field the sample was correctly aligned for the experiment.
As it was not possible to perform this check for samples with spectra showing a 180° periodicity, we ran these experiments multiple times (re-mounting each time), to eliminate any mounting error.

The change in rotation angle could be measured to within a number of minutes with the goniometer. To approximately determine the absolute direction of the applied magnetic field, $\vec{H}$, the sample was first mounted as accurately as possible (typically within 5°) such that $\vec{H}$ was parallel to a sample edge (a [100] type direction) for the in-plane rotations, or normal to the film plane for the out of plane rotations. This gave turning points of H_R within a few degrees of the expected high symmetry direction which was then assigned to the turning point.

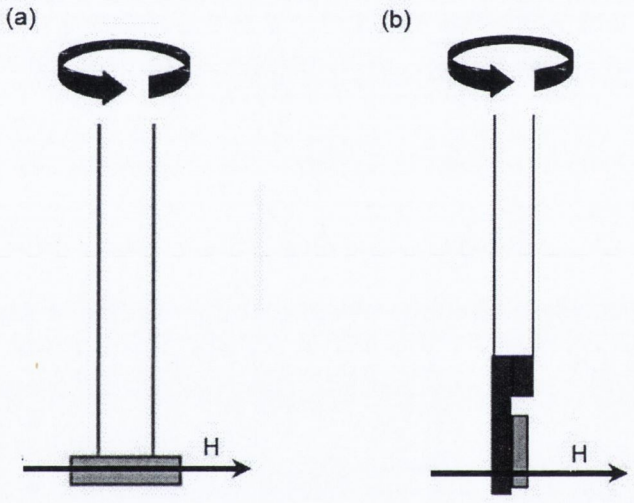

Figure 3.5: Illustration of sample mounting procedures. (a) In plane rotation experiment. The grey rectangle indicates the sample, mounted flat on the end of the quartz rod. (b) Out of plane rotation experiment. The grey rectangle indicates the sample, mounted vertically on a plastic mount, attached to the end of the quartz rod. In both cases the external field is applied horizontally, and the sample is rotated about the vertical axis.

Chapter 4

FMR Characterisation of MBE Deposited Thin Magnetite Films

4.1 Introduction

In this chapter we will present the results of an FMR study conducted on thin magnetite films deposited on MgO and $MgAl_2O_4$ by Molecular Beam Epitaxy (MBE). The aims of the study are to explore the magnetic anisotropy behaviour of these films, and specifically to extract the films' magnetic anisotropy constants. We do this by examining the angular dependencies of the ferromagnetic resonance field, H_R, for films of varying thickness. We will also investigate how these characteristics change as the substrate is changed from MgO to $MgAl_2O_3$.
We performed FMR measurements at 9.6 GHZ on films of magnetite deposited by MBE on substrates of (100) MgO and (100) $MgAl_2O_4$. We examined films with thickness in the range 5nm to 700nm, looking at the variation in resonance field as the applied field direction was varied with respect to the primary crystalline axes.
We will also briefly examine some results of an unpublished high-frequency FMR study on the same samples, undertaken by R.C. Barklie, G. Smith and H. El Mkami in St. Andrew's University.

The chapter is laid out as follows: first, we will provide a short review of the published FMR studies on magnetite films. We will then outline the experimental details, giving details of the samples investigated and the experiments conducted. We will present the results of experiments conducted at high frequency on the samples, as mentioned above, along with the experimental results obtained from the study performed at 9.6 GHz in TCD. We will finally give the analysis of these results, and provide a detailed discussion.

4.2 Literature Survey

Magnetite (Fe_3O_4), as a half-metallic ferromagnetic oxide with high Curie temperature, has attracted much scientific interest due to its potential uses in the area of spin-electronics. A number of works have been published outlining characterisation of magnetite films on different substrates produced using various deposition methods. Of particular interest with regard to the work detailed in this thesis are the results for films deposited on MgO and $MgAl_2O_3$.

Initial works characterising the properties of bulk magnetite were carried out by Bickford [38] and Calhoun [63]. Results from work on sputter deposited films has been published by a number of authors: Atkas [9], Margulies et. al. [23], and Balakrishan et. al. [11]. Studies on pulsed laser deposited (PLD) films were published by Kale et. al [12], and studies on films grown by reactive ion beam deposition were published by Lai et. al. [64]. MBE deposited films have also been investigated by a number of authors, P.A.A. van der Heidjen et. al. [13], Margulies et. al. [23], Voogt et. al. [14], Krebs et. al. [65], Fontijn et. al [15], Arora et. al [16–18,66] and Zhou et. al. [19–21,67].

The magnetisation of magnetite films is one property which has been extensively studied, with greatly varying results. Films deposited on (100) MgO by sputtering with thicknesses 13-6630nm [10], 301nm [9], and 100-600nm [11] were all found not to have magnetisation saturated at even high fields ($\geq$ 1 T). Films of thickness 45-195nm grown by ion beam deposition were found to have saturation magnetisation of around 310 emu/cm^3 [64], much lower than the bulk value of 496 emu/cm^3. Some films deposited by MBE, of thickness 428nm [23] and 100nm [19] were found not to have magnetisation saturated at even high fields, whereas other films deposited by MBE of thickness 20nm [14] and 30.5 nm [15], and those deposited by PLD of thickness 30-200 nm [12] were found to have magnetisation saturated at moderate fields. In a number of publications [19,23] this property has been linked to the presence of antiphase boundaries within the films.

Ferromagnetic resonance is an excellent method for investigating the magnetic anisotropies in magnetic films, and a number of studies have been conducted on thin films of

magnetite on MgO and $MgAl_2O_4$ [9,12,13,65]. Anisotropies can also be probed using torque magnetometry [23]. In all cases, the easy axis of magnetisation was observed to be along [110]-type directions. The cubic anisotropy field, $H_{4||}$ was consistently observed to be lower than that of the bulk material, with values ranging from -440 Oe [65] and -330 to -380 Oe [13] for MBE deposited films, to only -22 Oe [9] for a film deposited by sputtering. In many cases [10,12,13] where the thickness of the film was varied, the anisotropy was seen to increase with film thickness. For the case of films deposited by PLD, the cubic anisotropy was seen to disappear altogether for films with thickness below 80nm.

Other parameters examined are $4\pi M_{eff} = 4\pi M_s - 2K_{2\perp}/M$ and $H_{4\perp} = 2K_{2\perp}/M$, quantifying the strain induced uniaxial anisotropy. Again conflicting results are seen. For a 1.5μm thick MBE deposited film on MgO, was observed to be 4.7 kOe [23]. In another study of films deposited on MgO by MBE, the uniaxial anisotropy field $H_{4\perp}$ was observed to increase with increase in film thickness [13]. For a 301nm film deposited on MgO by sputtering, a value of 3.58 kOe was observed for $4\pi M_{eff}$ [9]. For PLD deposited films, $4\pi M_{eff}$ was reported to increase from 2.5 kOe to 7 kOe with an increase in film thickness from 30nm to 200nm [12]. In this case, films on both MgO and $MgAl_2O_4$ were investigated.

4.3 Experimental Details

4.3.1 Samples Investigated

Thin films of magnetite of different thicknesses were deposited on flat (100) MgO and (100) $MgAl_2O_4$ (MAO) substrates by MBE at temperature 250°C and base pressure $5x10^{-10}$ Torr. Film thickness was controlled by quartz crystal thickness monitors, calibrated using X-ray reflectometry. Further explanation of the deposition procedure is given in Section 2.2.4, and can also be found in [16] and [19].
Five magnetite films were used for these experiments - three films deposited on MgO substrate (thickness 38nm, 78nm and 700nm), and two on MAO substrate (thickness 33nm and 5nm). We label these films as 38MgO, 78MgO, 700MgO, 33MAO and 5MAO. Films were deposited on substrates cut in (100) plane (edges [001] and [010]). All samples were produced in TCD by members of Prof. Shvets group.

Previous Characterisation

Films produced in the same manner as those examined here have been extensively characterised [17,18,66,67] and so we will give only a brief summary of the characteristics relevant to this study.

Structural characterisation by high-resolution X-ray diffraction and cross-sectional transmission electron microscopy showed that films on (100) MgO remained fully strained even up to a thickness of 700nm, far greater than the critical thickness of 60nm which is estimated for films of magnetite on MgO [18].

Magnetisation measurements for films of thickness 30-70nm showed an unsaturated behaviour [17], with the slope of the M vs H increasing with a decrease in film thickness. The same unsaturated behaviour was seen for a film of 100nm thickness [67]. However, for films of thickness 120nm and above, it was possible to saturate the magnetisation of the films with magnetic fields of 5-8 kOe [18]. The values for the magnetisation at 1 T for films of thickness 45nm, 70nm and 700nm were found to be 440 emu/cm^3, 465 emu/cm^3 and 475 emu/cm^3 respectively [18].

The presence of antiphase boundary defects within the films have been linked to the increased strain accommodation properties in the films, and to the difficulty encountered in saturating their magnetisation [19,23].

4.3.2 FMR

Nearly all the FMR measurements reported in this thesis were carried out at TCD using a modified Bruker EPR spectrometer operating at about 9.6 GHz, with 100 kHz field modulation. Samples were inserted into a TE_{102} mode cavity and were attached to a spin-free quartz rod that could be rotated about a vertical axis using a goniometer. The magnetic field was calibrated using an NMR or Hall probe magnetometer and an EPR reference signal due to F^+ centers in MgO ($g = 2.0023$). Measurements were all made at room temperature.

Also included in this chapter are some previous unpublished data obtained on the same samples from measurements at both 94 GHz and 188 GHz. These were carried out at St. Andrew's University by R.C. Barklie, G. Smith and H. El Mkami. The spectrometer uses quasi-optical techniques to implement a broadband homodyne

bridge. Details of the equipment are published elsewhere [68]. Unlike the measurements made at 9.6 GHz at TCD, the high frequency measurements at St. Andrew's were made only for the magnetic field direction perpendicular to the film. The measurements reported here were made at room temperature. It should be noted that, as the resistivity of the magnetite films was $\leq$ 22 ohm.m, the skin depth was much greater than the film thickness even at 188 GHz, as is outlined below:

The strength of an electric field within a conductor decays with depth z as described by the following equation:

$$A = A_0 e^{-\delta}$$

The skin depth is given by:

$$\delta = \sqrt{\frac{2\epsilon_0 c^2}{\sigma\omega}}$$

where σ is the DC electrical conductivity, taken here as the magnetite bulk value of $10^4 \Omega^{-1} m^{-1}$.

	Skin Depth
9. 6GHz	50875nm
94GHz	16427nm
188GHz	11616nm

Table 4.1: Calculated Skin Depths

Calculations for the skin depth in these cases for the relevant frequencies are shown in table 4.1. It can be clearly seen that the skin depth in each case is far greater that the thickness of the film, so the field in each case is fully penetrating.

For the measurements in TCD at 9.6 GHz the direction of the magnetic field, $\vec{H}$, was varied both within the (100) plane of the film (i.e. varying ϕ_H at constant θ_H = 90°) and out of the film plane but within the (001) plane (i.e. varying θ_H at constant ϕ_H = 90°). The angles θ_H, ϕ_H and θ, ϕ are defined using the coordinate system shown in Figure 4.1.

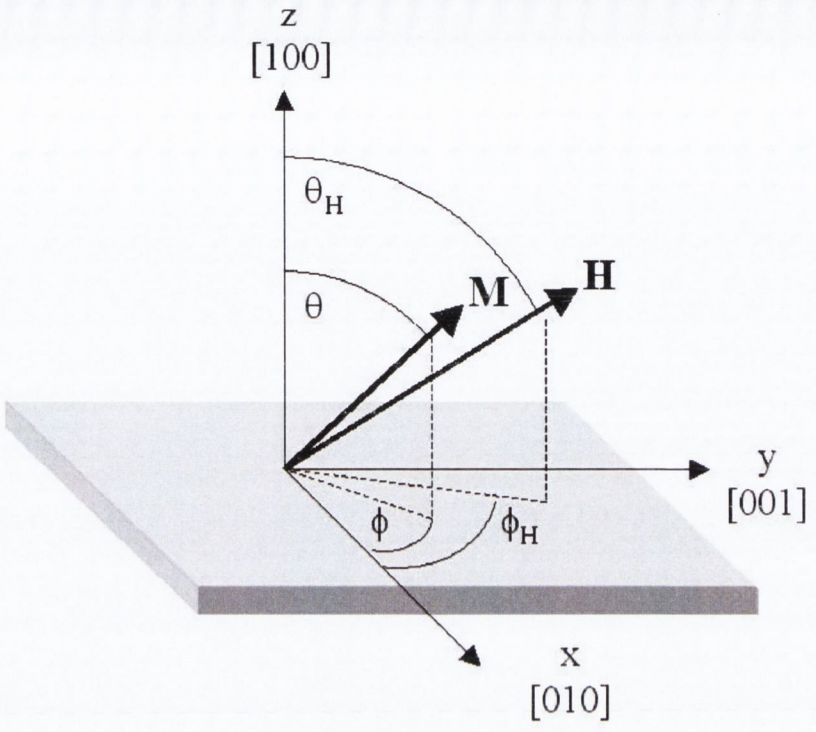

Figure 4.1: Coordinate system used for defining the orientation of $\vec{M}$ and $\vec{H}$ with respect to the film surface. The orientation of the applied magnetic field $\vec{H}$ is given by (ϕ_H, θ_H), while the resulting equilibrium orientation of the magnetisation is given by (ϕ, θ). The film plane is (100). The edges of the film are parallel to [001] and [010].

4.4 FMR Results

4.4.1 Frequency Dependence of FMR Signal

Figures 4.2 and 4.3 show the FMR spectra taken at 94 GHz and 188 GHz respectively for the four samples 38MgO, 78MgO, 700MgO and 33 MAO; the spectra were recorded at St. Andrew's University at room temperature with the magnetic field perpendicular to the film. Representative spectra taken at TCD at 9.6 GHz are shown in Section 4.5.2. Figure 4.2 shows that at 94 GHz the spectrum of the 700MgO sample is not a single symmetric line and we find that it can be well fitted to the superposition of two lines. Also the spectrum at 94 GHz of 78MgO shows the presence of extra, weak lines above and below the strong central line. The other spectra are single symmetric lines with no sign of extra features.

Figure 4.4 shows the dependence of the resonance field, H_R on microwave frequency. In view of the unsymmetrical nature of the spectrum for 700MgO the data for this

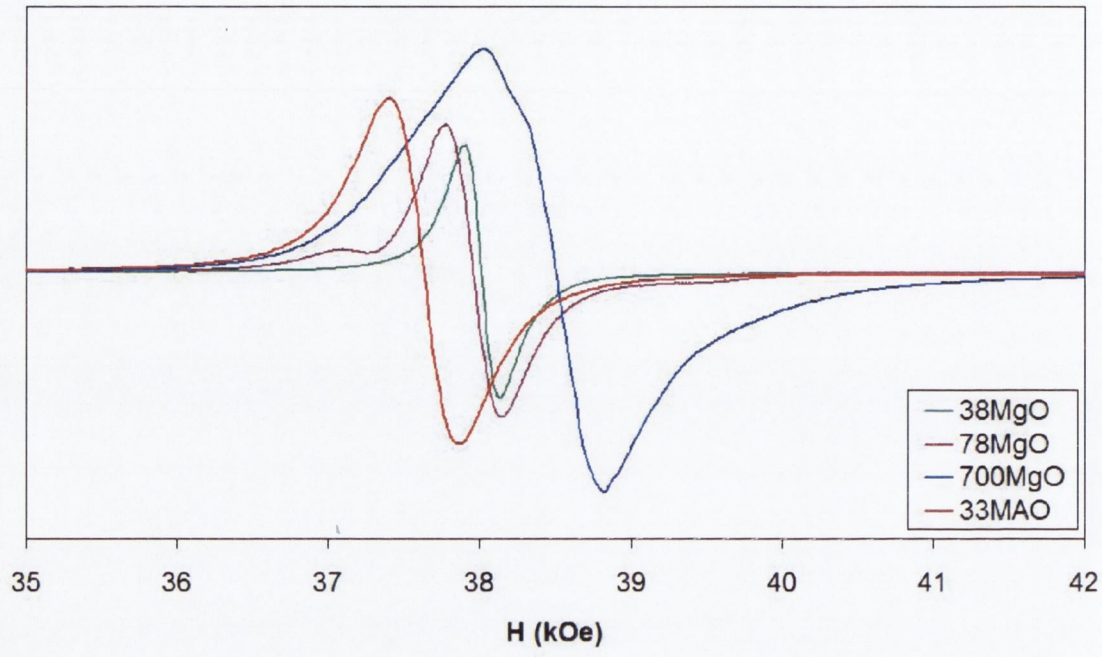

Figure 4.2: FMR spectra taken at 94 GHz with magnetic field perpendicular to the film

sample is omitted. It should be noted that, as is clear from the results presented in Section 4.5.2, the resonance field at 9.6 GHz for $\vec{H}$ perpendicular to the film is an extrapolated value for the samples 38MgO and 78MgO as this exceeds the maximum field of the magnet; however the very good fits obtained for the out-of-plane angular dependence of H_R imply that these are accurate values.

A detailed analysis of the angular dependence of H_R is given in Section 4.5.2 and also in Chapter 3 Section 3.2.5. From Equation 3.17 it follows that for $\vec{H}$ perpendicular to the film, the resonance field H (or H_R) is given by

$$\omega = \gamma\left(H - 4\pi M + H_{2\perp} + H_{4\perp}\right) \quad \rightarrow \quad H = \frac{\omega}{\gamma} + 4\pi M - \left(H_{2\perp} + H_{4\perp}\right) \qquad (4.1)$$

where $H_{2\perp}$ and $H_{4\perp}$ represent the perpendicular uniaxial and perpendicular cubic anisotropy fields respectively.

Equation 4.1 predicts that the graph of H_R versus frequency, ν, should be linear as is observed and from the slope ($= h/g\mu_B$) the g value can be estimated; the intercept on the H axis at $\nu = 0$ gives $4\pi M - H_{2\perp} - H_{4\perp}$ and this, together with the estimated g value, is given in Table 4.2 for samples 38MgO, 78MgO and 33MAO.

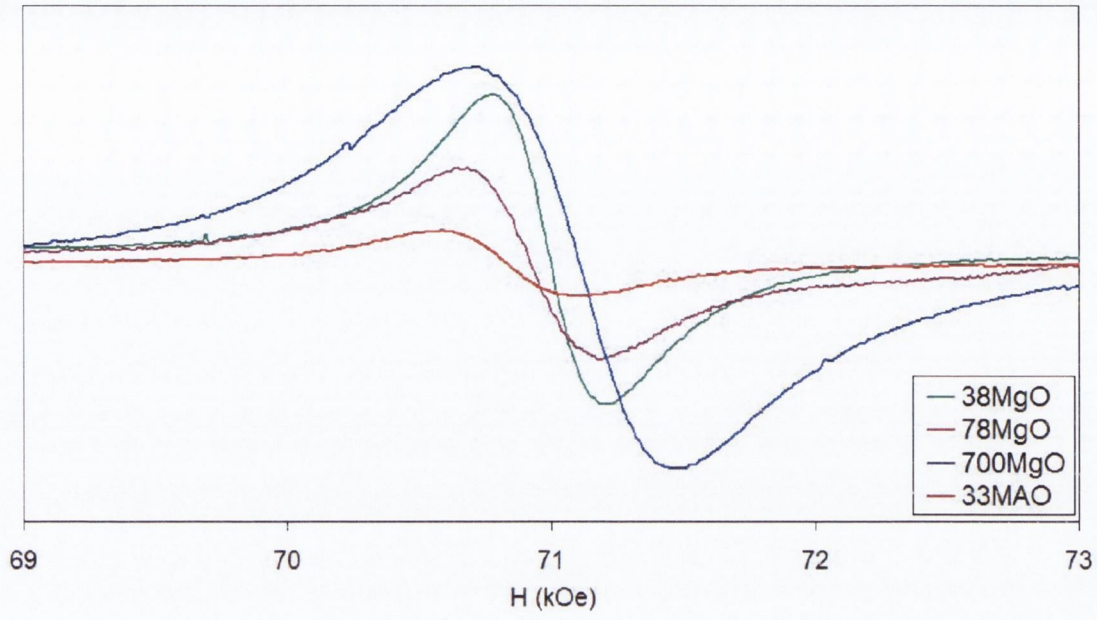

Figure 4.3: FMR spectra taken at 188 GHz with magnetic field perpendicular to the film

Table 4.2: Parameter values obtained from fits of High Field Data

	g value	$4\pi M - H_{2\perp} - H_{4\perp}$ (kOe)
38MgO	2.032 ± 0.003	4.88 ± 0.07
78MgO	2.034 ± 0.003	4.86 ± 0.07
33MAO (3 point)	1.99 ± 0.04	3.5 ± 0.1
33MAO (2 point)	2.024± 0.004	4.46 ± 0.03

For the sample 33MAO the parameters were evaluated with and without the inclusion of the resonance field value at 9.6 GHz. The latter value falls below a line drawn through the other two points. This may be because the magnetisation is lower than the saturation value; as equation 4.1 shows this would lower the resonance field. On the other hand, the magnetisation will be fully saturated at the fields appropriate to the high frequency measurements. We believe, therefore, that the 2-point fit is likely to give more trustworthy values for the parameters.

The values for g agree within error. For the 38MgO and 78MgO samples we obtain g = 2.033 ± 0.004. This is significantly lower than the values at room temperature of 2.13 ± 0.04, 2.12 ± 0.04 and 2.09 ± 0.04 found [38] for one natural and two synthetic single crystals of Fe_3O_4. Only one other estimate of the g value has been made and that was by Atkas [9] who, for a 301.2nm thick Fe_3O_4 film on (100) MgO,

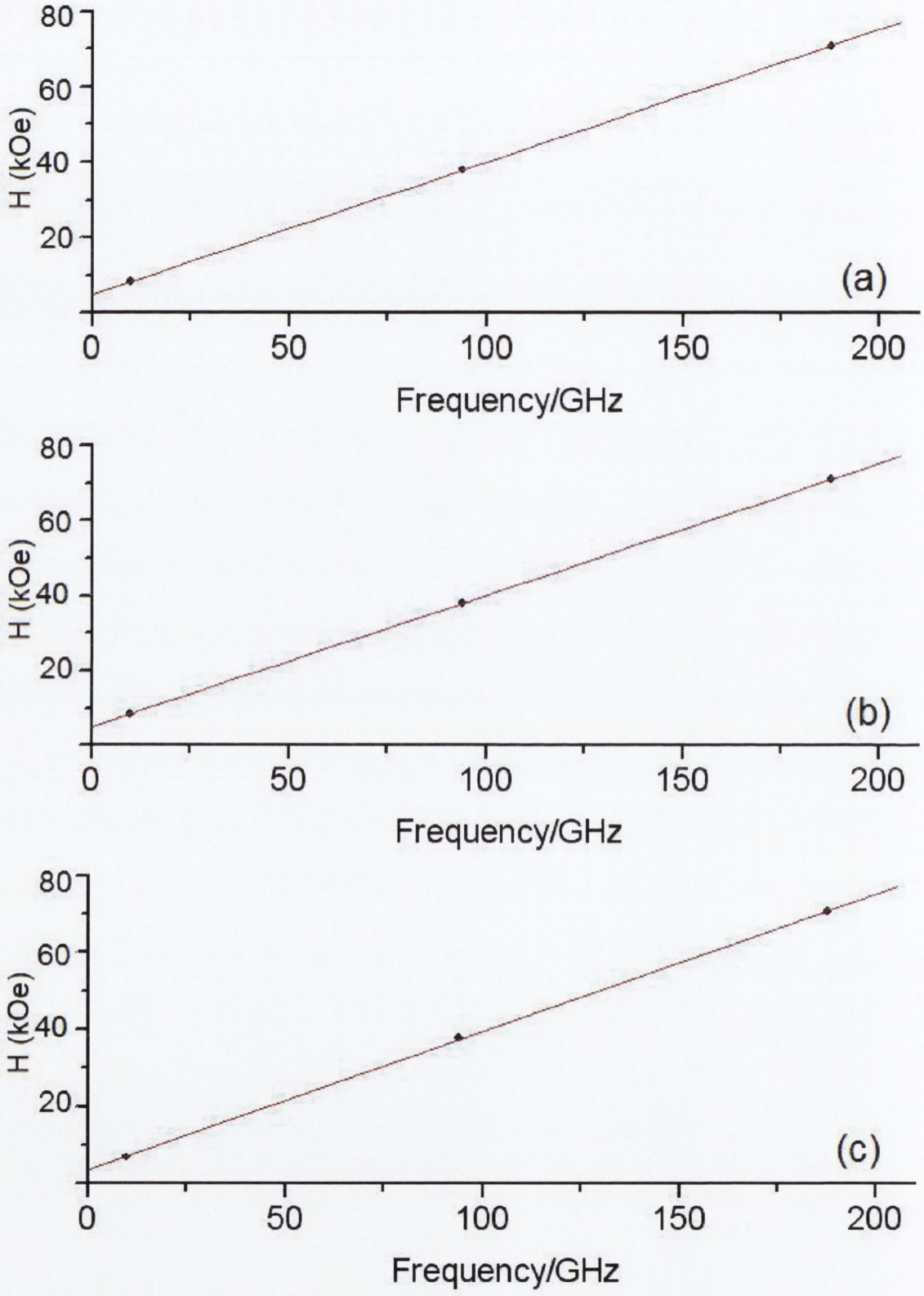

Figure 4.4: The dependence of resonance field on microwave frequency for samples (a) 38MgO, (b) 78Mgo and (c) 33MAO. Magnetic field is perpendicular to the film plane. Errors in field are $\pm$ 0.01 kOe

got 2.14; however this was obtained from a fit to the in-plane angular dependence of the resonance field – a fit that involved other adjustable parameters.

4.4.2 Angular dependence of the FMR signal at 9.6 GHz

Measurements were made at 9.6 GHz of the angular dependence of both the resonance field and the peak-to-peak linewidth, ΔH_{PP} for all five samples. The field was rotated both within the film plane i.e within the (100) plane, and out of the film plane but within the (001) plane.

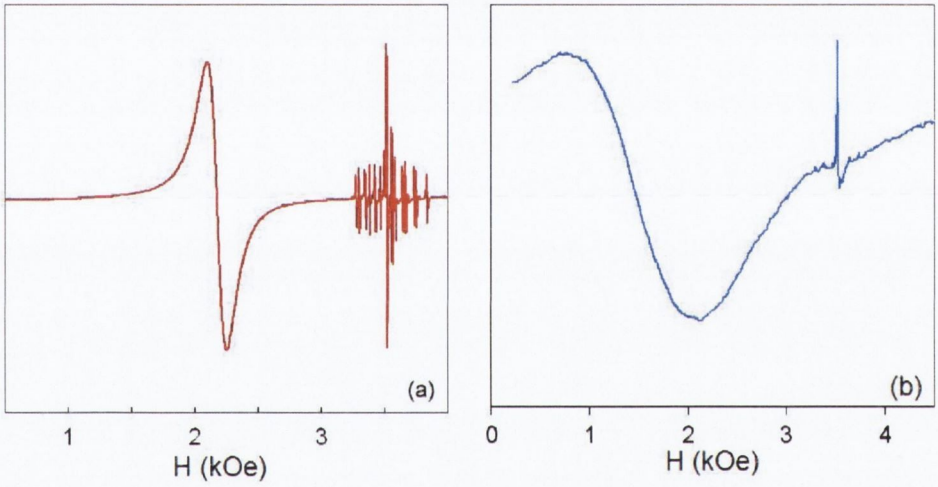

Figure 4.5: Spectra taken for field aligned along [010] direction for samples (a) 38MgO and (b) 33MAO. Microwave frequency = 9.6 GHz

Figure 4.5 shows some typical spectra taken at 9.6 GHz from two of the samples with the applied field aligned along the film [010] direction. These are representative of all of the signals at 9.6 GHz seen for films on MgO or MAO. Three distinct features are visible in each spectrum: the magnetite FMR signal (broadest line), the MgO:F^+ field marker EPR signal (strong narrow signal), and the substrate impurity (Manganese) EPR signal (a group of smaller narrow lines). It can be seen that for the film on MgO (Figure 4.5 (a)) the resonance signal is clear, and signal to noise ratio is high. The baseline is easily seen, and so the resonance position (H_R) was taken where the signal crossed the baseline. For the films on MAO (Figure 4.5 (b)), the signal to noise ratio is lower, and the baseline is not easily determined. Note also that the FMR signal is much broader, with linewidth over twice that observed for the films on MgO. Because in these cases the baseline was uncertain, H_R was taken as being the halfway point between the peaks of the resonance signal.

In all cases, the resonance linewidth (ΔH_{PP}) was calculated as the field difference between the resonance signal's maximum and minimum.

In Plane Rotation

Shown in figure 4.6 are examples of the spectra taken from each sample in this set of experiments - at $\phi_H = 0$, 45° and at an angle in between. In each case a single resonance signal was observed.

Figure 4.7 shows the angular dependence of H_R with respect to the in-plane direction of $\vec{H}$ for the three samples on MgO substrate. It can be clearly seen that the angular dependence has a period of 90°. The [011] direction, at $\phi_H = 45°$ is observed to be the easy axis of magnetisation (resonance observed at the lowest field value). This has been observed in previous studies [9,12,13]. It is also evident from these plots that the greatest variation in field values is occurs for the thinnest film (38 MgO), with a decrease as the films become thicker.

Figure 4.8 shows the corresponding angular dependence for the films on $MgAl_2O_4$. It should be noted here that, as the signals were broader and noisier in this case, the error in the position of H_R is higher. Where a baseline was uncertain, the resonance position was taken as the halfway point between the two peaks. Again we see the period of 90°, but the easy axis has now changed from [011] to [001]. This is a remarkable result, and has not been reported in any previously published studies. Another difference observed here in comparison to the results for the films on MgO is that a greater variation in H_R is seen for the thicker film, rather than for the thinner film as was observed for the films on MgO.

The angular dependence of the FMR linewidth of the films on MgO is shown in Figure 4.9. We can see that for the thinest film, at 38nm, the FMR linewidth varies in step with the angular variation of H_R, whereas for the thicker films, the maxima in H_R correspond to minima in ΔH_{PP}. In both cases, however, the angular dependence does show a 90° periodicity. It is noticeable that as the anisotropy in H_R increases then the mean linewidth decreases.

The linewidths for the films on $MgAl_2O_4$ are much larger (with average 1.3 kOe for sample 5MAO and 0.8 kOe for sample 33MAO), and show no discernible angular

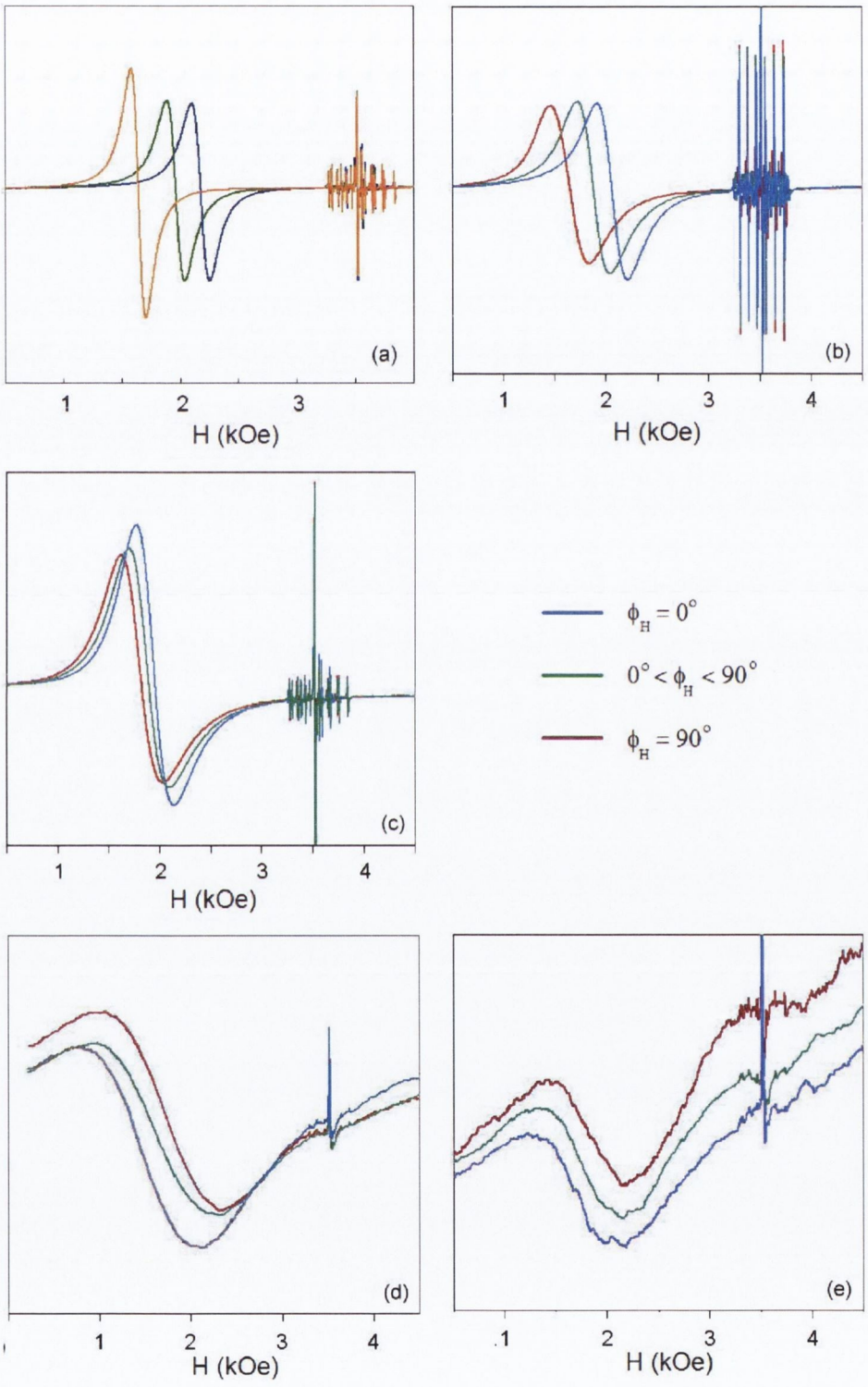

Figure 4.6: Spectra taken for $\vec{H}$ applied at three different directions within film plane for samples (a) 38MgO, (b) 78MgO, (c) 700MgO, (d) 33MAO and (e) 5MAO.

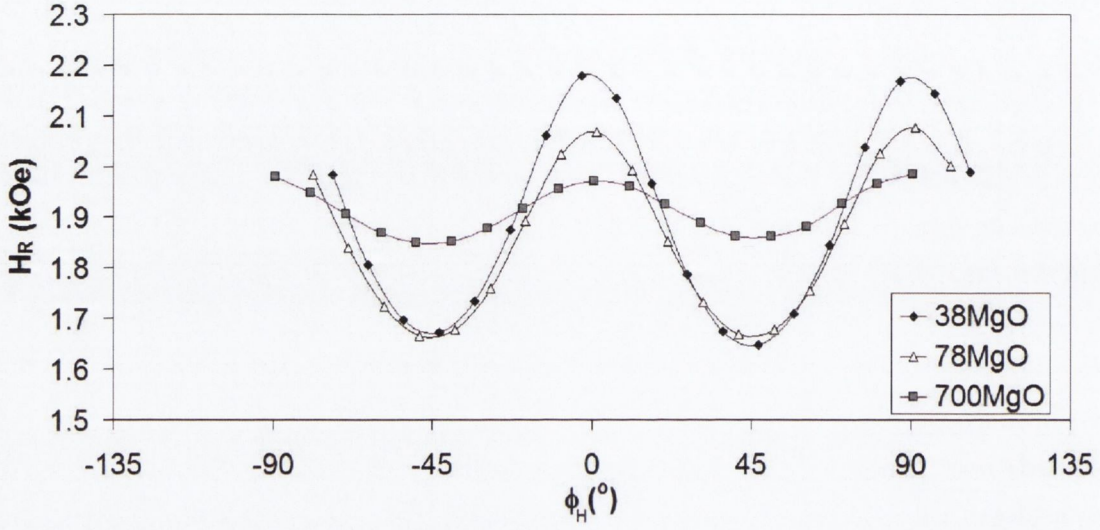

Figure 4.7: The in-plane ferromagnetic resonance field, H_R, as a function of angle ϕ_H for Fe_3O_4 on (100) MgO substrate with film thickness 38nm, 78nm and 700nm as indicated in the legend. Lines connecting the resonance field positions for each sample are included as a guide to the eye.

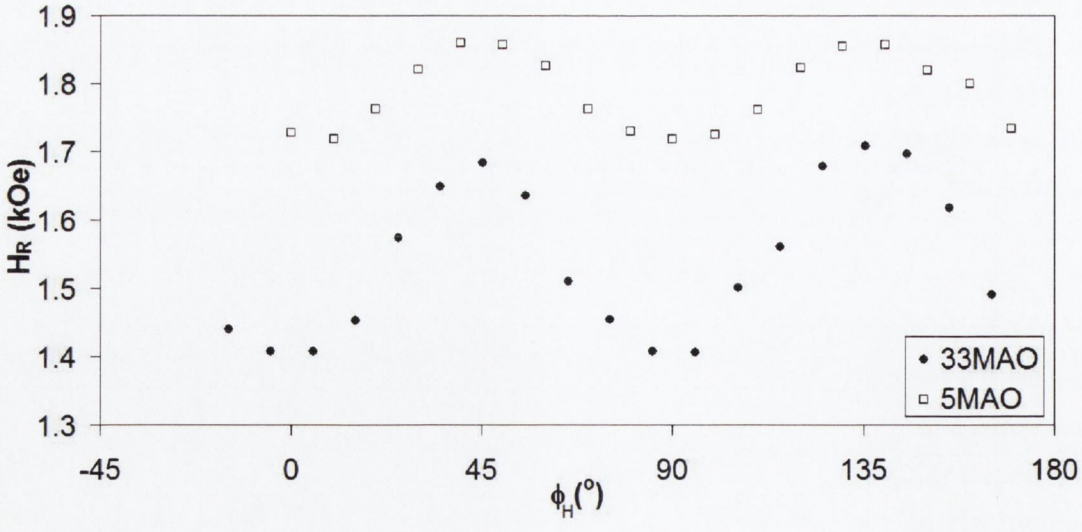

Figure 4.8: The in-plane resonance field, H_R, as a function of angle ϕ_H for Fe_3O_4 on (100) MAO substrate with film thickness 5nm and 33nm as indicated in the legend.

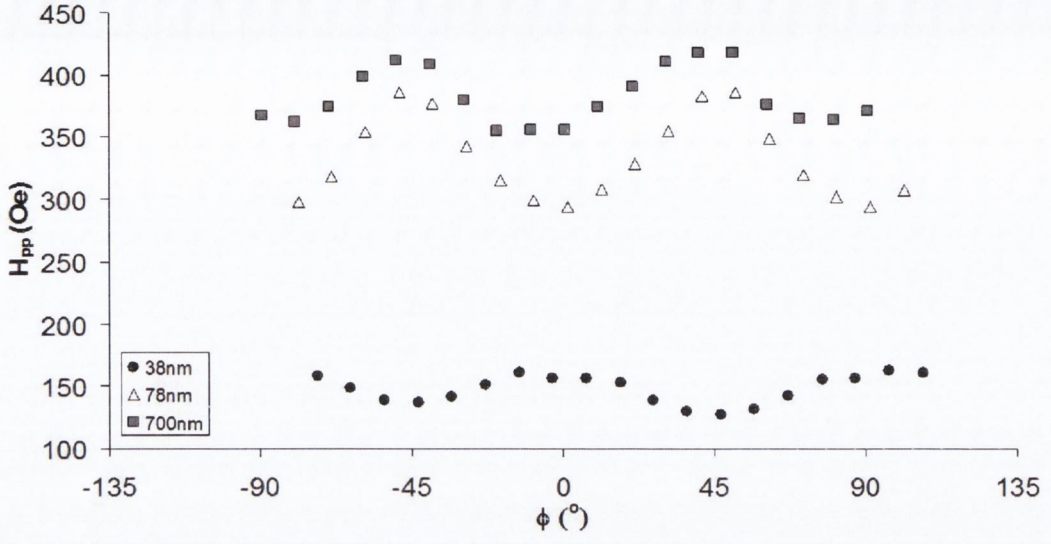

Figure 4.9: The in-plane FMR linewidth, ΔH_{PP}, as a function of angle ϕ_H for Fe_3O_4 on (100) MgO substrate with film thickness 38nm, 78nm and 700nm as indicated in the legend.

dependence, and hence are not shown.

Out of plane rotation

For this set of experiments we investigated the three samples on MgO, but only one sample on $MgAl_2O_4$ (33nm Fe_3O_4), as the signals given by the 5nm film were too weak and broad for accurate analysis.

Shown in figure 4.10 are spectra taken at various orientations for the four samples used. It can be seen from these that there is a large shift in the resonance positions between the two extreme alignments.

A problem encountered in this set of experiments was that the resonance field for the perpendicular alignment for some of the samples exceeded the upper limit of the magnet. This can be seen in plots (a) and (b) in figure 4.10, where the spectra taken around the zero degree mark have been cut off. In this case we measured as close as possible to the zero degree alignment, and then used this data to extrapolate to a field value for $\theta_H = 0$ by fitting to the theoretical model.

Resonance field position was taken to be where the spectrum crossed the baseline zero, as the baseline was easily ascertained in each case. In each case there is some

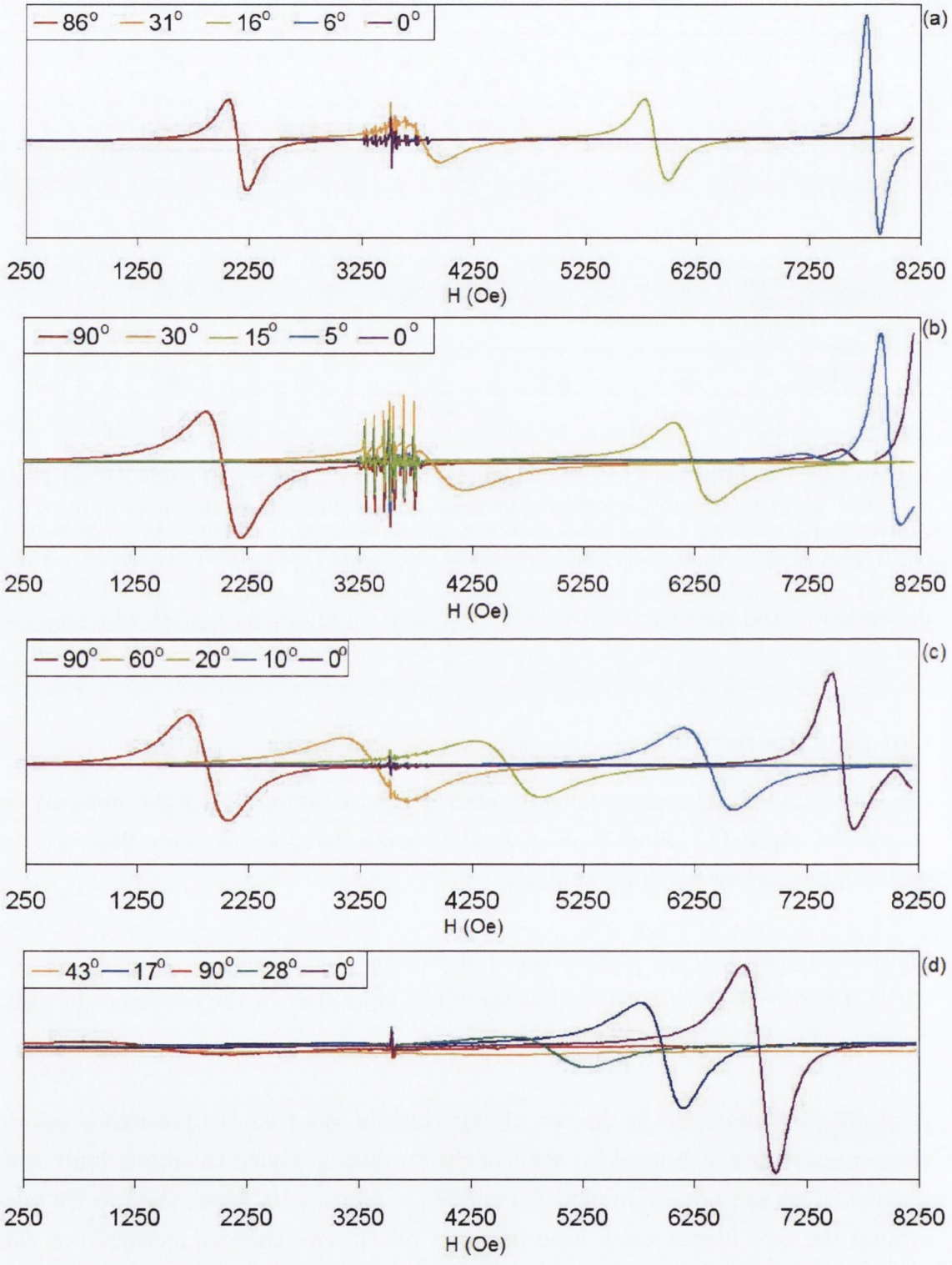

Figure 4.10: Spectra taken for $\vec{H}$ applied at different orientations out of the plane of the film (at values of θ_H given on the graphs) for samples (a) 38MgO, (b) 78MgO, (c) 700MgO, and (d) 33MAO

obscuring of the signal around the position of the impurity signal - this gave slightly higher uncertainty in reading the resonance position.

We note that there is extreme broadening of the signal between the extrema for the sample 33MAO (as can be seen in Figure 4.10.d) and so between angles 35° and 65° it was not possible to determine the resonance field. One possible reason for this broadening is the presence of two competing fields, trying to pull the magnetisation in opposite directions - the external magnetic field trying to pull the magnetisation out of plane, and the shape anisotropy, trying to keep the magnetisation in the plane of the film.
We also see that, for the 78nm and 700nm films on MgO, a second, weaker resonance signal is seen close to the perpendicular alignment ($\theta_H = 0$). In these cases, we take H_R to be the position of the stronger signal.

Shown in figure 4.11 are the field positions recorded for the four samples during the experiment. For all samples the resonance field varies from a maximum for $\vec{H}$ perpendicular to the film ($\theta_H = 0$) to a minimum at $\theta_H = 90°$. Field ranges are similar for the three MgO films. However, the resonance field values, for a given value of θ_H, for the sample on $MgAl_2O_4$ are seen to be lower. Also, for this sample, a slightly different trend is seen, with the field value falling less rapidly as θ_H increases.

The out-of-plane angular dependence of the FMR linewidths are shown in Figure 4.12. Similar behaviour is seen in all cases, with minima being observed at the extreme orientations ($\theta_H = 0$ and 90°) and with a maximum between. In the case of the sample deposited on $MgAl_2O_4$, however, we see that the minimum at $\theta_H = 0°$ is much lower than the values observed at the in-plane orientation. Again, here, some data values are missing as the line became too broad to resolve in the region of $\theta_H = 45°$.

4.5 Analysis

As described in Section 3.2.5 we begin with the appropriate expression for the magnetic free energy density of an epitaxial Fe_3O_4 film. Due to the lattice mismatch between magnetite and both the MgO and MAO substrates there may exist a slight tetragonal distortion and so the perpendicular and parallel cubic anisotropy fields $H_{\parallel}$ and $H_{\perp}$ may be unequal. The expression for E also includes the possibility of

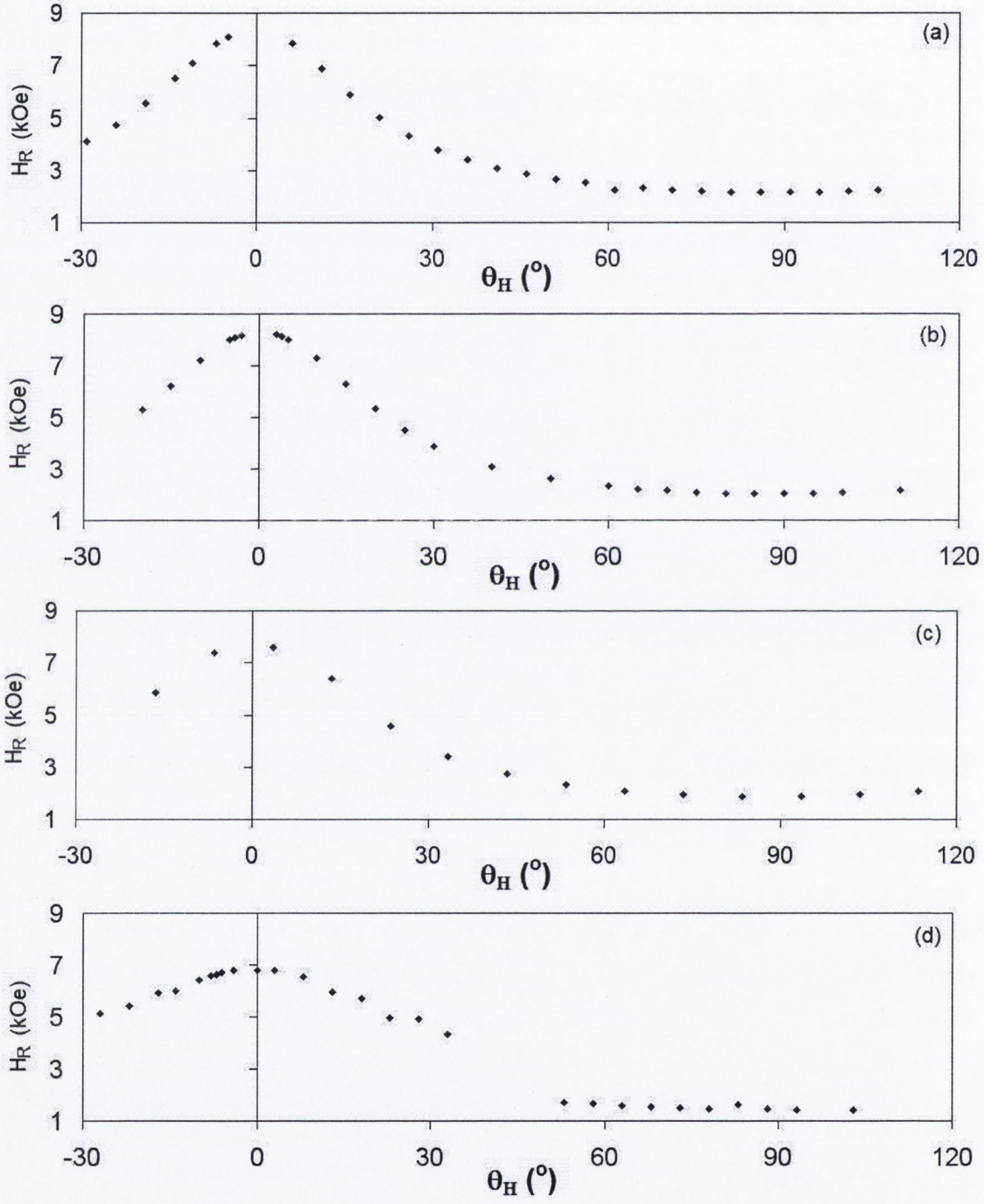

Figure 4.11: Angular dependence of H_R recorded during out of plane rotation for samples (a) 38MgO, (b) 78MgO, (c) 700MgO, and (d) 33MAO

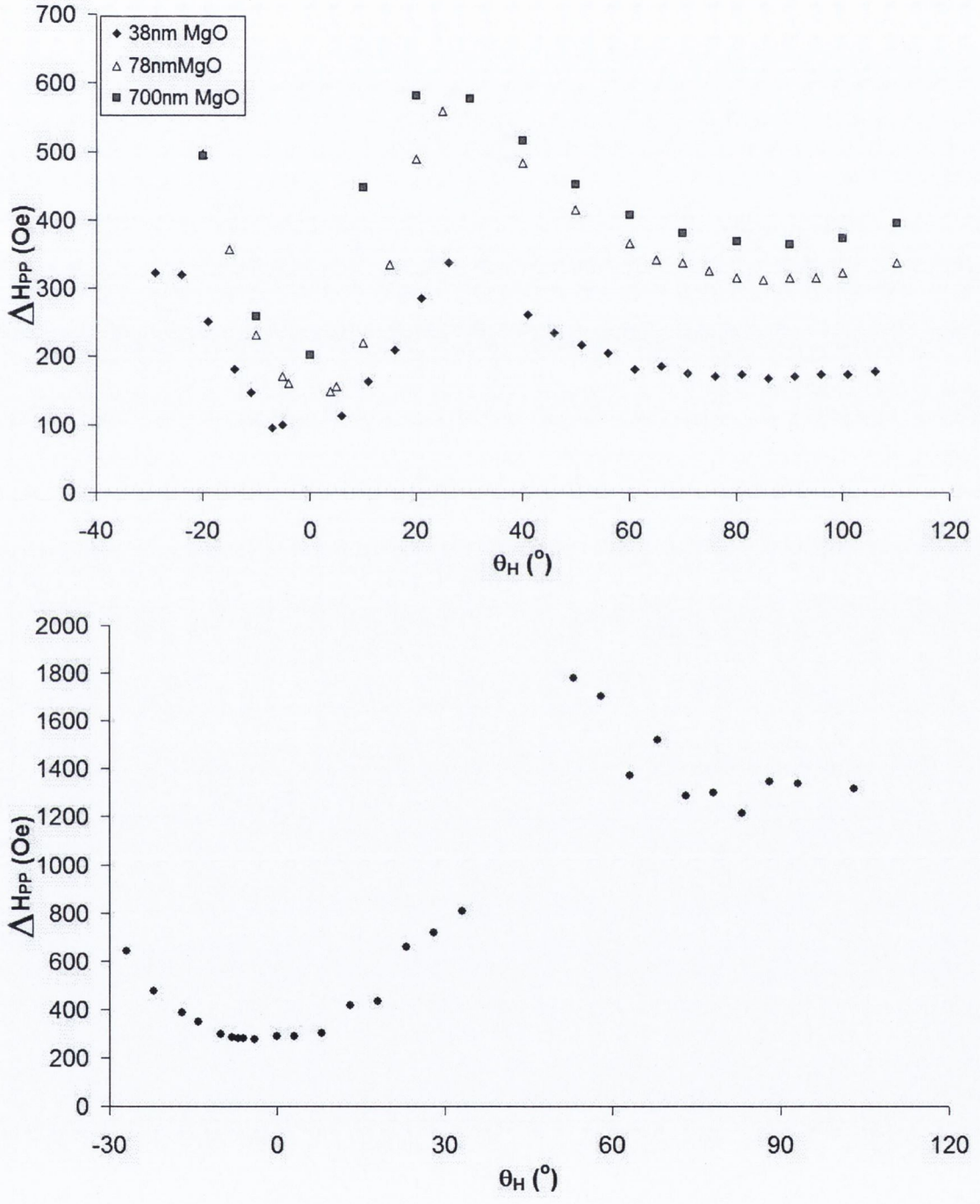

Figure 4.12: Angular dependence of ΔH_{PP} recorded during out of plane rotation for samples (a) 38MgO, 78MgO, and 700MgO, and (d) 33MAO

the existence of a perpendicular uniaxial anisotropy field $H_{2\perp}$. As shown in Section 3.2.5, for such films the free energy density can be given by:

$$\begin{aligned} E &= \frac{1}{2}M[-2H\left(\cos\theta\cos\theta_H + \sin\theta\sin\theta_H\cos(\phi-\phi_H)\right) + 4\pi M\cos^2\theta \\ &\quad -H_{2\perp}\cos^2\theta - \frac{1}{2}H_{4\perp}\cos^4\theta - \frac{1}{2}H_{4||}\frac{1}{4}\left(3+\cos 4\phi\right)\sin^4\theta] \end{aligned} \tag{4.2}$$

with θ, θ_H, ϕ, ϕ_H as shown in figure 4.1, and $H_i = 2K_i/M$.

For a specific orientation of the applied field the equilibrium position of the magnetisation vector is found by minimising the free energy with respect to ϕ and θ; that is, we set $\partial E/\partial\phi$ and $\partial E/\partial\theta$ to zero. This implies that for the out of plane orientation and with $\vec{H}$ lying within the (001) plane with $\phi = \phi_H = 0°$:

$$H\sin(\theta_H-\theta) - \cos\theta\sin\theta(4\pi M_{eff} + H_{4||}\sin^2\theta - H_{4\perp}\cos^2\theta) = 0 \tag{4.3}$$

where $4\pi M_{eff} = 4\pi M - H_{2\perp}$. For the in-(100)-plane orientation ($\theta = \theta_H = 90°$):

$$H\sin(\phi-\phi_H) + 0.25H_{4||}\sin 4\phi = 0 \tag{4.4}$$

The resonance condition can be derived using the Suhl or Smit and Beljers equation, as given in Section 3.2.5:

$$\left(\frac{\omega}{\gamma}\right)^2 = \left(\frac{1}{M\sin^2\theta}\frac{\partial^2 E}{\partial\theta^2}\right)\times\left(\frac{1}{M}\frac{\partial^2 E}{\partial\phi^2}\right) - \left(\frac{1}{M\sin\theta}\frac{\partial^2 E}{\partial\theta\partial\phi}\right)^2 \tag{4.5}$$

yielding the following resonance conditions for the in-plane case:

$$\left(\frac{\omega}{\gamma}\right)^2 = \left(H\cos(\phi-\phi_H) + 4\pi M_{eff} + H_{4||}\frac{3+\cos 4\phi}{4}\right)\times\left(H\cos(\phi-\phi_H) + H_{4||}\cos 4\phi\right)$$

As will be clear later it is valid to take $H >> H_{4||}$ and therefore equation 4.4 implies that for the in-plane case $\phi \approx \phi_H$. Therefore the resonance condition becomes

$$\left(\frac{\omega}{\gamma}\right)^2 = \left(H + 4\pi M_{eff} + H_{4||}\frac{3+\cos 4\phi}{4}\right)\times\left(H + H_{4||}\cos 4\phi\right) \tag{4.6}$$

For the out of (100) plane case (but within (001) plane) the resonance condition is:

$$\left(\frac{\omega}{\gamma}\right)^2 =$$
$$\left(H\cos\left(\theta-\theta_H\right)-\left[4\pi M_{eff}-\frac{H_{4\perp}}{2}+\frac{H_{4||}}{2}\right]\cos 2\theta+\left[H_{4\perp}+H_{4||}\right]\frac{\cos 4\theta}{2}\right)$$
$$\times\left(H\cos\left(\theta-\theta_H\right)-\left(4\pi M_{eff}+2H_{4||}\right)\cos^2\theta+\left(H_{4||}+H_{4\perp}\right)\cos^4\theta+H_{4||}\right) \tag{4.7}$$

4.5.1 In-Plane Angular Dependence

The experimental results shown in Figures 4.7 and 4.8 were fit to Equation 4.6 using Origin 5.0. The parameter $(\omega/\gamma)^2$ was calculated using the frequency averaged over all values taken during experiments on that sample (though the variation was less than 0.01% in all cases, and less than 0.001% in the cases of the films on MgO). We made separate calculations using the accepted bulk g-value of 2.12 [38], and for the g-value of 2.03 which was calculated from the frequency dependence experiments (section 4.4.1). The data fit the theoretical model equally well for both values of g - the theoretical field values generated were the same, with fit parameters being slightly different to compensate for the change in $(\omega/\gamma)^2$. The theoretical fit for all five samples are shown in figures 4.13-4.17.

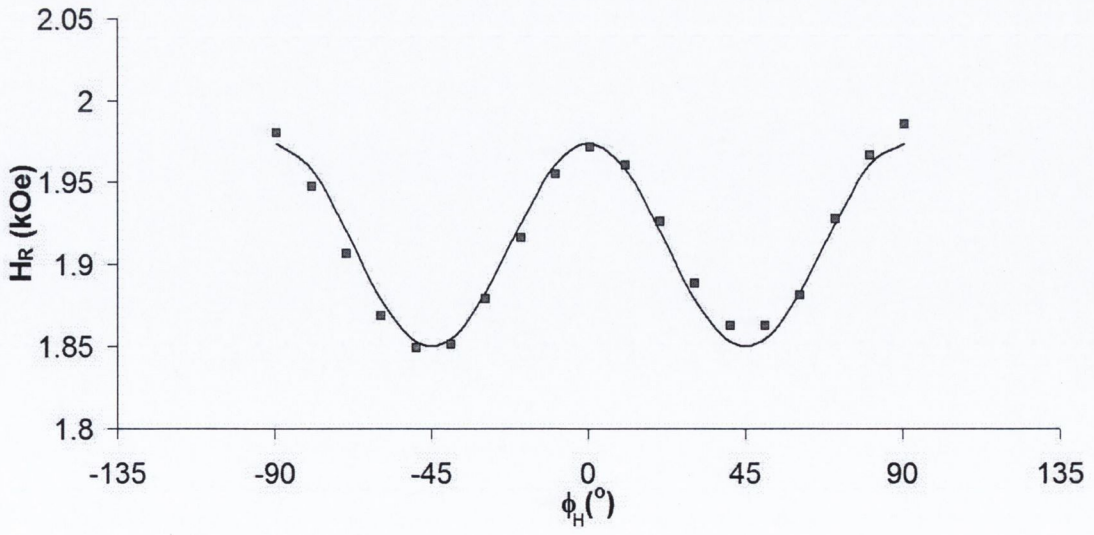

Figure 4.13: In-plane angular dependence of resonance field for sample 700MgO. The line is the fit using parameters given in tables 4.3 and 4.4

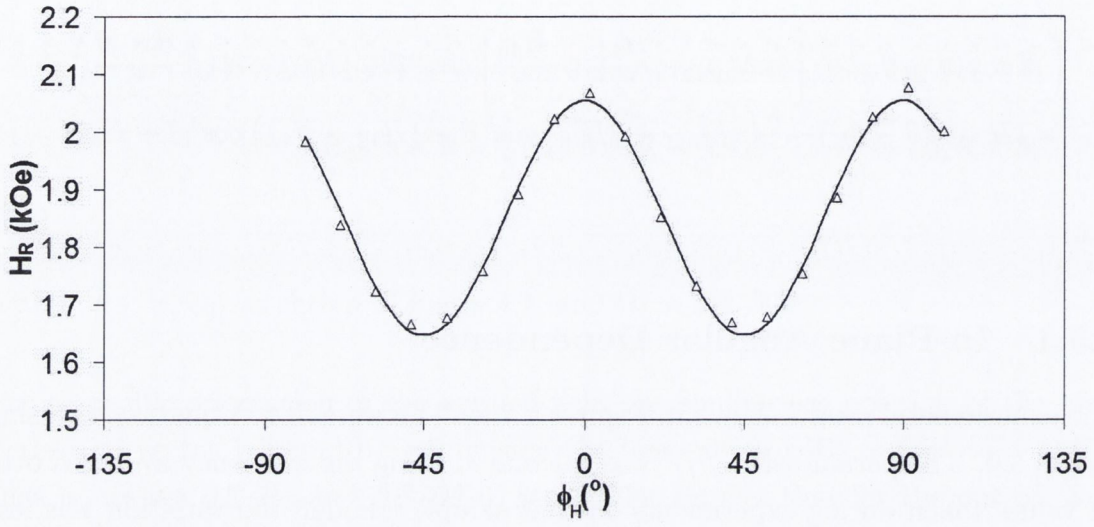

Figure 4.14: In-plane angular dependence of resonance field for sample 78MgO. The line is the fit using parameters given in tables 4.3 and 4.4

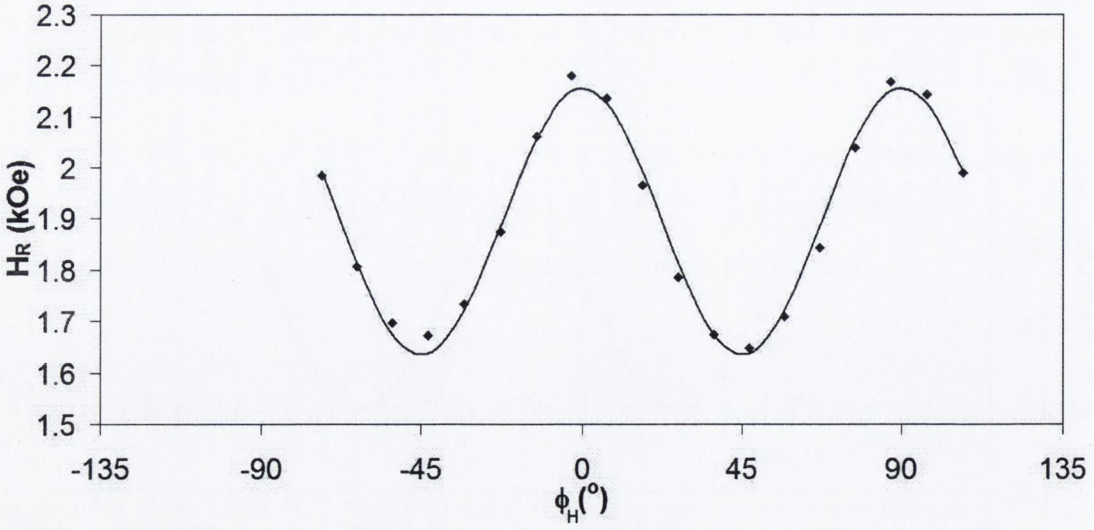

Figure 4.15: In-plane angular dependence of resonance field for sample 38MgO. The line is the fit using parameters given in tables 4.3 and 4.4

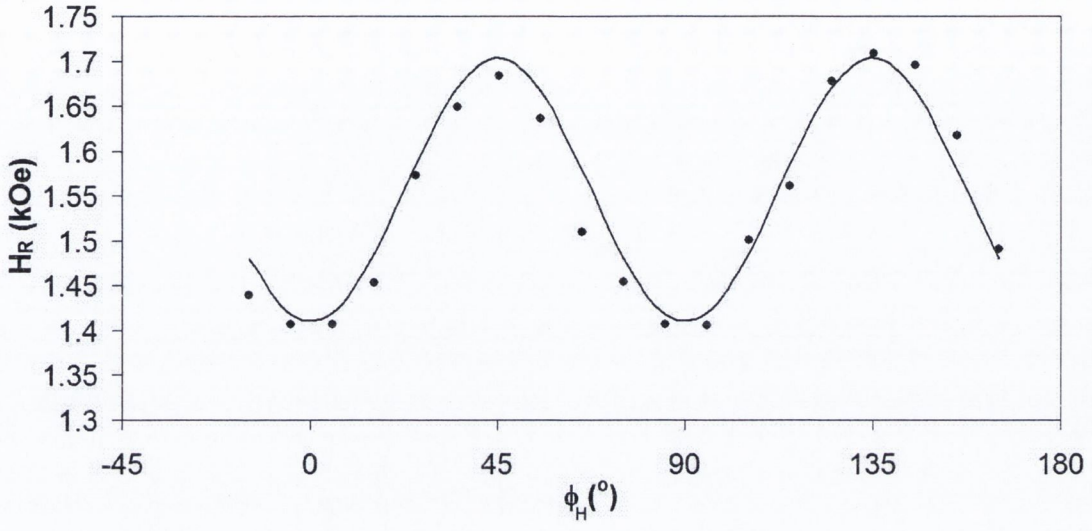

Figure 4.16: In-plane angular dependence of resonance field for sample 33MAO. The line is the fit using parameters given in tables 4.3 and 4.4

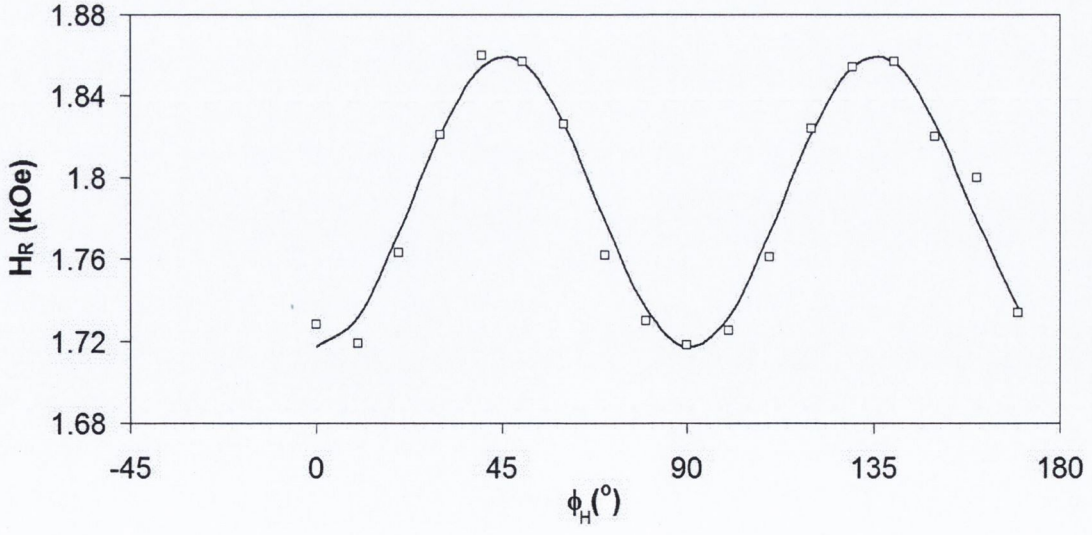

Figure 4.17: In-plane angular dependence of resonance field for sample 5MAO. The line is the fit using parameters given in tables 4.3 and 4.4

Parameters extracted were the anisotropy field ($2K_{4||}/M$), and $4\pi M_{eff}$; their values are given in tables 4.3 and 4.4.

Table 4.3: Parameters obtained from fits to in-plane angular dependence of H_R with g-value 2.12

	$\frac{2K_{4\|\|}}{M}$ (Oe)	$4\pi M_{eff} = 4\pi M - 2\frac{K_{2\perp}}{M}$ (kOe)
38MgO	-319 ± 9	4.19 ± 0.03
78MgO	-249 ± 6	4.21 ± 0.02
700MgO	-74 ± 3	3.88 ± 0.02
33MAO	170 ± 7	5.29 ± 0.03
5MAO	86 ± 3	4.22 ± 0.01

Table 4.4: Parameters obtained from fits to in-plane angular dependence of H_R with g-value 2.03

	$\frac{2K_{4\|\|}}{M}$ (Oe)	$4\pi M_{eff} = 4\pi M - 2\frac{K_{2\perp}}{M}$ (kOe)
38MgO	-315 ± 9	4.71 ± 0.03
78MgO	-244 ± 6	4.86 ± 0.02
700MgO	-75 ± 3	4.49 ± 0.02
33MAO	168 ± 7	6.28 ± 0.03
5MAO	85 ± 4	4.90 ± 0.01

For the case of the films deposited on MgO, the cubic anisotropy term $K_{4||}$ is negative, and it decreases as the film thickness is increased. The values differ only slightly for the fits using g = 2.12 and 2.03. The negative sign gives the easy axis along [110] type directions, and this is as has been previously observed for such films [9,12,13].

In contrast to the films on MgO, those deposited on MAO have a positive $2K_{4||}/M$ corresponding to an easy axis along [010] type directions. This is a remarkable result, and is contrary to what has been observed in previous studies [9,12]. To ensure that no mistake had been made, we carried out XRD measurements on the samples to ensure that our directions were correct, and we found the samples were as we initially believed. It is not apparent why such a huge change in the film's characteristics should be seen in this case. In another contrast to the films on MgO, the $2K_{4||}/M$ increases from 85/85 Oe to 168/170 Oe with an increase in film thickness from 5 to 33 nm.

The quantity which does change greatly between the fits with g = 2.12 and g = 2.03 is $4\pi M_{eff}$, with much higher values where the g value is taken to be 2.03. For both

cases we observe very similar values of $4\pi M_{eff}$ for the 38nm and 78nm, but with a lower value for the 700nm film. For the samples on MAO, however, the greatest value for $4\pi M_{eff}$ is observed for the thickest film. In both cases the values for the samples on MAO are greater than those for the samples on MgO. We will compare these values with the results obtained for the out of plane rotation in section 4.5.2.

4.5.2 Out of Plane Angular Dependence

The observed angular dependencies of H_R for variation in θ_H (but within the (001) plane) were fit to the theoretical model using equations 4.3 and 4.7.

To obtain the best fit of the angular dependence of resonance field we perform iteration of a calculation using equations 4.3 and 4.7. We began with by substituting the experimentally observed values for H into equation 4.3, which gave us an estimate of $\theta - \theta_H$. We then used this estimate to extract a value of H from equation 4.7, which we used as the starting value for the next iteration. We continued this process until we obtained a value of H for which equations 4.3 and 4.7 were mutually consistent. For $H_{4||}$ and $H_{4\perp}$ we took the values given in tables 4.3 and 4.4. It can be noted that the value for $4\pi M_{eff}$ dictates the difference between maximum and minimum H_R for the fit, and are not affected by the choice of g. The value of g (giving the value for γ) dictates the fit's mean H_R.

Shown in figures 4.18, 4.19 and 4.20 are plots of the experimental results for the three magnetite films deposited on MgO, along with fits using the theoretical model with different g-values (bulk g-value 2.12, and the value calculated using high field/varying frequency data, 2.03). The values of $4\pi M_{eff}$ obtained from the fits are shown in Table 4.5.

Table 4.5: Values of $4\pi M_{eff}$ obtained from fits to the out of plane angular dependence of H_R

	$4\pi M_{eff}(kOe)$
38MgO	4.6 ± 0.1
78MgO	4.7 ± 0.1
700MgO	4.3 ± 0.1
33MAO	4.0 ± 0.1

A similar graph and fits are shown in figure 4.21 for sample 33MAO. No readings could be taken for $\theta_H = 45°$, 50° and 55° as explained before.

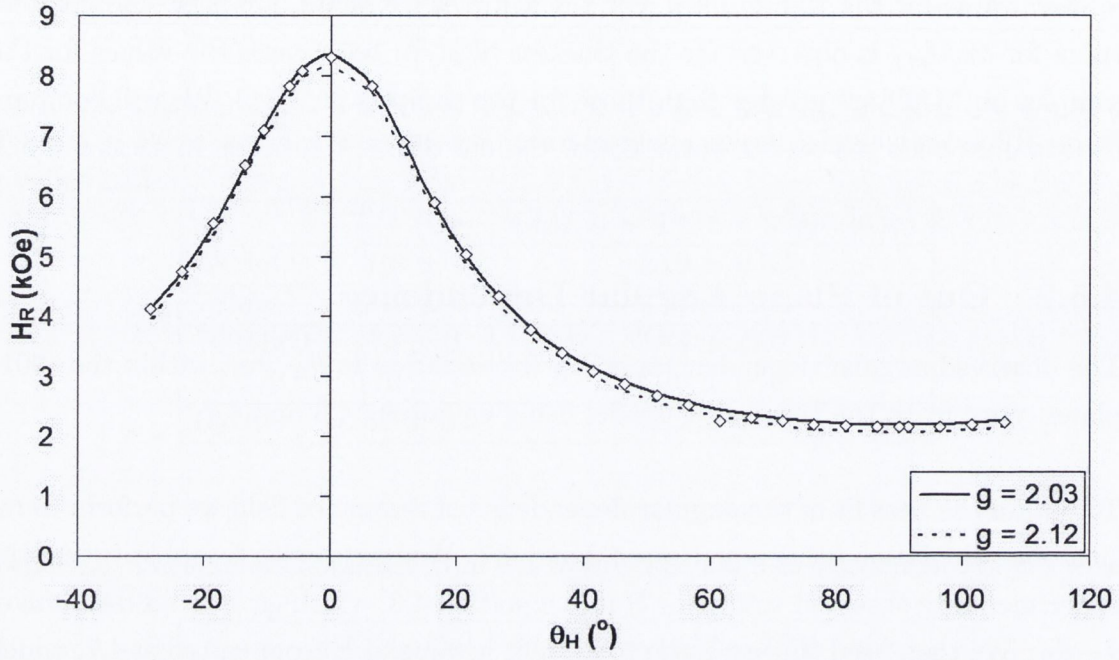

Figure 4.18: Out of plane angular dependence of H_R for sample 38MgO. Fits are shown both for g = 2.12 and 2.03

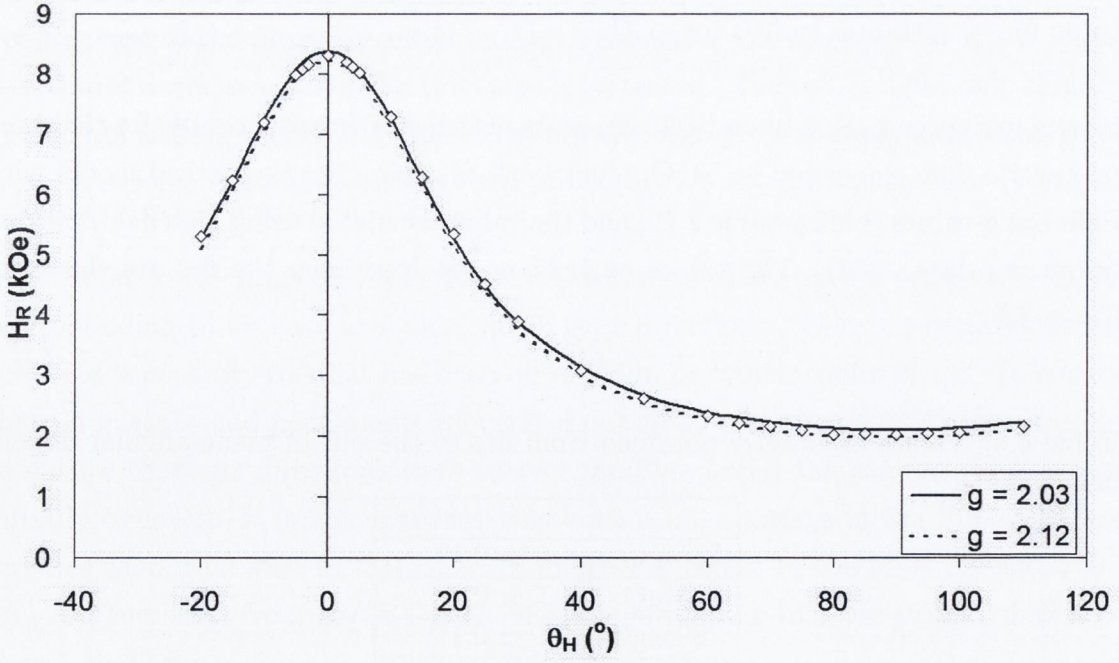

Figure 4.19: Out of plane angular dependence of H_R for sample 78MgO. Fits are shown both for g = 2.12 and 2.03

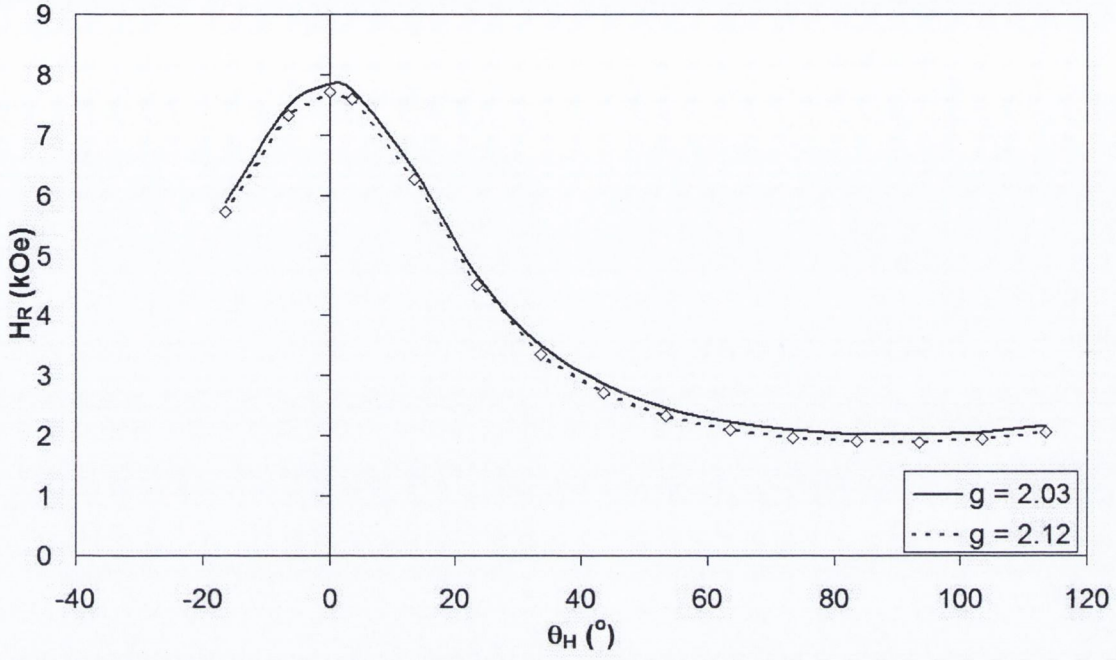

Figure 4.20: Out of plane angular dependence of H_R for sample 700MgO. Fits are shown both for g = 2.12 and 2.03

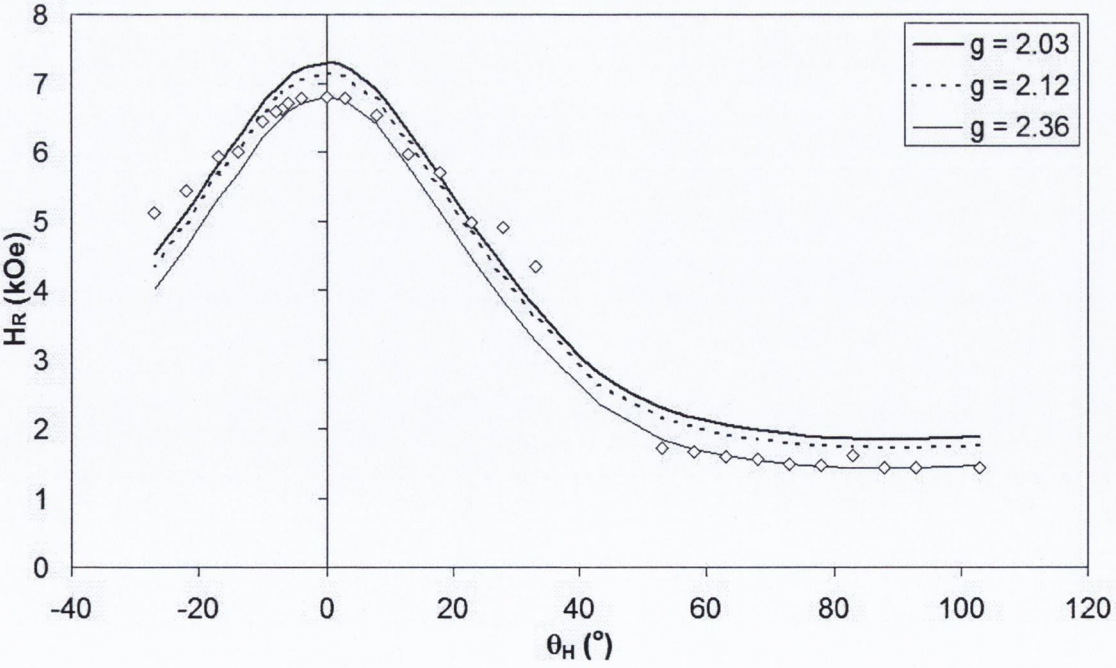

Figure 4.21: Out of plane angular dependence of H_R for sample 33MAO. Fits are shown both for g = 2.12 and 2.03, and with best fit value, g = 2.36

The values for $4\pi M_{eff}$ obtained from fits are shown in Table 4.5; they are in the same range as those calculated in the in-plane experiments.

From the plot 4.21 it can be seen that the theoretical model does fit the data for the film on MAO as well as it does for the films on MgO. The best fit is achieved for a g-value of 2.36 - this does not agree with what we have found previously, giving further evidence that the out-of-plane model used does not fit for this case. It is possible that $\theta \neq 0$ for $\theta_H = 0$ - this would cause H_R to be lower for θ_H in the region of 0, and so would result in the type of distortion observed.

4.5.3 Linewidth

It is clear from Figure 4.9 that, for the films deposited on MgO, varying the angle ϕ_H has an effect on the FMR peak-to-peak linewidth, ΔH_{pp}, and that this effect is different for films of different thickness. In each case the angular dependence has a 90° periodicity, as is observed for the angular dependence of H_R. However, in the case of the 38nm film, the linewidth varies in step with H_R, while for the case of the thicker films, the linewidth shows maxima where H_R shows minima, and vice versa.

As explained in Section 3.2.7 we can express the linewidth as

$$\Delta H_{pp} = \Delta H_{hom} + \Delta H_{inhom}$$

where the homogeneous contribution, ΔH_{hom}, arises from the intrinsic damping of the magnetisation and ΔH_{inhom} comes from the magnetic inhomogeneities of the sample; both can have an angular dependence. The homogeneous contribution is given by [59,61]

$$\Delta H_{hom} = \frac{1}{\sqrt{3}} \frac{1}{|\partial\omega/\partial H|} \frac{G}{M^2} \left(\frac{\partial^2 E}{\partial \theta^2} + \frac{1}{\sin^2\theta} \frac{\partial^2 E}{\partial \phi^2} \right) \tag{4.8}$$

where G is the Gilbert damping parameter. Evaluating this, we find that the angular dependence of this contribution is given by a $\cos(\phi - \phi_H)$ term. Since in our case we estimate that $\phi \approx \phi_H$, $\cos(\phi - \phi_H) \approx 1$, and so this contribution is almost constant and could not be the cause of the angular variation of the linewidth. It will, however, have an effect on the mean value of ΔH_{PP}.

Another possibility is that the angular dependence of the linewidth comes from

the inhomogeneous contribution ΔH_{inhom}. The magnetic inhomogeneities, arising from sample imperfections, such as mosaic structure and defects, can give rise to a distribution in the directions of both the crystal and magnetic anisotropy axes as well as a spread in the magnitudes of the internal fields. So, following Chappert et al [62], we write

$$\Delta H_{inhom} = \Delta H_0 + \sum_i \frac{\partial H_R}{\partial \phi_i} \Delta \phi_i + \sum_j \frac{\partial H_R}{\partial H_j} \Delta H_j \tag{4.9}$$

For our case we are only considering the in plane variation and so the angular spread $\Delta\phi_i$ includes spreads in the direction of the axes of the cubic and uniaxial anisotropy and ΔH_j includes spreads in $H_{4||}$, and M_{eff}. Using equations 4.6 and 4.9, and the parameters values given in Tables 4.3 and 4.4, we can calculate the angular dependencies that would be produced by these spreads. It is clear that a spread in the angle ϕ_H or in the cubic anisotropy field $H_{4||}$ can not be the cause of the angular variation of ΔH_{PP} as as these both have a 45° periodicity, giving minima or maxima (ϕ_H and $H_{4||}$ respectively) along ϕ_H = (0, 45°, 90°,...). The remaining contribution, a spread in $4\pi M_{eff} = 4\pi M - 2K_{2\perp}/M$ does show a 90° periodicity, with maxima along ϕ_H = (45°, 135°,...). This fits with the angular dependence that we observe for the two thicker films. However, we were unable to fit the angular dependence to this contribution, as the percentage ripple predicted for the dH/dM_{eff} contribution is much too low. None of the possible contributions are predicted to have the same angular dependence as the 38nm film (with maxima at ϕ_H = (0, 90°,...)).

For the out of plane rotation, we find similar results for all films investigated — namely, ΔH_{PP} exhibits local minima at $\theta_H = 0$ and 90°, with a maximum between. For the films on MgO, this maximum is in the region θ_H = 20-30°, while for the 33nm film on MAO, the maximum is observed for a higher value, θ_H = 40-50°. Using equations 4.8, 4.9 along with 4.7, we can calculate the angular dependencies of the both the intrinsic (homogeneous) and inhomogeneous linewidth contributions. Evaluating these we find that two of the possible contributions can be discounted — a spread in $K_{4||}$, which would give an almost linear increase in the linewidth from $\theta_H = 0$ to $\theta_H = 90°$, and a spread in $K_{4\perp}$, which gives a minimum in the region $\theta_H \approx$ 15-25°. It is possible that the former is having some effect, as we do observe in each case that the linewidth in the parallel alignment is greater than that in the perpendicular alignment – however, it is clear that it cannot be the primary contribution to the angular dependence.

The remaining two contributions, the homogeneous linewidth, and a spread in the

angle θ_H, both give a maximum at $\theta_H \approx 25°$, and so it is likely that these could be contributing to the observed linewidth for the films on MgO. However neither of these separately, nor a combination of the two, can be used to give a satisfactory fit to the observed linewidth, for the following reasons: as regards the homogeneous linewidth, its curvature about the maximum is not as sharp as that experimentally observed. The form of the contribution from a spread in θ_H is much closer to that observed, being always nonzero, and with a sharper curvature near the maximum. However, the difference between the maximum and minimum is much smaller than that observed experimentally (with maximum $\approx$ 140% of the minimum, in comparison to the 285-375% observed).
As regards the linewidth results observed for sample 33MAO, the large increase in ΔH_{PP} between $\theta_H = 0$ and 90° may be somewhat attributed to a spread in $K_{4\|}$, as mentioned above, which could arise from misfit dislocations in the material caused by the larger lattice mismatch between magnetite and MAO. The sharp increase in linewidth in the region θ_H = 40-50°, however, cannot be explained by any of the factors discussed above.

One factor which could be responsible for the observed angular dependencies in the out of plane linewidth, is two-magnon scattering, as described by Rantschler et.al [69]. For the case of transition metal doped permalloy films, the two-magnon scattering contribution to the linewidth is calculated to show a maximum at $\phi_H \approx$ 15°, and exhibits an angular dependence very similar to what we observe. A greater linewidth for $\theta_H = 90°$ than for $\theta_H = 0$ is also attributed to two-magnon scattering [69].

4.5.4 Discussion

We will now discuss briefly the results presented in tables 4.3, 4.4 and 4.5, and their implications.

Firstly, comparing the values for $4\pi M_{eff}$ in tables 4.3, 4.4 and 4.5, we see that the values obtained using g = 2.03, shown in table 4.4 agree much better with those shown in table 4.5 than do those for g = 2.12. Examining the fits shown in Figures 4.18, 4.19 and 4.20, we can also see that taking g = 2.03 gives a better fit to the theoretical model for sample 38MgO than taking g = 2.12, and for sample 78MgO, the fits are equally good for both values of g. This further supports the result obtained from the analysis of the high-frequency studies performed previously (presented in

section 4.4.1), that the g-value of the films is lower than the value of 2.12 reported for bulk magnetite [38], and the value of 2.14 estimated for a magnetite film by Atkas [9].

We will now discuss the values of $H_{4\|}$, given in tables 4.3 and 4.4. For the case of the films deposited on MgO, the cubic anisotropy term $K_{4\|}$ is negative, giving the easy axis along [110] type directions, and this is as has been previously observed for such films [9,12,13]. The values of $2K_{4\|}/M$ of -75 to -315 Oe are less than those of -380 Oe [13] and -440 Oe [65] previously reported for films of Fe_3O_4 deposited by MBE on MgO, and also lower than the bulk value of -466 Oe [38]. However, as mentioned previously, there have been a wide variety of results published, and, for sputtered films, values of -22 Oe for a 301 nm film [9] and 0 for films below 60nm [12] have been reported. Atkas [9] proposes a model to account for the nonsaturation of the film's magnetisation at the field values used in the FMR procedure, which substitutes a gaussian distribution of spins within a solid angle about $\vec{H}$ for the aligned spins of a saturated sample. Using this model, a theoretical calculation taking $2K_{4\|}/M$ = -466 for 100% saturation gives, for a 10% decrease in M, an 80% decrease in $2K_{4\|}/M$. This could account somewhat for the lower values observed, as we expect that the magnetisation of the samples is far from saturation at the low fields used.
For films on MgO we observe a decrease in $H_{4\|}$ with an increase in film thickness, which is opposite to what has been observed by other authors [10,12,13]. It is important to note however, that on examination of the linewidths observed (Figure 4.9), we see that the highest value of $H_{4\|}$ is present for the film with the lowest average linewidth (namely 38MgO), and vice versa (700MgO). We expect that with an increase in the magnetic order within a material, the observed linewidth should decrease, or in our case, that the linewidth should be indicative of the quality of the film. This is further supported by the measurements taken at 94GHz, as shown in Figure 4.2. Here, sample 38MgO, shows a clean narrow symmetric line, while that observed for 78MgO is wider with weaker lines clearly present, and that observed for 700MgO is wider again and is clearly the combination of at least two lines. The presence of more than one resonance signal suggests inhomogeneity in the material of the films. We suggest that that it is this inhomogeneity that causes the reduction in observed $H_{4\|}$, as an appreciable decrease in the magnetic ordering of the magnetite should surely dilute the magnetocrystalline anisotropy.

In contrast to the films on MgO, those deposited on MAO have a positive $2K_{4\|}/M$ corresponding to an easy axis along [010] type directions. This is a remarkable result, and is contrary to what has been observed in previous studies [9,12]. It is not

apparent why such a huge change in the film's characteristics should be seen in this case. Again the magnitude of $2K_{4||}/M$ is lower than the bulk value of -466 Oe [38].

In another contrast to the films on MgO, the magnitude of $2K_{4||}/M$ increases from 85/85 Oe to 168/170 Oe with an increase in film thickness from 5 to 33 nm. We can apply the same reasoning as before, namely that the observed anisotropy is linked to the film quality — although for this case it is the thinner film which shows the lower $H_{4||}$, and also the lower ΔH_{PP} at 9.6 GHz, it is clear to see from Figure 4.6 that the spectra observed for sample 33MAO are of far better quality. This is also evidenced by the fact that spectra taken from sample 5MAO in the out of plane rotation were of too low quality for analysis.

4.5.5 Conclusions

Fe_3O_4 films deposited on MgO show a decrease in cubic anisotropy with an increase in film thickness, with the cubic anisotropy field $H_{4||}$ decreasing from –315 Oe to –75 Oe with an increase in film thickness from 38 to 700nm. We propose that the decrease in cubic anisotropy is due to a decrease in film quality with increase in thickness, as is evidenced by an increase in the mean linewidth.
Fe_3O_4 films deposited on $MgAl_2O_4$ showed the remarkable property of having their easy axis orientated along [100] type direction, as opposed to the [110] type directions expected. It is not clear what could cause this change. The cubic anisotropy in this case increased with an increase in the film thickness, with the cubic anisotropy field $H_{4||}$ increasing from 85 Oe to 168 Oe with an increase in film thickness from 5nm to 33nm. Again, we propose that the film exhibiting higher cubic anisotropy is of better quality, as is shown by the quality of the FMR signal observed.
High frequency measurements gave a g-value of 2.03 for the films, lower than the bulk value of 2.12 [38], and the value of 2.14 observed by Atkas [9]. This is further supported by fits of the in-plane and out-of-plane angular dependencies of the resonance field to the theoretical model.

Chapter 5

FMR Characterisation of Post-Deposition Annealed Magnetite Films

5.1 Introduction

In this chapter, we will present the results of an FMR study of the effects of post-deposition annealing on 100nm thick films of magnetite deposited on both MgO and $MgAl_2O_4$ (MAO for short) substrates. These experiments follow and were inspired by those of Zhou et al who found that, remarkably, even a brief, 4 minute, anneal in air at a rather low temperature of 250°C gives an increase in the magnetisation, at 1T, of the film on MgO of 14% [19,20] and of that on $MgAl_2O_4$ of 10% [Zhou et. al., private communication]. The increase for the film on MgO was attributed to a change in antiferromagnetic coupling at the antiphase boundaries [19]. These magnetisation studies were carried out in TCD on samples prepared in Prof. Shvets' research group. The FMR measurements, reported here, were made on samples prepared by Yang Zhou in the same way in TCD.

The FMR study on these films was undertaken with the aim, firstly, of investigating to what extent this brief anneal also affects the magnetic anisotropy of the Fe_3O_4 film on (100) MgO. The second aim of the study is to compare the effect of annealing on the above films with that of annealing films of the same thickness deposited on $MgAl_2O_4$. Both Fe_3O_4 and $MgAl_2O_4$ have a similar spinel structure, but the lattice mismatch between the structures is 3.9%, much larger than the 0.34% between magnetite and MgO. In our case the film on $MgAl_2O_4$ is sufficiently thick (100nm)

for strain relaxation to occur through formation of dislocations, which would not be present in the fully strained system of 100nm Fe_3O_4 on MgO. However the films on MgO are expected to have many more antiphase boundaries than the films on $MgAl_2O_4$. The Fe_3O_4 film structure on $MgAl_2O_4$ is therefore expected to be very different to that of the films on MgO and the second aim of our experiments is to see if this is reflected in a difference in the annealing behaviour of the magnetic anisotropy.

In this chapter we present the effects of annealing on the magnetic anisotropy of 100nm Fe_3O_4 films grown epitaxially on both MgO(100) and $MgAl_2O_4$(100) substrates. The magnetic anisotropy was measured by FMR. Measurements of both the resonance field and the linewidth were made as a function of the direction of the magnetic field with respect to the film's crystal axes and from these we extract the anisotropy fields. Although details of the sample preparation and the experiments carried out on the films on MgO by Zhou et. al have been published previously [19,20] we will include here a brief summary. The equivalent measurements made by Zhou et.al. on the films on $MgAl_2O_4$ have not yet been published.

5.2 Experimental Details

5.2.1 Samples Investigated

Details of the procedure used to grow the 100nm Fe_3O_4 films on (100) MgO are given in Section 2.2.4, and also in [16,19] together with details of the X-ray diffractometer, Raman spectrometer and magnetometer characterisation. The same method of molecular beam epitaxy was used to grow the magnetite films on (100) $MgAl_2O_4$. The substrate temperature during growth was 250°C and, as for the films on MgO, subsequent annealing was carried out in air at 250°C.
Some Fe_3O_4 films on both MgO and $MgAl_2O_4$ were annealed in air at a temperature of 250°C both for a short time (4 or 5 minutes) and for a longer time (between 30 and 160 minutes).

Magnetisation

A remarkable change in the magnetisation behaviour of the Fe_3O_4/MgO films after annealing treatment was reported by Zhou et.al. [19,20], with results shown in fig-

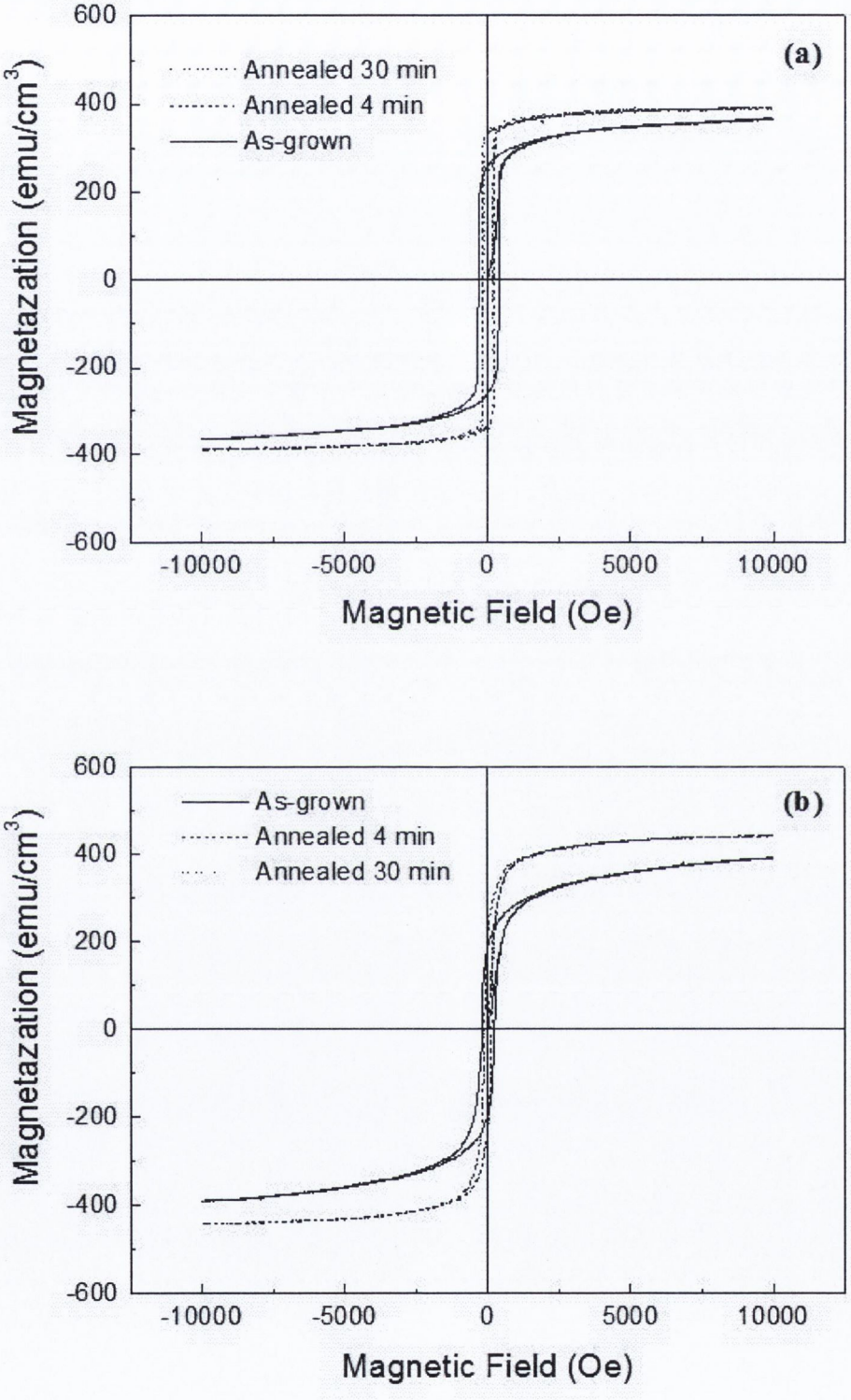

Figure 5.1: Hysteresis loops for as-grown and annealed 100nm thick Fe_3O_4 films on (a) $MgAl_2O_4$ and (b) MgO. In all cases the magnetic field is applied parallel to the plane of the film, along one of the principal axes.

ure 5.1(b). Even a short anneal in air (4 minutes at 250°C) produced an increase of 14% in the magnetisation of the film at 1T from 390 emu/cm^3 to 445 emu/cm^3, and caused the magnetisation to become more easily saturated. Extending the anneal to 160 min has little further effect.

Figure 5.1(a) shows the M-H loops recorded by Yang Zhou for a 100 nm $Fe_3O_4/MgAl_2O_4$ film. In all the cases the magnetic field lies within the film surface along [010]. From these measurements we see that magnetization of as-grown $Fe_3O_4/MgAl_2O_4$ films cannot be readily saturated with the maximum available field of 1 T, as is the case for the as-grown Fe_3O_4/MgO films. After short annealing (4 minutes) the films show an increase of 10% in magnetization at 1 T field, slightly less than the 14% increase for the case of Fe_3O_4/MgO, but the effect is still present and noteworthy nonetheless. The short anneal also induces a decrease in the slope of the M-H curves and causes the M(H) loop of $Fe_3O_4/MgAl_2O_4$ to become square-like. This suggests that the films on $MgAl_2O_4$ also become easier to saturate after the short anneal. Extending the anneal time to 30 min produces little further change.

In both cases, a decrease in the coercivity was observed (where by coercivity we mean the magnetic field required to reduce the magnetization to zero after it has been fully saturated). This can be seen in figures 5.1(a) and (b), where we observe that the hysteresis loops cross the M = 0 axis at a lower value of H for the annealed samples. The effect is slightly more pronounced for the $Fe_3O_4/MgAl_2O_4$ case, but is also present for the Fe_3O_4/MgO case.

Structure

Extensive characterisation of the films deposited on MgO was previously carried out by Zhou et. al. [19,20] High Resolution X-Ray Diffraction (HRXRD) measurements showed [19] that, both before and after annealing, the magnetite in-plane lattice constant is 0.84268nm, twice that of the MgO substrate. This indicates that the films remain in a fully strained state both before and after treatment. Resistivity and Raman Spectroscopy (RS) measurements [19] showed that in both the as grown and annealed films there were no traces of other iron oxide phases apart from magnetite.

Similar measurements were also conducted by Yang Zhou on the films on $MgAl_2O_4$ [unpublished]. Raman Spectroscopy measurements again showed magnetite to be the only iron oxide phase present both before and after annealing. Unlike the films on MgO that are fully strained, those on $MgAl_2O_4$ are largely relaxed. X-ray diffraction measurements show that the magnetite in-plane lattice parameter is 8.3666Å

for the 100nm as-grown film on $MgAl_2O_4$, and 8.3686Å for the same film after 30 minutes annealing. Since the lattice parameters for $MgAl_2O_4$ and bulk Fe_3O_4 are 8.0831Å and 8.3987Å respectively this shows that the in-plane strain of the as-grown film is already 90% relaxed, and is 94% relaxed after the 30 minute anneal. The out-of-plane lattice parameter is 8.4322Å for the as-grown film and 8.3922Å after the 30 minute anneal; the unit cell volume is therefore 590.2Å^3 and 587.7Å^3 respectively for these films and since both values are very close to that of 592.6Å^3 for bulk Fe_3O_4 any deviation from stoichiometry in the films is very small.

In summary, these measurements show that (1) all films investigated are composed of stoichiometric magnetite and contain no other iron oxide phases, (2) annealing the films does not significantly effect the stoichiometry of the films, and (3) the strain state of the films (fully strained for those on MgO and 90-94% unstrained for those on $MgAl_2O_4$) is not significantly affected by annealing.

5.2.2 FMR

The co-ordinate system we used to specify the directions of $\vec{M}$ and $\vec{H}$ is shown in Figure 5.2. For the FMR measurements the direction of the magnetic field, $\vec{H}$, was varied both within the (100) plane of the film (i.e. varying ϕ_H with constant $\theta_H = 90°$), and within the (001) plane (i.e. varying θ_H with constant $\phi_H = 0$).
All measurements were taken at room temperature on the X-band Bruker EPR spectrometer in Trinity College using a rectangular TE_{102} mode cavity operating at 9.6GHz. The sample was mounted flat on the end of a vertical, spin free, quartz rod that could be rotated by a goniometer, as described in Section 3.3.1. Samples were aligned as described in Section 3.3.1. The magnetic field position was calibrated using an NMR magnetometer and an EPR reference signal due to F^+ centers in MgO with a known g-value (2.0023).

5.3 FMR Results

5.3.1 FMR of Fe_3O_4 films deposited on (100) MgO

Figure 5.3 shows several spectra (recorded during the out of plane measurements) on the 100nm Fe_3O_4/MgO as grown film. The very sharp line at 3400 Oe is that of an F^+ center, used as a marker signal for field calibration as its g-value is precisely known. We will just note here that the FMR spectra observed are clear with high

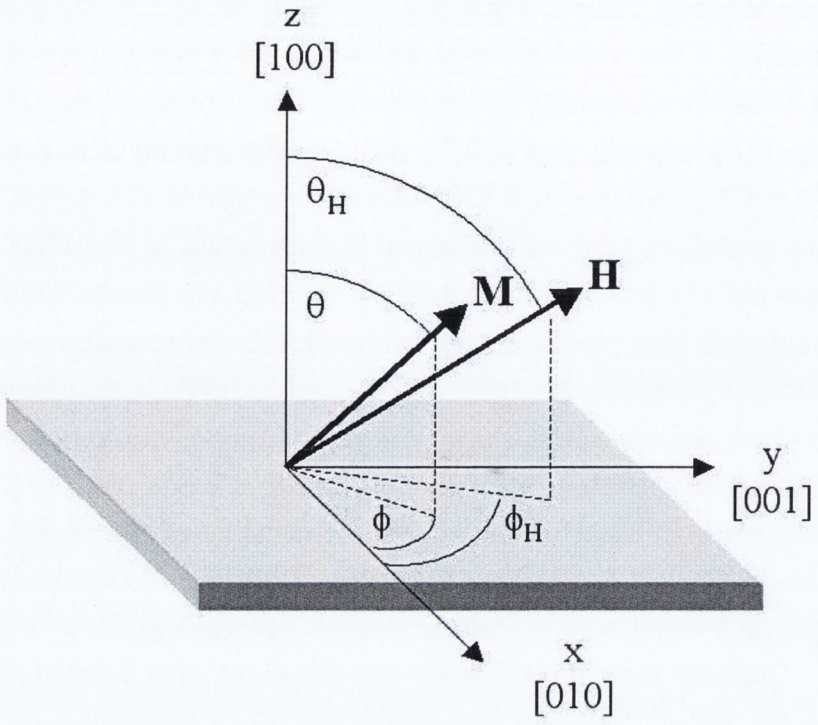

Figure 5.2: Coordinate system used for defining the orientation of $\vec{M}$ and $\vec{H}$ with respect to the film surface. The orientation of the applied magnetic field $\vec{H}$ is given by (ϕ_H, θ_H), while the resulting equilibrium orientation of the magnetisation is given by (ϕ, θ)

signal to noise ratio, and that this quality is representative of all of the spectra observed during this set of experiments.

We will first examine the in-plane angular dependence of the resonance field, H_R, for 100nm Fe_3O_4 on (100) MgO. The spectrum shown in figure 5.3 at $\theta_H = 90°$ is representative of the spectra observed - in each case only a single line was present. Figure 5.4(a) shows how the angular dependence of the resonance field is affected by the anneals. After only a 4 minute anneal the magnitude of the expected fourfold anisotropy is appreciably increased (as is evidenced by the greater difference between maximum and minimum values for H_R), but an additional 156 minutes gives little further change. We note that the occurrence of minima in H_R at ϕ_H = -45°, 45°, 135°,... that is along [011] type directions, is as expected for such films [9,12,13], and was also seen in our previous measurements (Section 4.5.1). The lines in Figure 5.4(a) are the fits obtained from the theory discussed in section 5.4, with parameter values as given in table 5.1.

As regards the peak-to-peak linewidth, ΔH_{PP}, Figure 5.4(b) shows that before an-

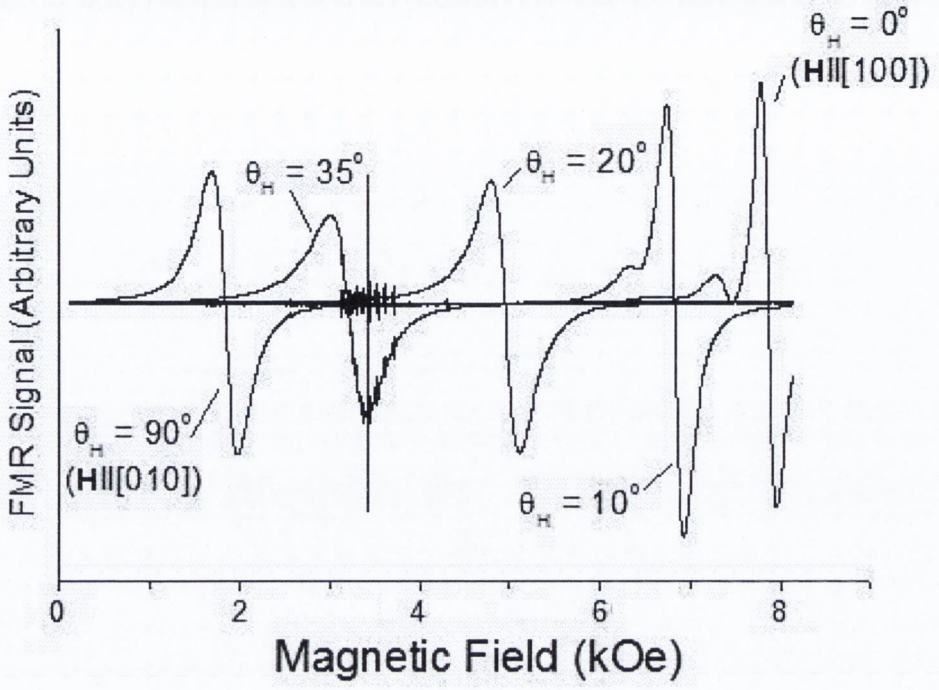

Figure 5.3: FMR spectra recorded at various orientations (marked θ_H) for the as-grown Fe_3O_4/MgO film. In each case $\phi_H = 0$.

nealing it varies by less than 20% as the field is rotated within the film plane. However, its mean value falls by 70 Oe from 280 Oe to 210 Oe after the 4 minute anneal but only by a further 30 Oe after the further 156 minutes. The form of the angular dependence also changes after the 4 minute anneal, but not thereafter. This reflects the change in anisotropy of H_R which also occurs primarily after the 4 minute anneal.

We now turn to the measurements taken after rotating the direction of $\vec{H}$ out of the plane of the film. Figure 5.3 shows several spectra recorded during the out of plane measurements on the 100nm Fe_3O_4/MgO as grown film. At most θ_H values only a single resonance line is observed but for $\theta_H \leq 15°$ a second much weaker line is also present; this may indicate some non-uniformity within the films (a similar phenomenon has been reported by Seshu Bai et. al. [70] for sputtered films of $Co_{100-x}Cu_x$). By contrast, for the annealed films on MgO only a single line is seen.

Figure 5.5 shows the out of plane angular dependence of H_R for the as grown and annealed films on MgO. In Figure 5.5(a) the data points are those for the stronger line. The plots shown in Figure 5.5(a), (b) and (c) are very similar as the angular variation of H_R is dominated by the shape anisotropy term. The solid lines show

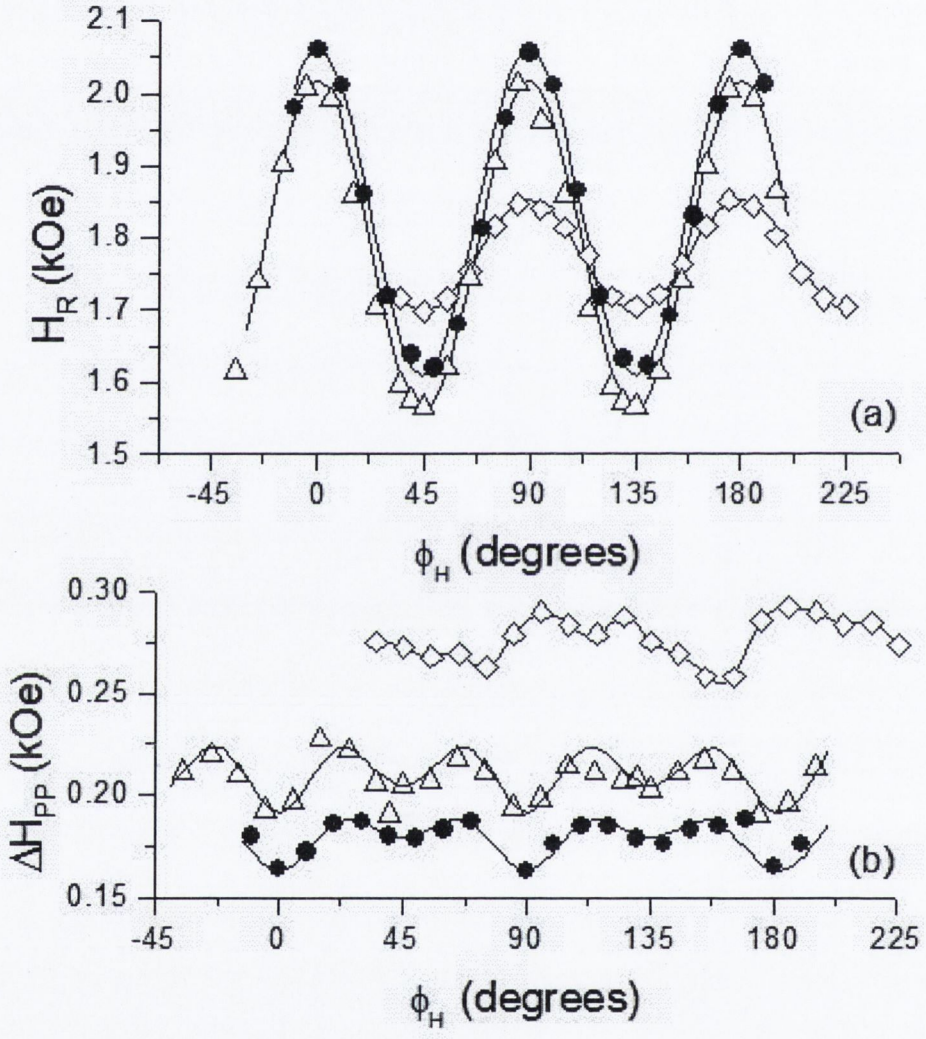

Figure 5.4: (a) In plane variation of the FMR line position for Fe_3O_4 on (100) MgO in the as-deposited state ($\diamond$) and after annealing for 4 minutes ($\triangle$) or 160 minutes ($\bullet$). The lines are theoretical fits as described in the text. (b) In plane variation of the FMR linewidth, ΔH_{PP}, for films on (100) MgO in the as-deposited state and after annealing; symbols are as before. The lines are guides to the eye.

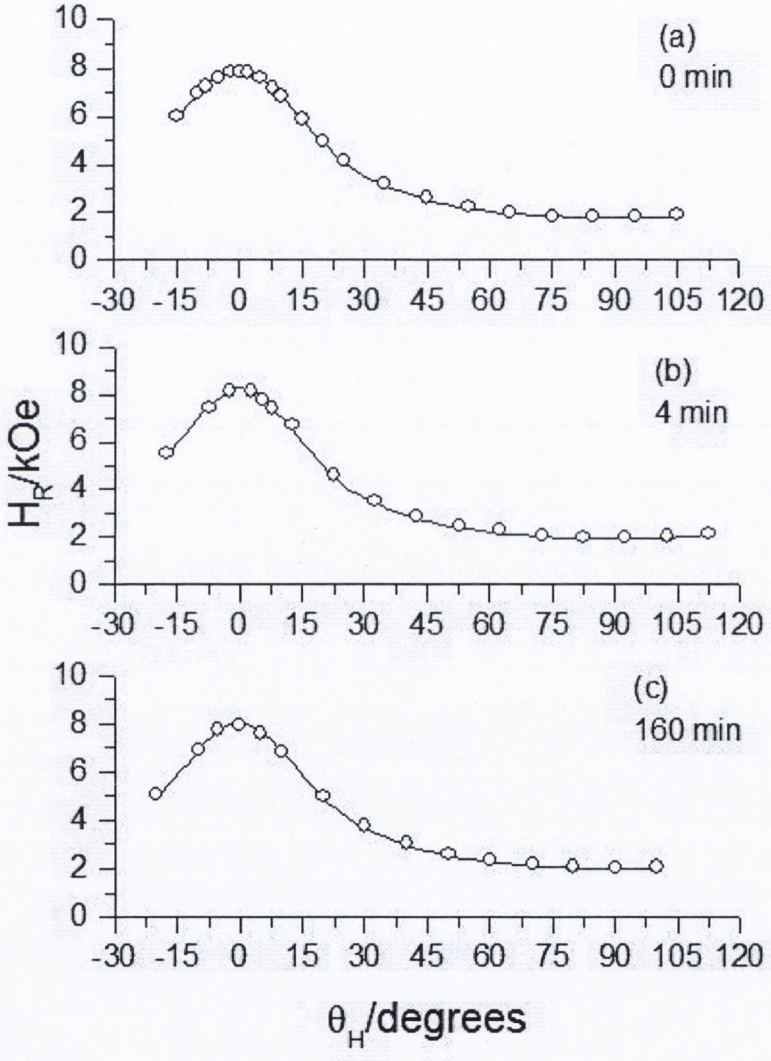

Figure 5.5: Out of plane variation of the FMR line position for Fe_3O_4 on (100) MgO in (a) the as-deposited state and after annealing for (b) 4 minutes and (c) 160 minutes. The lines are theoretical fits as described in the text.

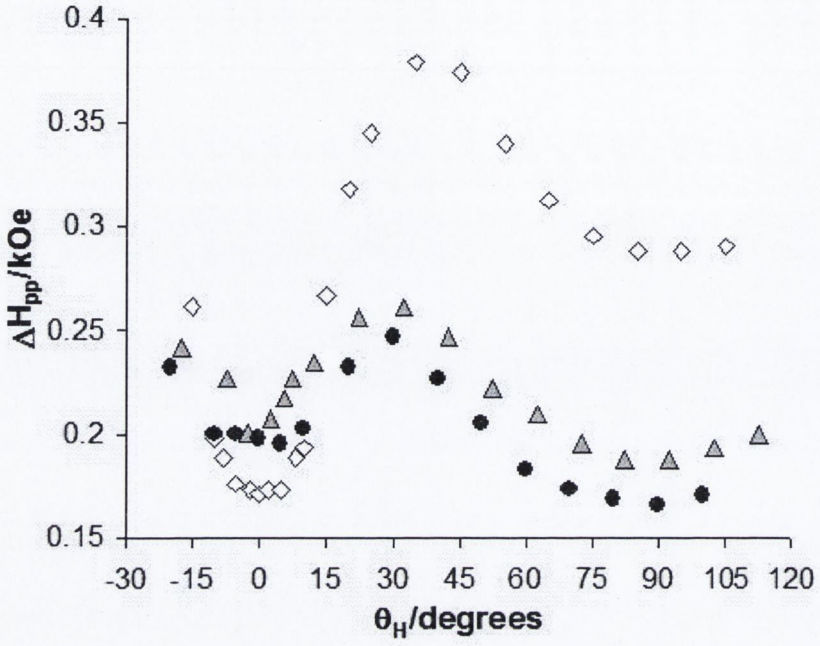

Figure 5.6: Out of plane variation of the FMR linewidth, ΔH_{PP}, for films on (100) MgO in the as-deposited state ($\diamond$) and after annealing for 4 minutes ($\triangle$) or 160 minutes ($\bullet$).

the excellent fits obtained from the theory, discussed in section 5.4, with parameter values given in Table 5.3. For the out of plane measurements the effects of the annealing are more evident in the angular variations of the peak-to-peak linewidth, ΔH_{PP}, which are shown in Figure 5.6. Although in each case ΔH_{PP} has minima at $\theta_H = 0°$ and 90°, with a maximum in the range $\theta_H = 30°$ - 40°, ΔH_{PP} is clearly affected by the annealing. Just a 4 minute anneal leads to a drop in ΔH_{PP}(max) from 370 Oe to 250 Oe and in $\Delta H_{PP}(\theta_H = 90°)$ from 290 Oe to 190 Oe. Increasing the annealing time to 160 minutes only leads to rather small further reductions in these widths. However at $\theta_H = 0°$ the linewidth is much less affected by the annealing and actually increases from 170 Oe to 200 Oe after annealing. It is also noticeable that the position of ΔH_{PP}(max) shifts from $\theta_H \approx 40°$ to $\theta_H \approx 30°$ after the 4 minute anneal, but no further after the longer anneal.

5.3.2 FMR of Fe_3O_4 films on (100) $MgAl_2O_4$

All the films on (100) $MgAl_2O_4$ give a single FMR line. Figure 5.7 (a) shows the in-plane angular dependence of H_R for the magnetite films deposited on (100) $MgAl_2O_4$, along with the corresponding fits of the theoretical model. Again we see the expected fourfold anisotropy but, in contrast to the films on (100) MgO, the minima occur at

$\phi_H = 0°$, 90°, 180°... that is for $\vec{H}$ in [001] type directions. There are several other differences between the FMR results for the films on MgO and $MgAl_2O_4$. Figure 5.7 (a) shows that a short anneal of 5 minutes has almost no effect on the cubic anisotropy although there is a decrease in the average value of H_R from 1.49 kOe to 1.37 kOe. However, after annealing for 160 minutes the cubic anisotropy increases almost to the value obtained for the similarly annealed film on (100) MgO. The 160 minute anneal also increases the average value of H_R. The lines in Figure 5.7 (a) show that good fits to the experimental data can be obtained with the theoretical model, as discussed in section 5.4.

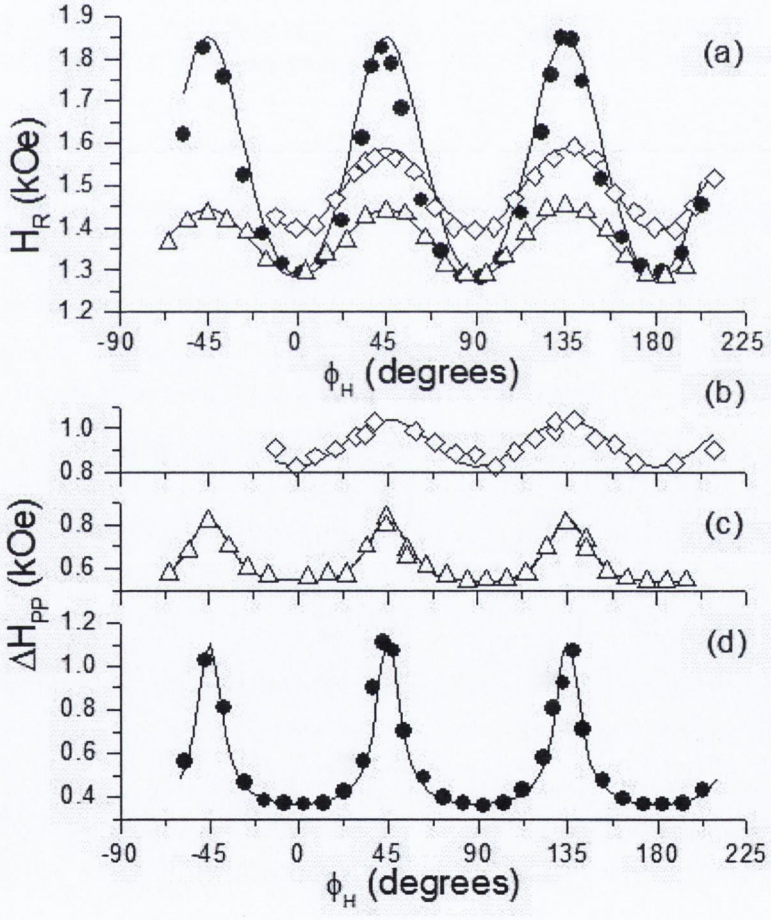

Figure 5.7: (a) In plane variation of the FMR line position for Fe_3O_4 on (100) $MgAl_2O_4$ in the as-deposited state ($\diamond$) and after annealing for 5 minutes ($\triangle$) or 160 minutes ($\bullet$). The lines are theoretical fits as described in the text. In plane variation of the FMR linewidth, ΔH_{PP}, for films on (100) $MgAl_2O_4$ in (b) the as-deposited state ($\diamond$) and after annealing for (c) 5 minutes ($\triangle$) or (d) 160 minutes ($\bullet$). The lines are guides to the eye.

The in-plane angular dependencies of ΔH_{PP} for the films on $MgAl_2O_4$ are shown in figures 5.7(b), (c) and (d). It is clear that not only does annealing affect the linewidth but, as comparison with the results in Fig 5.4(b) shows, so does the change in substrate. Figure 5.7(b) shows that for the as-grown film there is once again only a rather small (about 20%) angular variation in ΔH_{PP} but its average value of about 0.9 kOe is much higher than that of 0.28 kOe for the as grown film on MgO. Furthermore, the angular variation of ΔH_{PP} is now in step with that of H_R. Comparison of the results given in Figure 5.4 (b) and 5.7 (b), (c), (d) shows that, for the films on $MgAl_2O_4$, the additional 156 minutes of annealing produces a greater change in ΔH_{PP} than does the short anneal, an outcome opposite to that for the films on MgO. Finally we note that the 160 minute anneal of $Fe_3O_4/MgAl_2O_4$ (100) films leads to a considerable increase in the anisotropy of ΔH_{PP} as well as of H_R; however, taking the difference between the extreme values as a measure of this anisotropy, the ratio of the anisotropy of ΔH_{PP} to that of H_R only changes from 1.1 for the as grown film on $MgAl_2O_4$ to 1.3 after the 160 minute anneal.

Figure 5.8 shows the out of plane angular dependence of H_R for the as grown and annealed films. As for the films on (100) MgO the angular dependence is dominated by the shape anisotropy term. However a change is apparent after the 5 minute anneal: the value of H_R at $\theta_H = 0°$ has increased (to beyond the upper limit of our electromagnet) and so has $dH_R/d\theta_H$ in the region of $\theta_H \approx 15°$. Annealing for an additional 156 minutes has little effect. The solid lines show the fits obtained from the theory, discussed in section 5.4, with parameter values as given in table 5.4. The angular dependence of the out of plane linewidth ΔH_{PP} is shown in figure 5.9. As for the films on MgO, annealing has a much more obvious effect on ΔH_{PP} than on H_R. Once again annealing the film decreases ΔH_{PP} at $\theta_H = 90°$ although now the additional 156min of annealing does produce a further significant decrease. It is worth noting that at $\theta_H = 90°$ and for comparable anneal treatments ΔH_{PP} is considerably larger for the films on $MgAl_2O_4$ than for those on MgO. Also as before the maximum ΔH_{PP} shifts to smaller θ_H after annealing the films although in this case the value of $\Delta H_{PP}(\max)$ also increases. It is striking that at $\theta_H = 0$ the non-annealed film on $MgAl_2O_4$ has a resonance linewidth of 125 Oe that is less than the value of 170 Oe for the corresponding film on MgO. The data in Figure 5.9 suggest that at $\theta_H = 0°$ the annealed films have $\Delta H_{PP} \leq 125$ Oe.

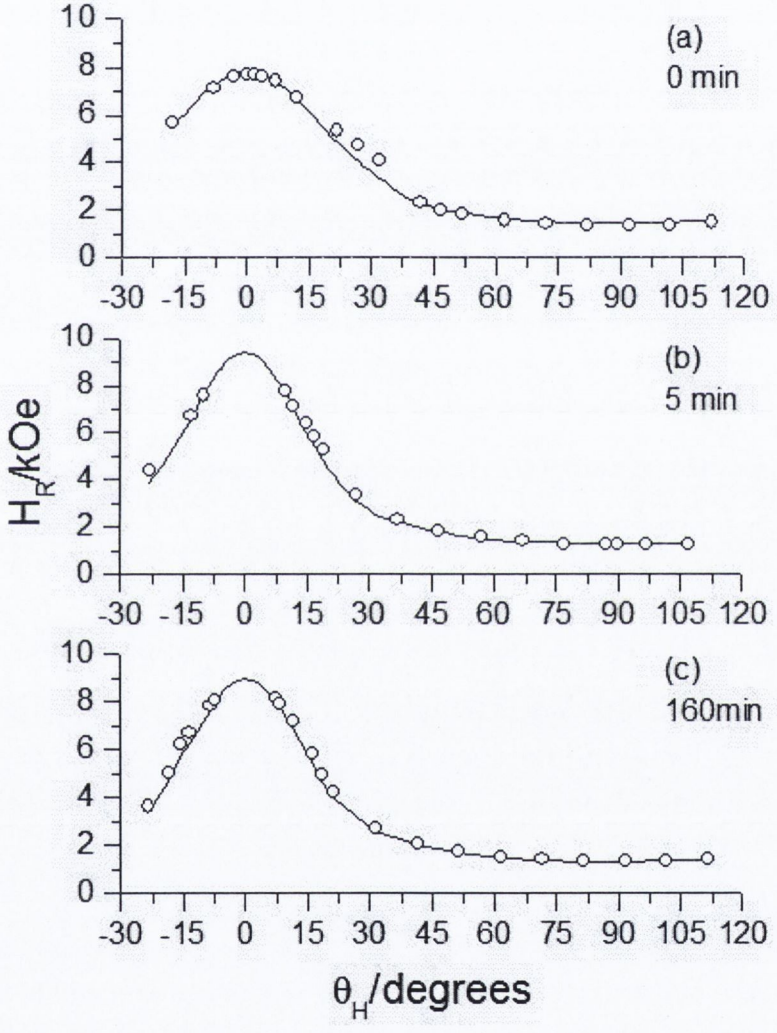

Figure 5.8: Out of plane variation of the FMR line position for Fe_3O_4 on (100) $MgAl_2O_4$ in (a) the as-deposited state and after annealing for (b) 5 minutes and (c) 160 minutes. The lines are theoretical fits as described in the text.

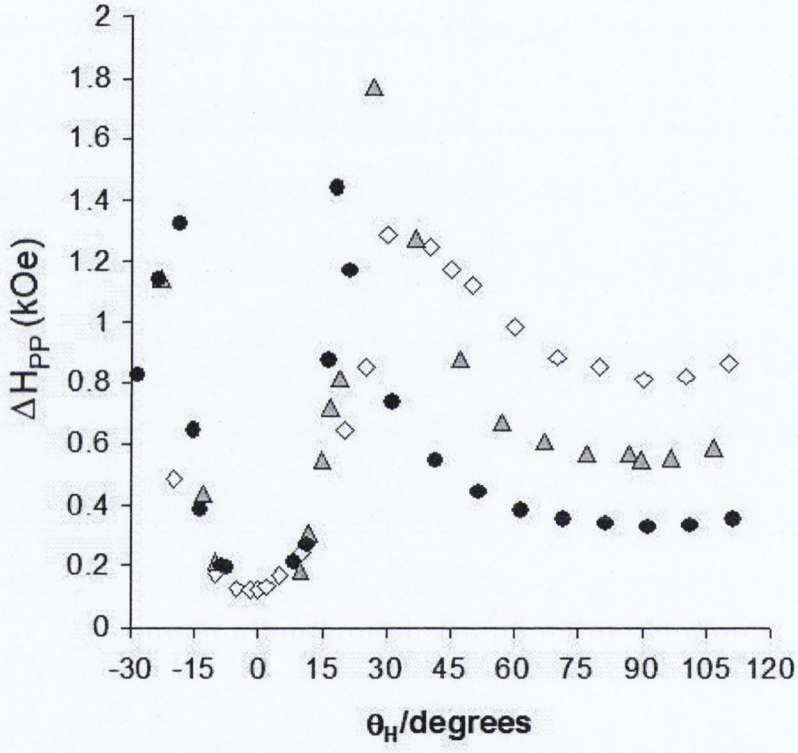

Figure 5.9: In plane variation of the FMR linewidth, ΔH_{PP}, for films on (100) $MgAl_2O_4$ in the as-deposited state ($\diamond$) and after annealing for 5 minutes ($\triangle$) or 160 minutes ($\bullet$)

5.4 Analysis

As described in Section 3.2.5 we begin with the appropriate expression for the magnetic free energy density of an epitaxial Fe_3O_4 film. Due to the lattice mismatch between magnetite and both the MgO and MAO substrates there may exist a slight tetragonal distortion. As shown in section 3.2.5, for such films the free energy density can be given by:

$$\begin{aligned} E &= \frac{1}{2}M[-2H\left(\cos\theta\cos\theta_H + \sin\theta\sin\theta_H\cos(\phi-\phi_H)\right) + 4\pi M\cos^2\theta \\ &\quad -H_{2\perp}\cos^2\theta - \frac{1}{2}H_{4\perp}\cos^4\theta - \frac{1}{2}H_{4||}\frac{1}{4}\left(3+\cos 4\phi\right)\sin^4\theta] \end{aligned} \tag{5.1}$$

with θ, θ_H, ϕ, ϕ_H as shown in figure 5.2, and $H_i = 2K_i/M$.

For a specific orientation of the applied field the equilibrium position of the magnetisation vector is given by minimising the free energy with respect to ϕ and θ; that is, we set $\partial E/\partial\phi$ and $\partial E/\partial\theta$ to zero. This implies that for the out of plane orientation, with $\vec{M}$, $\vec{H}$ lying within the (001) plane with $\phi = \phi_H = 0°$:

$$H\sin(\theta_H-\theta) - \cos\theta\sin\theta(4\pi M_{eff} + H_{4||}\sin^2\theta - H_{4\perp}\cos^2\theta) = 0 \tag{5.2}$$

where $4\pi M_{eff} = 4\pi M - H_{2\perp}$. For the in plane orientation ($\theta = \theta_H = 90°$):

$$H\sin(\phi-\phi_H) + 0.25H_{4||}\sin 4\phi = 0 \tag{5.3}$$

The resonance condition can be derived using equation 3.10

$$\left(\frac{\omega}{\gamma}\right)^2 = \left(\frac{1}{M\sin^2\theta_M}\frac{\partial^2 E}{\partial\theta_M^2}\right)\times\left(\frac{1}{M}\frac{\partial^2 E}{\partial\phi_M^2}\right) - \left(\frac{1}{M\sin\theta_M}\frac{\partial^2 E}{\partial\theta_M\partial\phi_M}\right)^2 \tag{5.4}$$

yielding the following resonance conditions for the in-plane case:

$$\begin{aligned} \left(\frac{\omega}{\gamma}\right)^2 &= \left(H\cos(\phi-\phi_H) + 4\pi M_{eff} + H_{4||}\frac{3+\cos 4\phi}{4}\right) \\ &\quad \times\left(H\cos(\phi-\phi_H) + H_{4||}\cos 4\phi\right) \end{aligned}$$

(5.5)

and out of plane case (but within the (001) plane):

$$\left(\frac{\omega}{\gamma}\right)^2 = \left(H\cos(\theta-\theta_H) - \left[4\pi M_{eff} - \frac{H_{4\perp}}{2} + \frac{H_{4||}}{2}\right]\cos 2\theta + \left[H_{4\perp}+H_{4||}\right]\frac{\cos 4\theta}{2}\right) \times \left(H\cos(\theta-\theta_H) - \left(4\pi M_{eff}+2H_{4||}\right)\cos^2\theta + \left(H_{4||}+H_{4\perp}\right)\cos^4\theta + H_{4||}\right)$$

(5.6)

5.4.1 In plane Angular Dependence

In equation 5.5, if $\phi \neq \phi_H$, the plot of the resonance field vs ϕ_H exhibits a smaller curvature at $\vec{H}$ parallel to the hard axis than $\vec{H}$ parallel to the easy axis [71,72], but as figures 5.4 and 5.7 show, except for the 160min annealed film on $MgAl_2O_4$, any such difference is negligible. Equation 5.3 also implies that $\phi \approx \phi_H$ when H >> $H_{4||}$ and from the values of $H_{4||}$ in tables 5.1 and 5.2 this is clearly the case. Therefore we take $\phi = \phi_H$ for all cases except the 160min annealed film on $MgAl_2O_4$, for which we use equation 5.3 to calculate $\phi - \phi_H$. Figures 5.4 and 5.7 show that the angular variation of H_R for the films on both substrates can be well fitted by equation 5.5 taking g = 2.12 [38], and values for $H_{4||} = 2K_{4||}/M$ and $4\pi M_{eff}$ given in tables 5.1 and 5.2. It is likely that just as good fits could be obtained with g = 2.03 but with slightly different values for $4\pi M_{eff}$.

Table 5.1: The parameter values for Fe_3O_4 on (100) MgO. $H_{4||}$ and $4\pi M_{eff}$ are evaluated from the fits to the in plane angular dependence of H_R

Anneal Time	M (emu/cm^3)	4πM (kOe)	$H_{4\|\|}$ (Oe)	$K_{4\|\|}$ (kJ/m^3)	$4\pi M_{eff}$ (kOe)	$H_{2\perp}$ (Oe)	$K_{2\perp}$ (kJ/m^3)
0 min	316 ± 4	3.97 ± 0.05	-93 ± 3	-1.5 ± 0.1	4.20 ± 0.01	-230 ± 60	-4 ± 1
4 min	368 ± 4	4.62 ± 0.05	-278 ± 3	-5.1 ± 0.1	4.29 ± 0.01	330 ± 80	6 ± 1
160 min	372 ± 4	4.67 ± 0.05	-277 ± 3	-5.2 ± 0.1	4.09 ± 0.01	580 ± 80	11 ± 1

Since, as shown by figure 5.1, the magnetization varies with field in the range covered by that of H_R the values of M given in tables 5.1 and 5.2 are those of its mean value with its uncertainty reflecting the range of M.

As shown in table 5.1, for the films on (100) MgO the cubic anisotropy term $K_{4||}$ is negative and it increases considerably in magnitude after only the 4 minute anneal but shows no further increase for the extra 156 minutes annealing. The negative

Table 5.2: The parameter values for Fe_3O_4 on (100) $MgAl_2O_4$. $H_{4||}$ and $4\pi M_{eff}$ are evaluated from the fits to the in plane angular dependence of H_R

Anneal Time	M (emu/cm^3)	4πM (kOe)	$H_{4\|\|}$ (Oe)	$K_{4\|\|}$ (kJ/m^3)	$4\pi M_{eff}$ (kOe)	$H_{2\perp}$ (Oe)	$K_{2\perp}$ (kJ/m^3)
0 min	309 ± 4	3.88 ± 0.05	112 ± 4	1.7 ± 0.1	5.45 ± 0.02	-1570 ± 70	-24 ± 1
5 min	364 ± 4	4.57 ± 0.05	91 ± 3	1.7 ± 0.1	6.26 ± 0.01	-1690 ±60	-31 ± 2
160 min	370 ± 4	4.65 ± 0.05	330 ± 8	6.1 ± 0.2	4.87 ± 0.04	-220 ± 90	-4 ± 2

sign gives the easy axis along [110] type directions as previously observed for such films [9,12,13], and as we observed in our previous measurements (Section 4.5.1). The value of $2K_{4||}/M$ of -277 Oe is less than those of -380 Oe [13] and -440 Oe [65] previously reported for MBE grown films on (100) MgO and also of -466 Oe for bulk Fe_3O_4 [38] but a value of only -22 Oe was reported [9] for a sputtered film and the anisotropy was found to disappear at a film thickness of 60nm for one deposited by a pulsed laser [12].

Table 5.1 also shows that the shape anisotropy term (4πM) is the dominant contribution to $4\pi M_{eff}$ and so the latter is little affected by annealing the film. The value of about 4 kOe for $4\pi M_{eff}$ lies within the range 2.5 kOe to 7 kOe of previously reported values [9,12,13]. Since the value for $2K_{2\perp}/M$ is the difference of two large and nearly equal quantities its error is large but, within error, there is a shift to more positive values after annealing with a sign change after the 4 minute anneal.

In contrast to the films on MgO those on $MgAl_2O_4$ have a positive $K_{4||}$ (as shown in Table 5.2) corresponding to the in plane easy axis being along [010] type directions. This was also observed for the untreated films discussed in Section 4.5.1; the reason for this change is not known. Also in contrast to the films on MgO there is no change within error of $K_{4||}$ after the short anneal but after the long anneal it has increased to 6.1 kJm^{-3}, a value exceeding 5.2 kJm^{-3} for the film on MgO. Previous [12] FMR measurements of Fe_3O_4 films deposited on $MgAl_2O_4$ using a pulsed laser found the in plane difference $\Delta H_R = H_{100} - H_{110}$ to be 500 Oe for a film thickness in the range 100nm to 200nm and this is close to our value of 560 Oe after the 160 minute anneal; however they found the easy axis to be [110] as for the films on MgO. It is not clear why for our films the easy axis is along [010] type directions.

The values of $4\pi M_{eff}$ for the non-annealed and short annealed films on $MgAl_2O_4$ are significantly larger than the corresponding values for the films on MgO and this is reflected in the larger values of $2K_{2\perp}/M$. This is to be expected because of the greater lattice mismatch with the $MgAl_2O_4$ substrate and Kale et. al [12] have shown that a value of about 1kOe for $2K_{2\perp}/M$ is reasonable for strained Fe_3O_4 on $MgAl_2O_4$.

It is not clear what is the reason for the considerable drop in the value of $2K_{2\perp}/M$ after the 160min anneal of the film on $MgAl_2O_4$.

5.4.2 Out of plane

The good fits to the out of plane angular dependence of H_R, shown in figures 5.5 and 5.8, are obtained using equations 5.5 and 5.6 with the values of the parameters given in tables 5.3 and 5.4 together with g = 2.12 [38].

Table 5.3: The parameter values for Fe_3O_4 on (100) MgO. Values for $H_{4||}$ are as in table 5.1, and taking $H_{4\perp} = H_{4||}$ gave a good fit in each case. $H_{2\perp}$ and $4\pi M_{eff}$ are evaluated from the fits to the out of plane angular dependence of H_R

Anneal Time	M (emu/cm^3)	4πM (kOe)	$H_{4\|\|} = H_{4\perp}$ (Oe)	$4\pi M_{eff}$ (kOe)	$H_{2\perp}$ (Oe)	$K_{2\perp}$ (kJ/m^3)
0 min	342 ± 38	4.3 ± 0.5	-93 ± 3	4.53 ± 0.05	-230 ± 500	-4 ± 9
4 min	421 ± 19	5.3 ± 0.2	-278 ± 3	4.71 ± 0.05	600 ± 300	13 ± 7
160 min	422 ± 17	5.3 ± 0.2	-277 ± 3	4.47 ± 0.05	800 ± 300	17 ± 7

Table 5.4: The parameter values for Fe_3O_4 on (100) $MgAl_2O_4$. Values for $H_{4||}$ are as in table 5.2; $H_{4\perp}$, $H_{2\perp}$ and $4\pi M_{eff}$ are evaluated from the fits to the out of plane angular dependence of H_R

Anneal Time	M (emu/cm^3)	4πM (kOe)	$H_{4\|\|}$ (Oe)	$H_{4\perp}$ (Oe)	$4\pi M_{eff}$ (kOe)	$H_{2\perp}$ (Oe)	$K_{2\perp}$ (kJ/m^3)
0 min	334 ± 25	4.2 ± 0.3	112 ± 4	400 ± 200	4.8 ± 0.1	-600 ± 400	-10 ± 8
4 min	376 ± 14	4.7 ± 0.2	91 ± 3	100 ± 300	6.3 ± 0.1	-1600 ± 300	-30 ± 7
160 min	377 ± 13	4.7 ± 0.2	330 ± 8	-400 ± 300	5.6 ± 0.1	-900 ± 300	-17 ± 6

The values of M given in these tables are its average over the relevant field range; this range is both larger and extends to higher fields compared to the in-plane rotation and hence both the average values of M and their uncertainty are greater than before. The values of $4\pi M_{eff}$ given in tables 5.3 and 5.4 show that the shape anisotropy term is dominant and therefore the effect of annealing the sample manifests itself primarily through a change in this term brought about by the change in M as indicated in figure 5.1. The values of $K_{2\perp}$ have a much greater uncertainty, due to the larger uncertainty in M, compared to those obtained from in plane measurements but they are in reasonable agreement with the latter values. As regards the values of $H_{4||}$ and $H_{4\perp}$, for the films on (100) MgO the best fits are obtained with $H_{4||} = H_{4\perp}$ and the same $H_{4||}$ as for the in-plane angular dependence. However, for the films on (100) $MgAl_2O_4$ the fits are improved by choosing $H_{4||} \neq H_{4\perp}$ as indicated in table 5.4; this

presumably arises from the greater tetragonal distortion associated with the greater lattice mismatch for the films on $MgAl_2O_4$.

5.4.3 Angular Dependence of the Linewidth

In order to analyse the angular dependencies exhibited by the FMR peak-to-peak linewidth, ΔH_{PP}, we refer to the standard form expressing the linewidth contributions:

$$\Delta H_{PP} = \Delta H_{hom} + \Delta H_{inhom} \tag{5.7}$$

where the homogeneous contribution, ΔH_{hom}, arises from the intrinsic damping of the magnetisation and ΔH_{inhom} comes from the magnetic inhomogeneities of the sample; both can have an angular dependence. The homogeneous contribution is given by [59,61]:

$$\Delta H_{hom} = \frac{1}{\sqrt{3}} \frac{1}{|\partial\omega/\partial H|} \frac{G}{M^2} \left(\frac{\partial^2 E}{\partial\theta^2} + \frac{1}{\sin^2\theta} \frac{\partial^2 E}{\partial\phi^2} \right) \tag{5.8}$$

Here G is the Gilbert damping parameter. For the in-plane case, this reduces to an expression proportional to $1/\mathrm{Cos}(\phi - \phi_H)$. Since $\phi \approx \phi_H$, this simply gives a contribution independent of angle. For the out of plane orientation, equation 5.8 reduces to an expression proportional to $1/\mathrm{Cos}(\theta - \theta_H)$, where θ is calculated using equation 5.2 for each orientation θ_H.

The inhomogeneous contribution may also have an angular dependence. Magnetic inhomogeneities, arising from sample imperfections such as mosaic structure and defects, can give rise to a distribution in both the directions of the crystal and magnetic anisotropy axes as well as a spread in the magnitudes of the internal fields so that, following Chappert et al [62], we may write

$$\Delta H_{inhom} = \frac{\partial H_R}{\partial \phi, \theta} \Delta\phi, \theta + \sum_j \Delta H_j \tag{5.9}$$

This takes account of possible linewidth contributions arising from an angular spread in the crystalline axes ($\Delta\phi$,θ), and in the internal anisotropy fields (ΔH_j includes contributions from $H_{4||}$, $H_{4\perp}$ and $H_{2\perp}$).

For the in plane case, using equation 5.5 and taking partial derivatives of H_R with respect to ϕ_H, $H_{4||}$ and $H_{2\perp}$, we can establish the angular dependence of each possible contribution. We find that a spread in the cubic axis direction (ϕ_H) would give regular minima at (0°, 45°, 90°...) a spread in the magnitude of $H_{4||}$ would give maxima at (0°, 45°, 90°...) and a spread in the magnitude of $H_{2\perp}$ would give

minima at (0°, 90°, 180°...) for $H_{4||}$ <0, or at (45°, 135°, 225°...) for $H_{4||}$ >0. Using the same procedure with equation 5.6, we can establish the angular dependencies for the out of plane orientation. In this case, a spread in the magnitude of any of the anisotropy fields $H_{4||}$, $H_{4\perp}$ and $H_{2\perp}$ give maxima at $\phi_H = 0°$ and 90°, with minima in between. A spread in the cubic axis direction ($\Delta\theta_H$) gives minima at $\theta_H = 0°$ and 90° with a maximum in the range θ_H = 15°-18°.

We will now consider the angular dependence of the linewidth of the films on MgO firstly within the plane of the films as shown in Figure 5.4. Here the angular dependence is small and the most striking change after annealing is the decrease in the average linewidth, by 25% (80 Oe) after 4 minutes annealing, but only a further 11% (30 Oe) after 160 minutes annealing. Such a change could be brought about by a decrease in the homogeneous component arising from a drop in the damping term G. This supports the proposal [19,20] that the annealing treatment significantly reduces the exchange frustration across the antiphase boundaries, since a reduction in the frustration in these regions would lead to a decrease in energy dissipated and hence reduce the damping. The small angular variation suggests that the inhomogeneous contribution to the linewidth is small.

We now consider the out-of-plane angular dependence of the linewidth shown in Figure 5.6. For all samples ΔH_{PP} has a maximum value in the range θ_H = 30°-40°. A similar angular dependence has been reported previously [70] for sputtered $Co_{100-x}Cu_x$ films and [73] for Co/Mn superlattice, and in both cases was attributed to a spread in the cubic axis $\Delta\theta_H$. However, calculating this contribution for our samples using equations 5.6 and 5.9 gives a maximum in the range θ_H = 15°-18°, which does not agree with what is observed. Using these equations we also find that any angular dependence arising from a spread in the anisotropy fields would show a minimum rather than a maximum linewidth between parallel and perpendicular orientations and as such can also be ruled out.

The intrinsic linewidth (calculated using equation 5.8) does exhibit a maximum at approximately the same orientation as is observed experimentally (to within 5°), suggesting that this may at least partly account for the angular dependence of ΔH_{PP}. However, there are several reasons why this cannot be the only factor. The first is that the ratio of ΔH_{PP}(Max) to ΔH_{PP}(Min) observed experimentally is in each case significantly higher than that of the intrinsic linewidth contribution. The calculated ratio for the intrinsic contribution is between 1.2 and 1.3, whereas that observed experimentally for the films on MgO ranges from 1.4 to 2.2, and for the films on $MgAl_2O_4$ ranges from 7.4 to 10.3. Secondly, the intrinsic linewidth gives two equal minima at $\theta_H = 0°$ and 90°. This is approximately the case after both

anneals but not before any anneal. In the case of the as-deposited film the greater value of ΔH_{PP} at $\theta_H = 90°$ than at $\theta_H = 0°$ may arise from two-magnon scattering as this is only operative operative when the magnetisation is in plane [74].

We now consider the linewidth angular dependence for the films on $MgAl_2O_4$, as shown in figures 5.7 and 5.9. The magnitudes of ΔH_{PP} are much higher than those observed for the films on MgO and this is to be expected due to the larger lattice mismatch between Fe_3O_4 and the $MgAl_2O_4$ substrate than between it and the MgO substrate. This larger lattice mismatch would lead to a larger number of strain-relaxation type defects in the film on $MgAl_2O_4$ (such as misfit dislocations) and hence a larger linewidth.

Looking at the in-plane case, the most obvious effect of the annealing treatment is the increase in the amplitude of variation in ΔH_{PP} but this is solely due to a decrease in the minimum linewidth and hence, as for the films on MgO, annealing does decrease the average linewidth, possibly due to a drop in G, the Gilbert damping parameter.

The in-plane angular variations of ΔH_{PP} for both the pre- and post-anneal films show minima at $\phi_H = 0°$, $90°$... and maxima at $\phi_H = 45°$, $135°$... which are at the same orientations as the minima and maxima observed for H_R. This is similar to behaviour seen before for Fe_4/V_4 superlattices [61]. In that case, the behaviour was attributed to a spread in the crystal axis directions ($\Delta\phi_H$). However, examining the form of this contribution in our case we find that the angular dependence does not match our results because, as mentioned earlier, this would give rise to minima at $\phi_H = 0°$, $45°$, $90°$...

We cannot account for the observed angular dependence because it is too large to be due to the homogeneous term and does not match that expected for any contribution from inhomogeneities.

Finally we consider the out-of-plane angular dependence of ΔH_{PP} for the films on $MgAl_2O_4$. This is similar to that for the films on MgO but the linewidths are generally larger, as was the case for the in-plane measurements. The greater value of ΔH_{PP} at $\theta_H = 90°$ than at $0°$ for the as-deposited film may, as suggested earlier, come from two-magnon scattering. The reduction in ΔH_{PP} at $\theta_H = 90°$ as annealing proceeds may reflect a reduction in this scattering caused by the improved quality of the film. It is noticeable that the linewidth maximum occurs close to the θ_H value for maximum slope of the H_R versus θ_H plots and so may be associated with a spread in the crystal axis direction θ_H which would give a linewidth maximum close to this position.

5.4.4 Discussion

Finally we briefly discuss possible explanations for the observed changes in the magnetic anisotropy and for the differences between the behaviour of the films on MgO and $MgAl_2O_4$.

One possible explanation for the changes seen in the films' magnetic anisotropy is that the defects within the films are being altered by the annealing process. The dominant defect within the films on MgO is the antiphase boundary (APB), and it is due to the presence of these defects that a number of the differences between magnetite films and the bulk material have been attributed (e.g. difficulty in saturating the magnetisation, changes in magnetoresistance [16,23,43,44]). It has been proposed [19,20] that the increase in the value of the magnetisation after annealing comes from the decay of the antiferromagnetic and frustrated exchange interaction that takes place through localised thermo-chemical reaction at the APBs or in their vicinity. It has also been suggested by Erenstein et. al. [42] that antiphase domain boundaries in Fe_3O_4 films anneal out via diffusive mechanism at relatively low temperatures (250-350°C). It is possible that reducing the frustrated exchange across the APBs also increases the magnetic anisotropy of the Fe_3O_4 films; this would explain the observed increase in $K_{4||}$ after annealing.

In contrast to this, while the films on $MgAl_2O_4$ will also have some APBs, the number will be much fewer since the film and substrate unit cells are much closer to a 1:1 match. The films will, however, possess a large number of misfit dislocations. Thus, while it may be possible to alter the APB defects with a short anneal, it should take more energy to alter the misfit dislocation, as this would involve actual movement of atoms. This would fit with the observation that the increase in magnetic anisotropy is only seen after a longer anneal for the films on $MgAl_2O_4$ than of those deposited on MgO.

5.5 Conclusions

Fe_3O_4 films deposited on MgO show an increase in cubic anisotropy after even a brief period of annealing (4min at 250°C in air), with the cubic anisotropy parameter $K_{4||}$ increasing from -1.5 kJ/m^3 to -5.1 kJ/m^3. The linewidth simultaneously decreases, with the mean (in-plane) value decreasing from 280 Oe to 210 Oe after the 4min anneal. However, annealing for a further 160min shows no further change

in $K_{4||}$ and only a small further change in the mean in-plane linewidth, to 180 Oe. This mirrors the changes in magnetisation measured by Zhou et.al [19,20].

However, unlike the behaviour of the magnetisation with annealing for the films on $MgAl_2O_4$ (which increases by 10% after 4 minutes annealing and no further with extended annealing time), $K_{4||}$ remains unchanged after 5 min annealing but increases from 1.7 kJ/m^3 to 6.1 kJ/m^3 after 160min. Similarly, the in-plane linewidth shows only a small change after 5 min annealing, but decreases significantly after 160 minutes of annealing.

These results support the suggestion by Yang et.al [19,20] that the APB structure in the films on MgO can be significantly altered by even a rather gentle air anneal. Our results suggest that more extensive annealing is required to improve the quality of films on $MgAl_2O_4$.

Chapter 6

FMR Characterisation of Magnetite on Vicinal MgO (100) Substrates

6.1 Introduction

In this chapter, we present the results of a study of magnetite films deposited on vicinal (or stepped) substrates. The aims of the study are to explore how the symmetry-breaking of the stepped surface is manifest in the magnetic anisotropy of the film, and to explore the effect on this of changing film thickness and miscut angle. We do this by examining the in-plane angular dependencies of resonance field, H_R, and peak-to-peak linewidth, ΔH_{PP}, for films of varying thickness, and varying substrate miscut angle.

We performed FMR measurements at 9.6 GHz on films of magnetite deposited by MBE on substrates of MgO miscut from the (100) direction. We have examined the effect of changing both the vicinal angle in the range 2° to 10° for a fixed film thickness of 45nm and of changing the film thickness from 30 nm to 70 nm at a fixed vicinal angle of 2°.

We found that the in-plane fourfold anisotropy constant $K_{4||}$ is approximately the same for all films but the dominant in-plane uniaxial constant $K_{2||}$ varies linearly with the inverse of the film thickness and approximately quadratically with the vicinal angle. A second, weaker, in-plane uniaxial term is evident for the film on a larger miscut (10°) substrate. The easy axis of the dominant in-plane uniaxial term is perpendicular to the step edges. The dominant in-plane uniaxial anisotropy has one term inversely proportional to the film thickness that is associated with anisotropy

localized at the interface and a second term that is independent of film thickness; the latter may arise from the preferential alignment of antiphase boundaries with the step edges.

The chapter is laid out as follows: first, we will provide a short introduction describing the nature of the vicinal substrates, how the step edges influence the formation of antiphase boundaries, and outlining the properties of similar films which have been extracted in previous studies. We then outline the experimental details, giving specifics on the samples investigated, and experiments conducted. We will then present the experimental data, and finally outline the analysis, present the extracted results, and provide a detailed discussion of same.

6.2 Magnetite on Vicinal Substrates

The magnetic properties of ferromagnetic thin films grown epitaxially on a vicinal substrate surface are of interest because of both their technological and scientific importance [75–77]. There have been several studies of such films on these step arrays: Fe/stepped Ag(100), [78–80], Fe/stepped Au(100) [80], Fe/stepped W(001) [81,82], Fe/stepped W(110) [25], Fe/stepped Mo(110) [83], $Fe_{1-x}Co_x$/stepped GaAs(100) [84], Co/stepped Cu(100) [79,85], $CoPt_3$/stepped MgO(100) [86]. They all show that the parallel step arrays induce an in-plane uniaxial magnetic anisotropy. However the easy axis of magnetisation associated with this anisotropy is sometimes parallel to the step edges [77,79], [83], [85] and at other times perpendicular to them [80–82,86]. As noted above, measurements have so far been mostly confined to films of Fe or Co and there are no reports or similar investigations for half metallic ferromagnetic materials.

Magnetite, as a half metallic ferromagnetic (HMFM), has desirable properties for use in spin electronics. However, films on MgO contain antiphase boundaries (APBs) (as described in Section 2.2.3). To selectively extract the contribution of APBs to the films' magnetoresistance (MR) Arora et al [16] measured the MR in directions parallel to and perpendicular to the step edges formed by the epitaxial growth of Fe_3O_4 films on vicinal (100) MgO substrates with miscut angles of 0.5° and 2°. They showed that the APBs would preferentially align parallel to the step edges and so were able to show that the observed anisotropy in MR could be attributed to presence of the APBs.

The term "vicinal" in crystallography is defined as "denoting a plane the position of which varies very little from that of a fundamental plane of the form" - i.e. the material surface is mis-cut by a small angle with respect to a low-index plane. Figure 6.1 illustrates a high-miscut surface of MgO. The surface consists of plateaus of the low-index planes separated by atomic-height steps.

Figure 6.1: High-miscut surface of MgO (miscut angle 11.3°) shown to the atomic scale. Red and grey spheres represent O and Mg atoms respectively. We note the presence of plateaus of the low-index surface, separated by atomic height steps.

As was described in Section 2.2.3, MBE deposited Fe_3O_4 forms by nucleation of islands, leading to the likely formation of APBs. In this case of deposition on a stepped surface, the islands of Fe_3O_4 forming on different atomic terraces nucleate independently from each other. Consequently, as the nucleation islands grow there is a significant chance that antiphase boundaries are formed along the step edges of the atomic terraces. The problem was investigated thoroughly by Arora, Sofin, and Shvets [16] during previous characterisation of MBE deposited Fe_3O_4 films on vicinal MgO, and it was calculated that there was at least a 75% chance of APB formation at the step edges. Thus investigating films deposited on a stepped surface provides a unique way to increase the density of APBs of a particular orientation. As the density of the APBs aligned along the step edges is greater than in the perpendicular direction, we would expect the films to exhibit different properties for the different directions, and can so identify the magnetic effects of an increased APB density.
In previous studies of Fe_3O_4 [16,43] it was found that specimens deposited on high-vicinal substrates showed reduced magnetic moment as compared with the films grown on low-vicinal substrates, agreeing with the expected reduction in magnetic moment due to an increase in APB density. Magnetoresistance was also found to be significantly higher for films on high-vicinal substrate than for those on low-vicinal substrate. A strong anisotropy in the MR was observed, which correlated with the

direction of atomic step edges. The observed modification in the magnetotransport behavior was attributed to an enhanced spin scattering arising due to the presence of a greater density of APBs.

6.3 Experimental Details

6.3.1 Samples Investigated

Figure 6.2 shows a schematic diagram of the vicinal MgO (100) substrate. We define α as the miscut angle. All of the substrates used in this study were miscut along the [011] direction so that the edges of the terraces are in the $[0\bar{1}1]$ direction. The overall surface of the film is parallel to a plane formed by rotating the (100) plane by α degrees about the $[0\bar{1}1]$ direction - thus $[0\bar{1}1]$ is the mean direction of the atomic step edges.
RHEED images of the 2° MgO substrate taken after the UHV heat treatment, but before film deposition, give a miscut angle of 2.1°. Further RHEED measurements of this substrate after deposition of the 45nm Fe_3O_4 film showed that the average terrace width is 5.7 ± 0.5nm, consistent with the miscut angle [16].
Two sets of Fe_3O_4 films were grown by molecular beam epitaxy (MBE) on single crystal MgO substrates vicinal to (100). The first set consisted of films of thickness 45nm on substrates with miscut angle, α, of 2°, 5° or 10°. The second set were films of thickness 30 nm, 45 nm and 70 nm deposited on the 2° miscut substrates. The substrates were cleaned chemically prior to insertion into the growth chamber and were further cleaned in situ at 600°C in UHV for 1 hour followed by annealing in oxygen at $1x10^{-5}$ torr for 6 hours. The Fe_3O_4 films were grown by the electron beam evaporation of metallic iron (99.999%) in the presence of free oxygen radicals generated by an ECR (electron cyclotron resonance) plasma source. The substrate temperature during growth was 250°C. Further details of the growth procedure are given in Section 2.2.4, and in [16].

Detailed characterisation of the films' properties are given in reference [16], with results as follows. Reflection high energy electron diffraction (RHEED) measurements confirmed that the films grew in a layer-by-layer mode at a rate of 0.3Å/sec. High resolution x-ray diffraction (HRXRD) rocking curves showed that, for the above film, the out of plane lattice constant is 0.8372nm whereas the in-plane lattice constant is 0.8423nm, twice that of the MgO substrate (0.4213nm). This gives the volume of the unit cell as 0.594 nm^3, in full agreement with that of stoichiometric magnetite. It was inferred [16] from the in situ RHEED and the ex-situ HRXRD measurements

that the films grow pseudomorphically and maintain one-to-one registry with the MgO substrate.

6.3.2 FMR Measurements

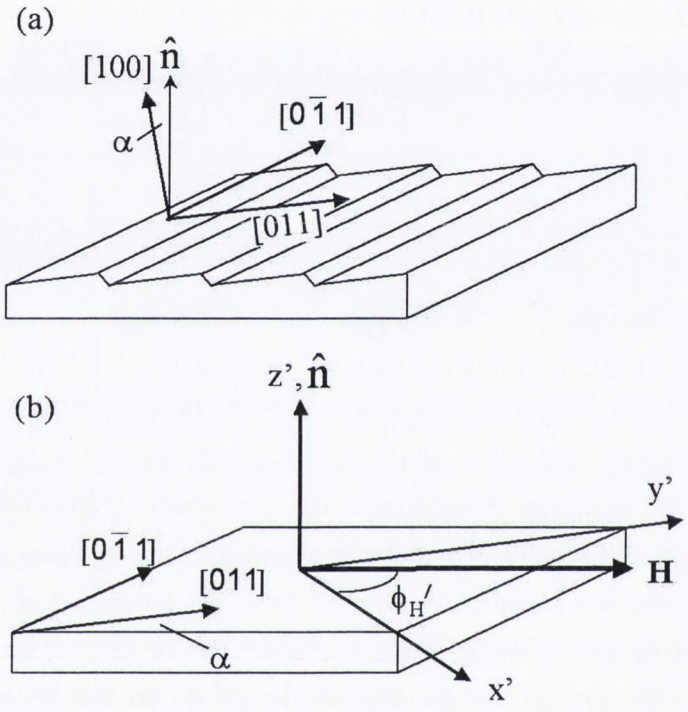

Figure 6.2: Schematic diagram of (a) the vicinal MgO (100) substrate characterised by (011) terraces with steps parallel to $[0\bar{1}1]$ and (b) the film. $\hat{n}$ is the normal to the film and x', y', are the projections of [010] and [001] respectively within the film plane. $\vec{H}$ lies in the film plane

The field position and width of the ferromagnetic resonance signal of the magnetite films was measured as a function of the direction of the applied field within the film plane.

All measurements were taken at room temperature on the X-band Bruker apparatus in Trinity College. Operating frequency for this apparatus is in the region of 9.6 GHz. The sample was mounted flat on the end of a vertical, spin free, quartz rod that could be rotated by a goniometer such that the magnetic field direction varied within the film plane. Further details are given in Chapter 3.3.1.

The direction of $\vec{H}$ within the film plane is given by the angle ϕ'_H as shown in Figure 6.2(b). For all films the angle ϕ'_H differs by less than 1° from ϕ_H, the angle between [010] and the projection of $\vec{H}$ in the (100) plane.

6.4 Results

A single FMR line was observed for all the samples. For each sample we measured the dependence of the ferromagnetic resonance field, H_R, on the direction of the external magnetic field, $\vec{H}$, as it was rotated within the plane of the film.

6.4.1 In plane angular dependence of resonance field for films of different thickness

Figure 6.3 shows the in-plane angular dependence of the resonance field for the Fe_3O_4 films of thickness 30nm, 45nm and 70nm on MgO (100) substrates with a fixed vicinal angle of 2°.

Figure 6.3(a) shows that the 70nm film displays the fourfold anisotropy to be expected for a cubic crystal. The minima in H_R occur at $\phi_H = 45°$, 135°,... corresponding to the projections within the film plane of the [011] type directions; this is consistent with previous FMR measurements for Fe_3O_4 on MgO as reported in earlier chapters, and in [13] and [9]. Details of the analysis are given in the next section and we just note here that, as shown in Fig. 6.4 (a), the angular dependence of H_R fits well to that expected for cubic magnetocrystalline anisotropy. However, Figures 6.3(b) and 6.3(c) show that for the 45 nm and 30 nm films the value of the resonance field for $\vec{H}$ parallel to [011], or, to be more exact, to its projection in the film plane ($\phi_H = 45°$), clearly differs from that for $\vec{H}$ parallel to $[0\bar{1}1]$ ($\phi_H = 135°$). This implies an inequivalence of the [011] and $[0\bar{1}1]$ directions that is a manifestation of an in-plane uniaxial anisotropy superimposed on the cubic anisotropy; the former increases in strength with decreasing thickness as shown in Figure 6.3. As discussed in detail in section 6.5.1 and as shown in Figures 6.3(b) and 6.3(c) a good fit to the angular dependence is obtained by including an in-plane uniaxial anisotropy term with axis along the step edge direction $[0\bar{1}1]$; however it is clear that the uniaxial easy axis is in the [011] direction, perpendicular to the step edge.

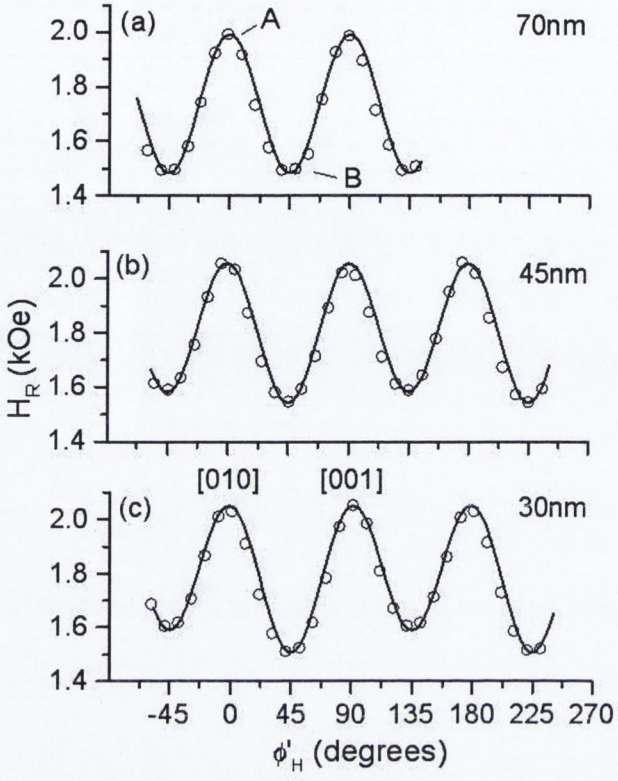

Figure 6.3: The in-plane ferromagnetic resonance field, H_R, as a function of angle ϕ'_H for Fe_3O_4 on 2° miscut vicinal MgO(100) with film thickness (a) 70 nm, (b) 45 nm, and (c) 30 nm. The solid lines are fits using Equation (6.2) with parameters given in Table 6.1. Note that the curvature at points A and B is very similar.

6.4.2 In plane angular dependence of resonance field for films of different miscut angle

Figure 6.4 shows the effect on the in-plane angular dependence of H_R of changing the vicinal angle, α, from 2° to 10° at a fixed film thickness of 45nm. Comparing Figures 6.4(a) and 6.4(b) shows that increasing α from 2° to 5° leads to an increase in the magnitude of the uniaxial term that manifests itself as an increase in the difference in the H_R value for the [011] and [0$\bar{1}$1] directions. Once again we see that the combination of the cubic term with a single in-plane uniaxial term yields a good fit as will be discussed in section 6.5.1. Figure 6.4(c) shows the angular dependence of H_R at a = 10°. Two points are worth noting about this plot. Firstly, H_R is further decreased along [011] and increased along [0$\bar{1}$1] (to such an extent in the latter

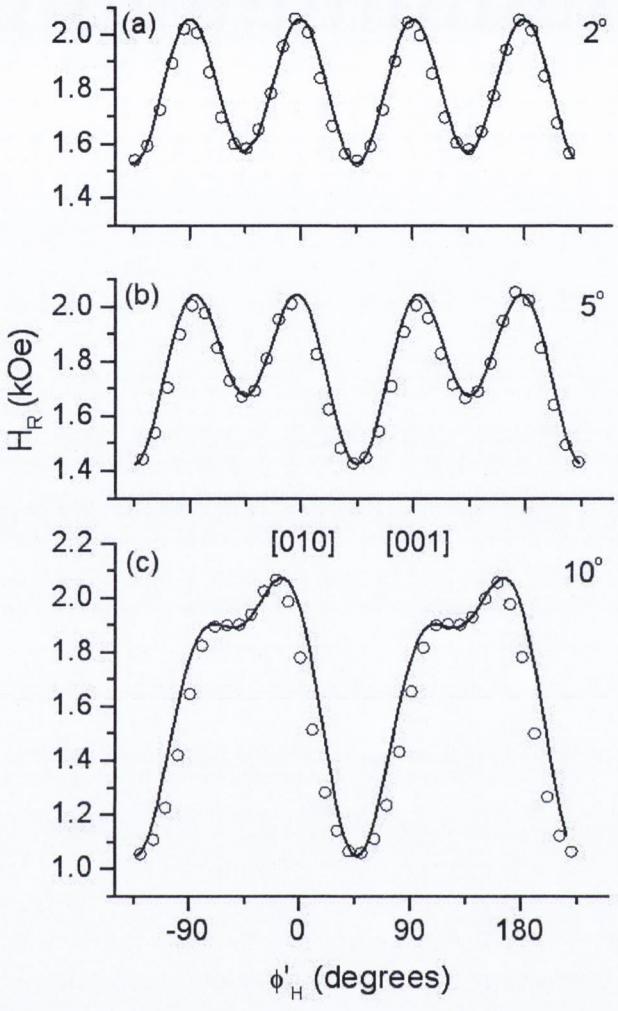

Figure 6.4: The in-plane ferromagnetic resonance field, H_R, as a function of angle ϕ'_H for 45 nm Fe_3O_4 on vicinal MgO(100) with miscut angle of (a) 2° (b) 5° and (c) 10°. The solid lines are fits using Equations (6.2) and (6.3) with parameters given in Table 6.1.

direction that the dip has disappeared) and this indicates a further increase in the magnitude of the previous uniaxial term. Secondly, there is an inequivalence in the directions [001] and [010]; we find that this can be accounted for by the inclusion of a second but weaker in-plane uniaxial term, this time with axis along [010], and Figure 6.4(c) shows that with this a good fit can be obtained.

6.4.3 In plane angular dependence of linewidth

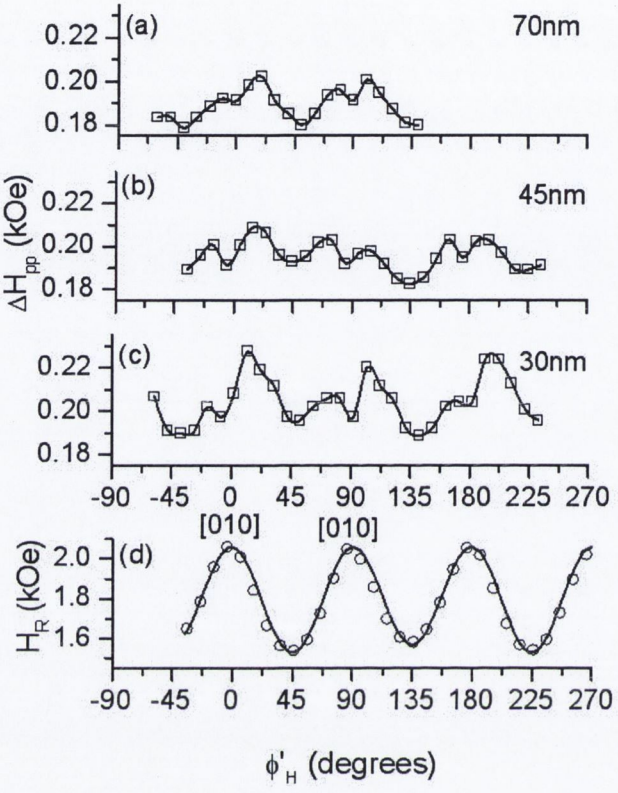

Figure 6.5: The in-plane ferromagnetic resonance linewidth, ΔH_{pp}, as a function of angle ϕ'_H for films with $\alpha = 2°$ and thickness, d, of (a) 70 nm (b) 45 nm and (c) 30 nm; the lines are guides to the eye. (d) H_R versus angle ϕ'_H for the film with $\alpha = 2°$, d = 45 nm with theoretical fit.

The dependence of the peak-to-peak FMR linewidth, ΔH_{pp}, on the applied field direction within the film plane was measured for all samples. Figure 6.5 shows the in-plane angular dependence of ΔH_{pp} for the films with thickness 70 nm, 45 nm and 30 nm on the $\alpha = 2°$ substrate; also shown to aid comparison is a plot of H_R versus angle ϕ'_H for the film with $\alpha = 2°$, d = 45 nm. It is clear that changing the thickness in this range has little effect on the linewidth. For the 70 nm film ΔH_{pp} varies approximately in step with H_R with minima when $\vec{H}$ is parallel to the in-plane easy axes in the [011] type directions; there also appear to be weaker minima along the [010] type directions. For the other two films there also appear to be linewidth minima along the [011] and [010] type directions. The linewidth variation is quite small, ranging from about 180 Oe to 200 Oe for the 70 nm and 45 nm films, and from 190 Oe to 225 Oe for the 30 nm film.

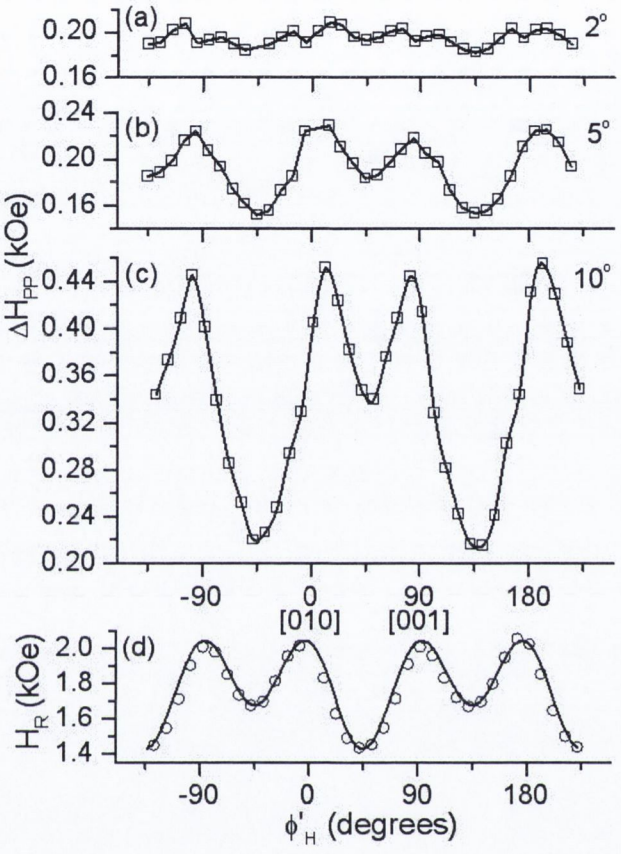

Figure 6.6: The in-plane ferromagnetic resonance linewidth, ΔH_{pp}, as a function of angle ϕ'_H for Fe_3O_4 films with d = 45 nm and vicinal angle, α, of (a) 2°, (b) 5° and (c) 10°; the lines are guides to the eye. (d) H_R versus ϕ'_H for the film with d = 45 nm, $\alpha = 5°$ with theoretical fit.

In contrast to the small effect of changing the film thickness, Figure 6.6 shows that changing the angle α at a fixed thickness, d, of 45nm, has a much larger effect on the linewidth. To aid comparison, the angular dependence of H_R for $\alpha = 5°$, thickness d = 45 nm is also shown in Figure 6.6(d). It is clear that for $\alpha = 5°$ and 10°, the minima of ΔH_{pp} are again along the [011] type directions but now the linewidth minimum along $[0\bar{1}1]$ is clearly less than that along [011]. The inequivalence of the [011] and $[0\bar{1}1]$ directions is therefore also revealed in the linewidth. Surprisingly, as Figure 6.6 shows, the ΔH_{pp} angular dependence pattern is shifted in angle by 90° relative to that of H_R. Finally we note that increasing α from 5° to 10° amplifies the variation in linewidth and also increases the mean value of ΔH_{pp}.

6.5 Analysis

6.5.1 Angular Dependence of the Magnetic Field

As described in section 3.2.5, we begin with the equation for the magnetic free energy density of the system (equation 3.12) . We use the formula for a crystal with both in-plane and out-of-plane fourfold and twofold anisotropies as described in sections 3.2.5 and 3.2.6 and in [60]:

$$\begin{aligned} E &= \frac{1}{2}M[-2H\left(cos\theta cos\theta_H + \sin\theta\sin\theta_H\cos(\phi-\phi_H)\right] + 4\pi M\cos^2\theta - H_{2\perp}\cos^2\theta \\ &\quad -\frac{1}{2}H_{4\perp}\cos^4\theta - H_{2||}\sin^2\theta\sin^2(\phi-\pi/4) - \frac{1}{2}H_{4||}\frac{1}{4}\left(3+\cos 4\phi\right)\sin^4\theta] \end{aligned} \tag{6.1}$$

Angles ϕ, ϕ_H, θ and θ_H as defined in Figure 3.2. Here, we have added the term $H_{2||}\sin^2\theta\sin^2(\phi-\pi/4)$ to the general energy equation 3.12 to incorporate the desired twofold anisotropy behaviour, implying a difference in energy between the cases of $\vec{H}$ || [011] and $\vec{H}$ || [0$\bar{1}$1]. This is to be expected since the step edges are parallel to [0$\bar{1}$1]. We expect that $K_{2||}$ depends on both vicinal angle and film thickness.

Using the general resonance equation 3.10:

$$\left(\frac{\omega}{\gamma}\right)^2 = \left(\frac{1}{M\sin\theta}\right)^2\left[E_{\theta\theta}E_{\phi\phi} - (E_{\theta\phi})^2\right]$$

and Equation (6.1) we calculate the general resonance condition:

$$\left(\frac{\omega}{\gamma}\right)^2 = \left[\left(H\times a_1 + b_1\right)\left(H\times a_1 + b_2\right) - b_3^2\right]$$

where:

$$
\begin{aligned}
a_1 &= \cos\theta\cos\theta_H + \sin\theta\sin\theta_H\cos(\phi-\phi_H) \\
b_1 &= -\left(4\pi M - H_{2\perp} + H_{2||}\cos^2\left(\phi+\frac{\pi}{4}\right)\right)\cos 2\theta + H_{4\perp}\frac{\cos 2\theta+\cos 4\theta}{2} \\
&\quad + H_{4||}\frac{\cos 4\theta-\cos 2\theta}{2}\frac{3+\cos 4\phi}{4} \\
b_2 &= -(4\pi M - H_{2\perp})\cos^2\theta + H_{4||}\sin^2\theta\left(\cos 4\phi - \cos^2\theta\frac{3+\cos 4\phi}{4}\right) + H_{4\perp}\cos^4\theta \\
&\quad - H_{2||}\left[\sin 2\phi + \left[\cos\theta\cos\left(\phi+\frac{\pi}{4}\right)\right]^2\right] \\
b_3 &= \frac{1}{2}\cos\theta\left(\frac{3}{2}H_{4||}\sin 4\phi\sin^2\theta + H_{2||}\cos 2\phi\right)
\end{aligned}
$$

We now consider what is the appropriate resonance condition for the present case, where the applied field $\vec{H}$ lies within the film plane, which is tilted from the (100) plane by an angle α about the step edge direction $[0\bar{1}1]$. We define a new set of axes x', y', z' as shown in Figure 6.2, where z' is the film normal and x', y' are the projections of [010], [001] respectively into the film plane. Since in our experiments $\vec{H}$ lies in the film plane we have taken ϕ'_H as the angle between $\vec{H}$ and the x' direction. Similarly, since $\vec{M}$ will also lie within or very close to the film plane, we take ϕ' as the angle between $\vec{M}$ and x'. The angle θ'_H between $\vec{H}$ and z' (the film normal) is 90° and also $\theta' \approx 90°$. We estimate that, for all $\alpha \leq 10°$, $|\phi_H - \phi'_H| < 1°$ and so to very good approximation we take $\phi_H = \phi'_H$. It is also reasonable to suppose that $\phi = \phi'$. As regards the other angles, θ_H varies between 90° for $\vec{H}$ || (at ϕ'_H = -45°) and 90° + α for $\vec{H}$ || [011] (at ϕ'_H = 45°); a very similar variation for θ is expected. If we make the reasonable approximation that in our case, $\theta \approx \theta_H$ and $\theta' \approx \theta'_H$, then the errors in taking $\theta_H \approx \theta'_H$ amount to only about 3%, 6% and 3% in the cases of $\sin^2\theta$, $\sin^4\theta$ and $\cos^2\theta$ respectively. Since these errors are small we make the simplifying assumption that $\theta = \theta' = \theta_H = \theta'_H = 90°$, as well as $\phi = \phi'$ and $\phi_H = \phi'_H$ to obtain the resonance condition for our case to be:

$$
\begin{aligned}
\left(\frac{\omega}{\gamma}\right)^2 &= \left(H\cos(\phi'-\phi'_H) + 4\pi M_{eff} + H_{4||}\frac{3+\cos 4\phi'}{4} + H_{2||}\sin^2\left(\phi'-\frac{\pi}{4}\right)\right)\times \\
&\quad \left(H\cos(\phi'-\phi'_H) + H_{4||}\cos 4\phi' - H_{2||}\cos\left(2\phi'-\frac{\pi}{2}\right)\right) \qquad (6.2)
\end{aligned}
$$

where $4\pi M_{eff} = 4\pi M$ - $H_{2\perp}$.

When the magnetisation lags appreciably behind the in-plane applied field (i.e. when $\phi \neq \phi_H$), a plot of resonance field versus ϕ_H exhibits a smaller curvature for $\vec{H}$ along the easy axis than for $\vec{H}$ along the hard axis, as reported in [71,72]. However, as shown in in Figure 6.3(a), the curvatures at points A and B are very similar and therefore we also take $\phi' = \phi'_H$.

Table 6.1: Parameters extracted from fits of theoretical model (equations 6.2 and 6.3) to the experimental data for Fe_3O_4 films of thickness, d, on vicinal MgO(100) substrates miscut by angles α

$\alpha(^\circ)$	d(nm)	$H_{2\|\|}$(Oe)	$H_{4\|\|}$(Oe)	$4\pi M_{eff}$(kOe)	$H'_{2\|\|}$(Oe)
2	70	0 ± 5	-305 ± 7	4.52 ± 0.03	–
2	45	-23 ± 5	-305 ± 7	4.23 ± 0.03	–
2	30	-47 ± 5	-307 ± 7	4.28 ± 0.03	–
5	45	-142 ± 5	-295 ± 7	4.34 ± 0.03	–
10	45	-480 ± 20	-230 ± 20	5.2 ± 0.2	190 ± 20

Fits of Equation (6.2) to the experimental data are shown in Figures 6.3(a), (b) and (c), and Figures 6.4(a) and (b), which were fit using the parameters shown in Table 6.1. We can see that the data fits well to the angular dependence predicted by equation 6.2 with $\phi' = \phi'_H$. The fits were evaluated with g = 2.12 [38]. Figure 6.4(c) shows that for $\alpha = 10°$, in addition to the inequivalence of $\vec{H}$ || [011] and $\vec{H}$ || [0$\bar{1}$1], there is an inequivalence of $\vec{H}$ || [010] and $\vec{H}$ || [001] that is not accounted for by equation 6.2. One possible reason for this inequivalence could be the presence of kinks in the step edge. It is possible that for the larger values of α, miscutting the MgO (100) surface along the [011] direction may not produce exactly straight step edges, but rather a ragged edge, with some portions along [0$\bar{1}$1] and others along another direction. Since imaging of the MgO surface is difficult in ambient due to the formation of hydroxide we cannot confirm that this is the case; however the presence of step portions along one of the principal crystal axis directions could induce this additional inequivalence that is observed. In an attempt to account for this we introduce a further in-plane uniaxial anisotropy density term E'$_A$ with axis along [010] so that:

$$E'_A = -K'_{2||}\beta_x^2 = -K'_{2||}\sin^2\theta\sin^2\phi$$

where β_x is the direction cosine between $\vec{H}$ and the [010] direction.
With the same assumptions as before this leads to the resonance condition:

$$\left(\frac{\omega}{\gamma}\right)^2 =$$
$$\left(H\cos(\phi'-\phi'_H)+4\pi M_{eff}+H_{4||}\frac{3+\cos 4\phi'}{4}+H_{2||}\sin^2\left(\phi'-\frac{\pi}{4}\right)+H'_{2||}\sin^2\phi'\right)\times$$
$$\left(H\cos(\phi'-\phi'_H)+H_{4||}\cos 4\phi'-H_{2||}\cos\left(2\phi'-\frac{\pi}{2}\right)-H'_{2||}\cos 2\phi'\right) \qquad (6.3)$$

Figure 6.4(c) shows that Equation 6.3 gives a good fit to the data. The parameters used in the fit are given in Table 6.1.

Table 6.1 shows that both $H_{2||}$ and $H_{4||}$ are negative and that the one value of $H'_{2||}$ is positive. This implies that, as regards anisotropy contributions to the free energy density, the cubic term gives a minimum along [011] type directions, the first uniaxial term gives a minimum along [011], that is perpendicular to the step edge direction , and the second uniaxial term gives a minimum along [001].

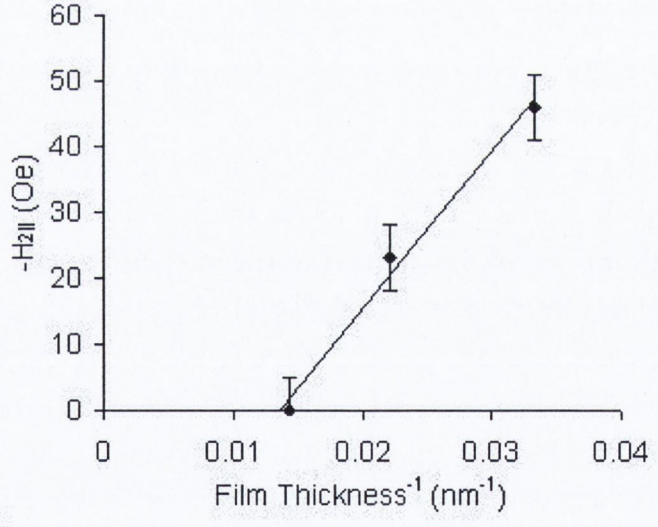

Figure 6.7: Dependence of the uniaxial anisotropy field $H_{2||}$ on 1/film thickness for a constant $\alpha = 2°$; the line is a best fit with parameters given in the text.

The most interesting parameter for these films is the uniaxial anisotropy field $H_{2||}(= 2K_{2||}/M)$. Examining the variation in $H_{2||}$ with changing film thickness, Table 6.1 shows that the magnitude of $H_{2||}$ increases as the film thickness, d, decreases. Plotting a graph of $H_{2||}$ vs 1/d (shown in Figure 6.7), we find that, for $\alpha = 2°$, the dependence of $H_{2||}$ on d is given by:

$$H_{2||} = A + \frac{B}{d}$$

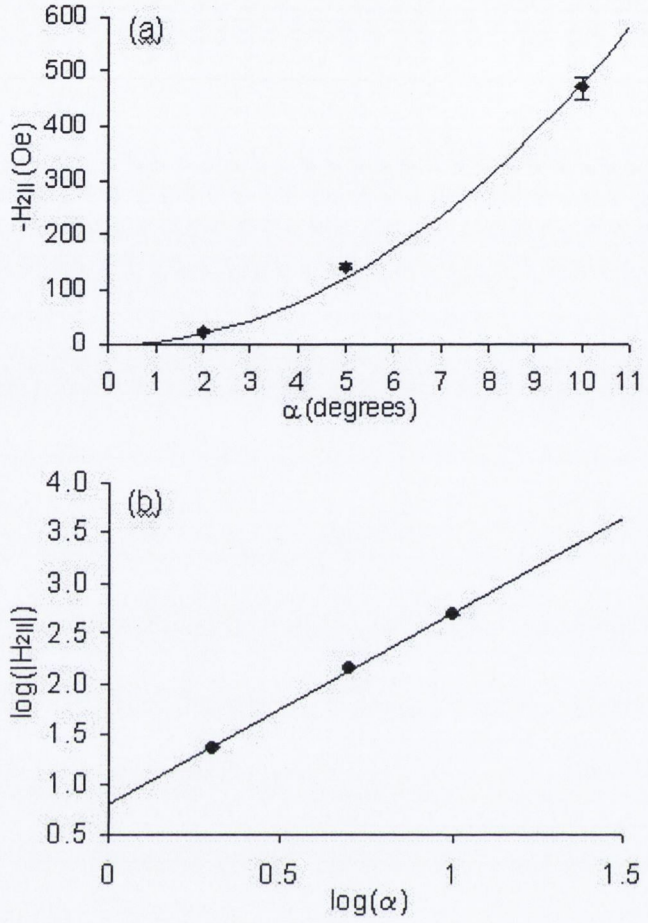

Figure 6.8: Dependence of $H_{2||}$ on vicinal angle a shown with (a) linear scales and (b) log scales. Shown are fits in (a) of $H_{2||} = 4.8\alpha^2$ and in (b) of $\log(|H_{2||}|) = 1.89 \log(\alpha) + 0.80$. Each film has a thickness of 45nm.

with A = 33 ± 6 Oe and B = -(2.4 ± 0.2) x10^{-4}Oe.cm. Now looking at the variation of $H_{2||}$ with changing miscut angle, we plot the values of $H_{2||}$ given in Table 6.1 vs α for the 45nm thick films (shown in Figure 6.8(a)). This shows that $H_{2||}$ varies almost quadratically with α; the log-log plot shown in Figure 6.8(b) gives the exponent to be 1.89 ± 0.06. Thus we can express $H_{2||}$ in the form:

$$H_{2||} = \left(\frac{90}{\pi}\right)^2 \left(A + \frac{B}{d}\right) \alpha^2 \tag{6.4}$$

where $H_{2||}$ is in Oe, α in radians and A, B have the values given above. Equation 6.4 gives the values of $H_{2||}$ in Oe of -1.3 , -20.3, -47, -127 and -507 for (α, d) of (2°, 70nm), (2°, 45nm), (2°, 30nm), (5°, 45nm) and (10°, 45nm) that agree well with the measured values of 0 5, -23 ± 5, -47 ± 5, -142 ± 5 and -480 ± 20 respectively.

We now consider what may give rise to this expression for $H_{2||}$ and begin with the term in α^2/d. Kawakami et al [79] showed that for a stepped (001) bcc film there should be an in-plane uniaxial anisotropy

$$\left(\frac{K_{sp}}{a} - K_s\right)\frac{\alpha^2}{d}$$

where K_s, K_{sp} are the surface and step anisotropy constants respectively and a is the step height. This result was obtained using a model based on that proposed by Neel [87] but which kept only its functional form reflecting the symmetry of the lattice. The in-plane uniaxial anisotropy of bcc Fe grown on stepped Ag(001) [79] and of Fe on curved W(001) [82] is found to show an α^2 dependence, similar to the one in magnetite. By contrast, for an fcc lattice, the steps can give rise to a linear dependence of the induced anisotropy on step density as has been observed [79] for fcc Co on curved Cu (001). Spinel Fe_3O_4 is a lot more complex than a metal, for example Fe, and first-principles derivation of anisotropy cannot readily be done. However, studies undertaken using the magneto-optical Kerr effect (MOKE) on epitaxial films of magnetite on GaAs(100) [88] found that surface-induced anisotropy effects to be present in the films. Interfacial effects were also reported for low-indexed Fe_3O_4/NiO interfaces [89] - here, x-ray magnetic circular and linear dichroism (XMCD and XMLD) studies showed differing magnetic coupling phenomena for (100), (111) and (001) interfaces of NiO films on single-crystal Fe_3O_4, highlighting the interface effects.

In order to get an estimate of the anisotropy constants we assume that our α^2/d term in Equation 6.4 can be identified with that for the bcc film so that:

$$\left(\frac{90}{\pi}\right)^2 \equiv 2\left(\frac{K_{sp}}{a} - K_s\right)\frac{\alpha^2}{dM} \tag{6.5}$$

with B = -(2.4 $\pm$ 0.2) x 10^{-4}Oe.cm. For the $\alpha = 2°$ films the mean terrace width is 5.7 nm (as reported in [16]) and so the step height a $\approx$ 0.2nm; we assume the same value of a for all films. From previous measurements of M(H) [16] we find that M $\approx$ 432 emu/cm^3 in the field range of our FMR experiments. Therefore we obtain (K_{sp}/a - K_s) $\approx$ -42 erg/cm^2. If $K_{sp}/a >> K_s$ then $K_{sp} \approx$ -8.5 x 10^{-7} erg/cm, a value greater than that of 5.73 x 10^{-8} erg/cm found for Fe/stepped Ag(001) [79].

Now, we turn our attention to the other term in Equation 6.4, $(90/\pi)2A\alpha^2$, that is independent of film thickness. Its independence of film thickness implies that it can

be associated with a uniaxial volume contribution K_U^V so that we may write:

$$H_{2||} = \left(\frac{90}{\pi}\right)^2 \left(A + \frac{B}{D}\right) \alpha^2 \equiv 2\left(K_U^V + \frac{1}{d}\left[\frac{K_{sp}}{a} - K_s\right]\right)\frac{\alpha^2}{M} \tag{6.6}$$

Using the previous values of A and M we obtain $K_U^V \approx 6 \times 10^6$ erg/cm^3. Leeb et al [80] found that the in-plane uniaxial anisotropy constants, K_u^{eff}, for Fe films on vicinal Ag(001) and Au(001) fit to a similar expression

$$K_U^{eff} = K_U^V + \frac{2K_U^S}{d}$$

although the values of K_U^V = -2.3 x 10^4 erg/cm^3 and 1.6 x 10^4 erg/cm^3 found for Fe/Ag and Fe/Au respectively are much smaller than the value we find for Fe_3O_4/MgO. It is interesting to note that for Fe/curved W(001) and Fe/Vicinal Ag(001) [78] the in-plane uniaxial anisotropy was found to be thickness independent although varying as α^2. In these latter cases the thickness independence was attributed to the presence of strain. Wu et al [78] suggested that 1/d dependence was seen by Leeb et al [80] because the strain was relaxed, possibly as a result of depositing the Ag and Au seed layer on a stepped GaAs (001) substrate with vicinal angle of 2°. HRXRD studies of our films show that strain is isotropic within the plane of the film [43] and cannot contribute to the uniaxial volume term K_U^V. Instead of being linked to strain, the K_U^V term may be related to the preferential alignment of the APBs parallel to the step edges [16]. These defects propagate though the entire thickness of the film and therefore could produce an anisotropy energy proportional to the volume of the film.

Turning now to the value of $H_{4||}$ (= $2K_{4||}/M$) we note that its value of -305 Oe found for samples with $\alpha = 2°$ is similar to that of $2K_{4||}/M$ = 380Oe obtained by Van der Heijden et. al [13] for Fe_3O_4 films grown on MgO (100) using MBE. The former value is 65% of that of 466 Oe for magnetite single crystals [63] which is indicative of a high crystalline quality of these films. We note that the values of $2K_{4||}/M$ for magnetite produced by sputtering [9] and pulsed laser deposition [12] differ substantially from those for the bulk single crystals [38].

6.5.2 Angular Dependence of the Linewidth

The striking feature of the results is the development of a strong in-plane angular

dependence of the peak-to-peak linewidth, ΔH_{pp}, for the 45nm thick film as the vicinal angle is increased from 2° to 10°. By contrast the angular dependence of ΔH_{pp} for $\alpha = 2°$ remains rather small as the thickness is changed between 30nm and 70nm.

As explained in Section 3.2.7 we can express the linewidth as

$$\Delta H_{pp} = \Delta H_{hom} + \Delta H_{inhom}$$

where the homogeneous contribution, ΔH_{hom}, arises from the intrinsic damping of the magnetisation and ΔH_{inhom} comes from the magnetic inhomogeneities of the sample; both can have an angular dependence. The homogeneous contribution is given by [59,61]

$$\Delta H_{hom} = \frac{1}{\sqrt{3}} \frac{1}{|\partial\omega/\partial H|} \frac{G}{M^2} \left(\frac{\partial^2 F}{\partial\theta^2} + \frac{1}{\sin^2\theta} \frac{\partial^2 F}{\partial\phi^2} \right) \tag{6.7}$$

where G is the Gilbert damping parameter. Using equations (6.1), (6.2) and (6.7) we calculate that

$$\Delta H_{hom} = \frac{2}{\sqrt{3}} \frac{G\omega}{\gamma^2 M} \frac{1}{\cos(\phi - \phi_H)} \tag{6.8}$$

Since in our case the magnetic field used is strong enough to align the magnetisation along the applied field direction to within a few degrees, the value of ϕ - ϕ_H, and hence the deviation of cos(ϕ - ϕ_H) from unity, is very small. Therefore this contribution is almost constant and so could not be the cause of the angular variation of the linewidth.

Another possibility is that the angular dependence of the linewidth comes from that of the inhomogeneous contribution ΔH_{inhom}. The magnetic inhomogeneities, arising from sample imperfections, such as mosaic structure and defects, can give rise to a distribution in the directions of both the crystal and magnetic anisotropy axes as well as a spread in the magnitudes of the internal fields. So, following Chappert et al [62], we write

$$\Delta H_{inhom} = \Delta H_0 + \sum_i \frac{\partial H_R}{\partial \phi_i} \Delta\phi_i + \sum_j \frac{\partial H_R}{\partial H_j} \Delta H_j \tag{6.9}$$

For our case we are only considering the in plane variation and so the angular spread $\Delta\phi_i$ includes spreads in the direction of the axes of the cubic and uniaxial anisotropy and ΔH_j includes spreads in $H_{4||}$, $H_{2||}$ and M_{eff}. Several of these terms can be ruled out because they give angular dependencies of ΔH that do not fit to the observed

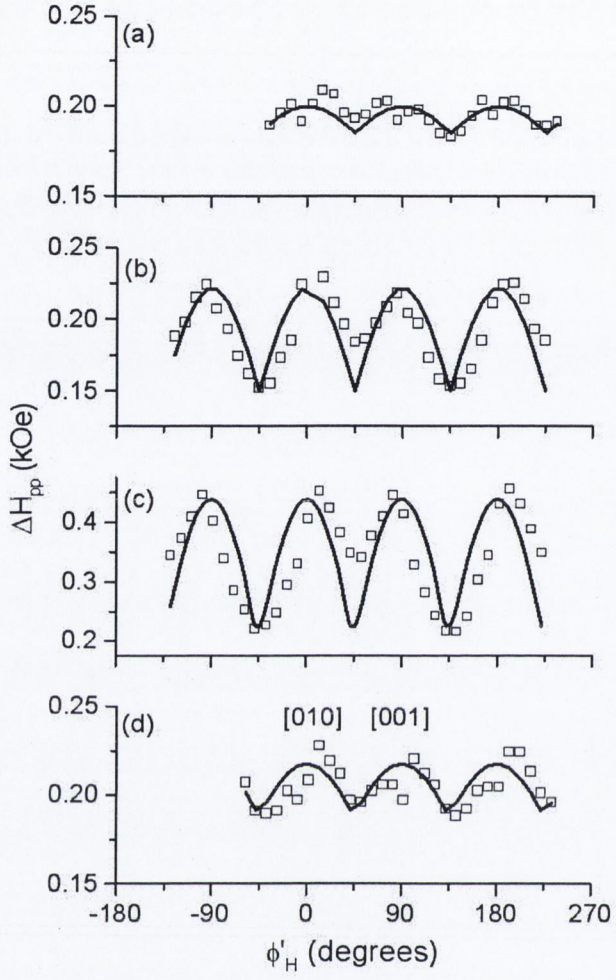

Figure 6.9: The in-plane ferromagnetic resonance linewidth, ΔH_{pp}, as a function of angle ϕ'_H for Fe_3O_4 films with d, α values of (a) 45nm, 2° (b) 45nm, 5° (c) 45nm, 10° and (d) 30nm, 2°. The lines show fits to $\Delta H_{pp} = \Delta H_0 + (\partial H_R/\partial \phi_u)\Delta\phi_u$ with parameters given in the text.

dependencies. The linewidth is found to have maxima at $\phi_H = 0, \pi/2, \pi, \ldots$ with minima in between the two adjacent values. However, Equations (6.2) and (6.9) imply that a spread in the direction of cubic axes and the magnitudes of $H_{4||}$, $H_{2||}$ and M_{eff} would give linewidth maxima at ($\pi/8$, $3\pi/8$, $5\pi/8$,...), (0, $\pi/4$, $2\pi/4$, ...), and ($\pi/4$, $3\pi/4$, $5\pi/4$, ...) respectively; none of these match the data. However, a spread, $\Delta\phi_U$, in the direction of the axis of the uniaxial term $H_{2||}$ does give maxima at $\phi_H = 0, \pi/2, \pi, \ldots$ as observed. The in-plane angular dependence of ΔH_{pp} calculated on this basis is shown in Figure 6.9, with parameters used in the fits as shown in Table 6.2 (other parameters are as shown in Table 6.1).

Table 6.2: Parameters used in fitting the linewidth behaviour using Equations (6.2) and (6.9) for Fe_3O_4 films of thickness, d, on vicinal MgO(100) substrates miscut by angles α

$\alpha(^\circ)$	d(nm)	$\Delta\phi_U(^\circ)$	ΔH_0 (kOe)
2	45	29	0.19
5	45	23	0.15
10	45	23	0.2
2	30	29	0.19

These angular spreads seem unrealistically large but they may be related to the rugged character of the step edges. The increase in the variation of ΔH_{pp} as α increases, even though $\Delta\phi_U$ remains nearly constant comes from the increase in $H_{2||}$.

It is clear from Figure 6.9 that the spread $\Delta\phi_U$ does not fully account for the observed linewidth variation as the linewidth for $\vec{H}$ along [011] and hence perpendicular to the step edges is greater than for $\vec{H}$ along $[0\bar{1}1]$ and parallel to the edges. However this difference may arise from two magnon scattering as Arias and Mills [74] have predicted that for stepped surfaces this mechanism will give rise to a maximum linewidth when $\vec{M}$ is perpendicular to the edges and a minimum when it is parallel; as previously indicated the difference in direction of $\vec{M}$ and $\vec{H}$ should be small in the present case.
In brief, the angular variation of ΔH_{PP} for the films may be largely accounted for by a combination of that arising from a spread $\Delta\phi_U$ together with two magnon scattering by the steps. With magnon scattering the values of $\Delta\phi_U$ necessary to provide the required amplitude for variation with period $\pi/2$ would be smaller (and more plausible) than those used for the fits in Figure 6.9.

6.6 Conclusions

Fe_3O_4 films on vicinal MgO(100) with step edges parallel to $[0\bar{1}1]$ have an in-plane uniaxial anisotropy with easy axis perpendicular to the step edge. The strength of this anisotropy varies approximately quadratically with the vicinal angle. As regards its dependence on film thickness, d, it can be represented by the sum of two terms, one of which is independent of d and the other one proportional to 1/d. The latter is associated with an anisotropy localized at the interface, most likely at the steps, and the first may be associated with APBs preferentially aligned with the step edges. A second, weaker, in-plane uniaxial anisotropy is present in the film on

the 10° miscut substrate, which we attribute to an uneven step edge configuration. The FMR linewidth also exhibits an in-plane anisotropy that increases in magnitude as the vicinal angle increases but is almost independent of thickness, in the range 30-70nm, of films on the 2° miscut substrate.

Chapter 7

FMR Characterisation of Fe Nanowires

7.1 Introduction

In recent years there has been increasing interest in the production and properties of nanostructured materials partly driven by their potential applications. In this chapter we are concerned with nanowires of Fe. One way of forming such one-dimensional structures is to use a stepped substrate and the idea of using the steps as nucleation centers for deposited atoms was proposed many years ago by Basset [45] and Bethge [46]. Simulations of the growth of Fe nanostripes on stepped Cu(111) surfaces were recently carried out by Negulyaev et. al. [35] and there are several reports of measurements on such structures [25–28]. Of particular interest is the magnetic anisotropy of such structures and FMR is a good technique to use to study this. As far as we are aware there are no published reports of FMR studies of ferromagnetic wires on stepped substrates, but there are several reports [29], [30–34] of FMR measurements of such wires embedded in an insulating membrane. These measurements show that for low density arrays the angular dependence of the FMR spectrum can be interpreted in terms of the shape demagnetisation anisotropy of an isolated wire which gives the easy axis parallel to the wire. However, at high densities the dipolar interactions must be included and these yield an effective uniaxial field oriented perpendicular to the wire axis. For high densities therefore the material behaves as a thin film with the easy axis being within the film plane. It is clearly of interest to make FMR measurements on a two-dimensional array of wires such as those formed on a stepped substrate to examine the magnetic anisotropy in this case. Recently the equipment for making such arrays was installed in the School of Physics, TCD, and arrays have been made by members of Prof. Shvets' group.

We therefore decided to make FMR measurements on some of these samples. In particular, FMR measurements were made on three samples of Fe nanowires deposited on a stepped sapphire substrate, and the results are presented in this chapter. The results are preceded by some details of the sample preparation and FMR procedure and are followed by analysis, discussion and conclusions.

7.2 Experimental Details

7.2.1 Sample Preparation

Table 7.1: Details of Fe nanowire samples

Designator	Deposition Time (min)	Width (nm)		Spacing (nm)		Height (nm)
		Mean	Range	Mean	Range	
S-1	25min	25	15–30	10	0–40	1–2
S-2	34min	20	10–30	10	0–20	1–2
S-3	45min	50	35–70	20	0–50	1–2

Iron nanowires were prepared by Floriano Cuccureddu in TCD using the ATLAS system described in Section 2.3.3 and in the paper by Shvets et. al. [24]. The iron was deposited on a c-plane sapphire stepped substrate that was miscut by 3° along the $(1\bar{2}10)$ direction. The terraces were estimated to be 30-80nm wide with a step height of 2-4nm (private communication from Floriano Cuccureddu, TCD). The substrate was not separately heated and was nominally at room temperature. The temperature of the iron source was 1462°C, close to the melting point of iron of 1540°C. This was expected to give a deposition rate of 2.37 Å per minute for normal incidence but the beam was directed up the terrace at only 3° to the level of each terrace and so the actual deposition rate must be much less. Three samples were prepared with deposition times of 25 min, 35 min and 45 min, the AFM images of which are shown in Figures 7.1, 7.2 and 7.3. The light stripes correspond to the wires. The AFM images in Figure 7.1 show that most of the wires deposited during 25min have a rather well defined width of about 25nm but the overall range is from about 15 to 30 nm. By contrast, the wire spacing is much less regular with a mean of about 10 nm but with a spread from 0 to 37 nm. The AFM images in figures 7.2 and 7.3 of the wires deposited during 34 and 45 min show that these wires are not so regular in width; there is clearly also a spread in the spacing. Estimates of width and spacing are given in Table 7.1. In each case the wire heights are estimated to

be only 1-2 nm (Cuccureddu, private communication).

7.2.2 FMR Experimental Details

Figure 7.4 shows the coordinate system used to define the direction of $\vec{H}$ and $\vec{M}$ with respect to the nanowires and substrate.

FMR spectra were recorded as a function of the orientation of $\vec{H}$ within three planes: x-y, y-z and x-z. For rotation of $\vec{H}$ within the y-z plane the sample was mounted horizontally on the end of a vertical, spin free, quartz rod that could be rotated about its axis by a goniometer as described in Section 3.3.1. For rotation of $\vec{H}$ within planes x-y or x-z the sample was mounted vertically as illustrated in Figure 3.5.

All measurements were taken at room temperature on the X-band Bruker spectrometer in Trinity College using a rectangular TE_{102} mode cavity operating at 9.6GHz. The magnetic field position was calibrated using a Hall probe or NMR magnetometer and an EPR reference signal due to F^+ centers in MgO with known g-value (2.0023).

7.3 FMR Results

Two sets of measurements were made on the samples. The first set were made within a week of the samples being made. In this case the FMR spectrum was recorded as a function of orientation within the x-y plane (fixed $\theta_H = 90°$) and also within the x-z plane (fixed $\phi_H = 0°$); two lines were observed. The second set consisted of measurements on all samples of the effect of rotating the field within the y-z plane ($\phi_H = 90°$); this set was taken about two weeks later and only one of the lines remained. Although the samples were stored in a dessicant it is likely that some oxidation occurred at the surface. The line that disappeared is presumably associated with Fe ions at the surface whereas the one that remains may be associated with Fe ions deeper within the wires. The results of the first and second sets of experiments are given in Sections 7.3.1 and 7.3.2 respectively.

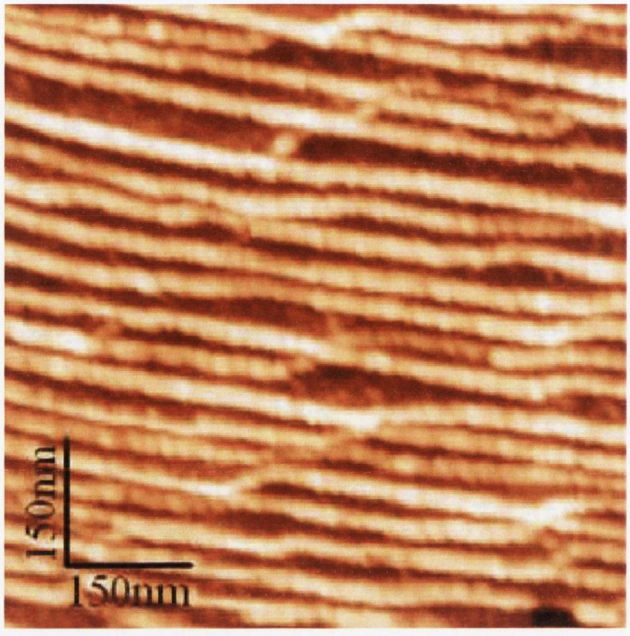

Figure 7.1: AFM image of the nanowire sample with deposition time of 25min

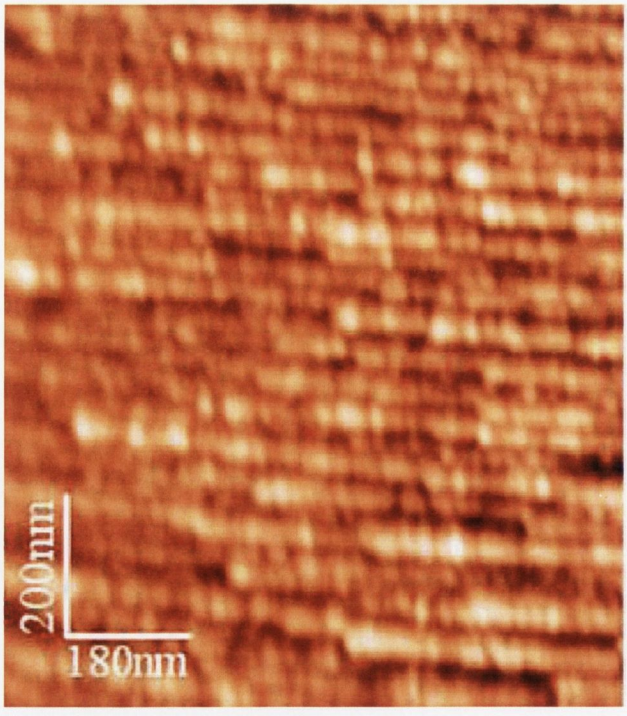

Figure 7.2: AFM image of the nanowire sample with deposition time of 34min

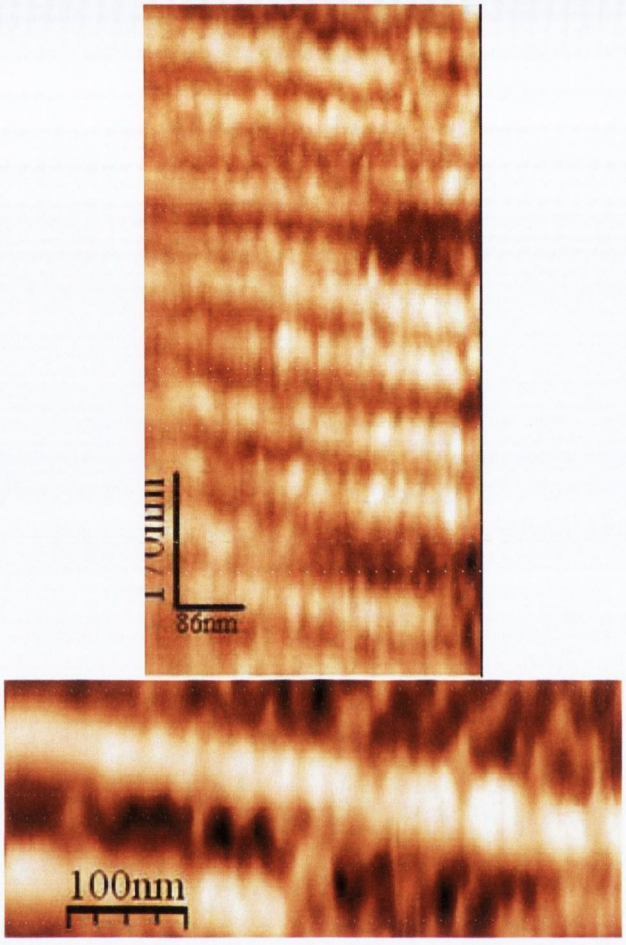

Figure 7.3: AFM images of the nanowire sample with deposition time of 45min

7.3.1 Out of Plane Angular Dependence of Resonance Field

Figures 7.5 and 7.6 show how the FMR spectrum of sample S-1 is dependent on the direction of $\vec{H}$ within both the x-y and x-z planes. Very similar spectra are obtained for samples S-2 and S-3. It is clear from some of the spectra in Figure 7.6 that two lines, labeled 1 and 2, are present and that they are not separately resolved for $\theta_H \geq 30°$. Line 1 is still present several weeks later but line 2 has by then disappeared. In view of this we will concentrate our attention on line 1.

One might expect the FMR spectrum to exhibit an axial symmetry with axis parallel to the nanowire direction. Figures 7.5 and 7.6 show very clearly that this is not the case and instead that the spectra display axial (or near axial) symmetry about the z-axis and there is a very large difference in the spectra for the two directions perpendicular to the wires, $\vec{H}$ parallel to $\hat{x}$ and $\vec{H}$ parallel to $\hat{z}$, with the z axis corresponding to the hard axis. As in many cases the lines 1 and 2 overlap, their positions were determined by fitting the spectra to the superposition of two lines.

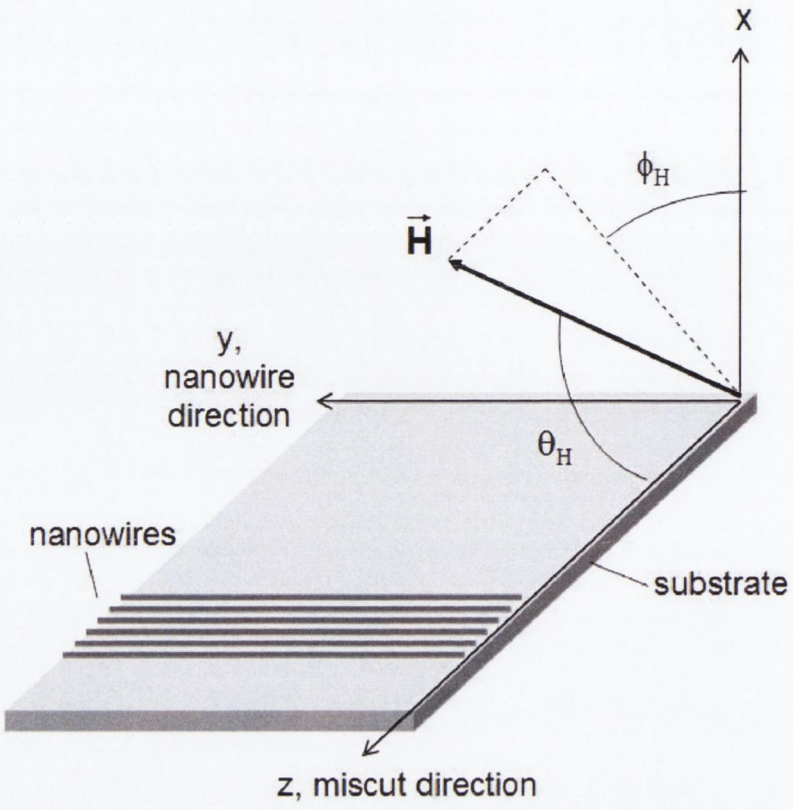

Figure 7.4: Coordinate system used to define the direction of $\vec{H}$. ϕ_H is the angle between the x-axis and the projection of $\vec{H}$ within the x-y plane. The equilibrium direction of $\vec{M}$ is defined by a corresponding pair of angles ϕ, θ.

Figures 7.7 and 7.8 show two spectra with their fits for field directions within the x-y plane and x-z plane respectively. Both lines used in the fits have a Lorentzian (1st derivative) shape; good fits are obtained. Figure 7.9 shows how the resonance field, H_R, and peak-to-peak linewidth, ΔH_{PP} for both lines 1 and 2 vary with the field direction within both the x-y and x-z planes. As mentioned before, line 2 disappears after several weeks whereas line 1 is not noticeably changed, so we will confine our remarks to line 1. The axial symmetry, about axis z, is made plain in Figure 7.9 (a) and (b), and the large increase in both H_R and ΔH_{PP} as $\vec{H}$ is rotated towards the z-axis (at $\theta_H = 0$) is apparent from figure 7.9 (c), (d). Indeed it is not possible to measure either the position or width of line 1 for $\theta_H \leq 8°$ because firstly the linewidth has become very large and secondly because the resonance field appears to exceed the maximum field (≈ 7 kOe) of our magnet.

Very similar results were obtained for the other two samples; the angular dependence of H_R and ΔH_{PP} for lines 1 and 2 for rotation of $\vec{H}$ in the x-y and x-z planes are shown in Figures7.10 and 7.11 for samples S-2 and S-3 respectively.

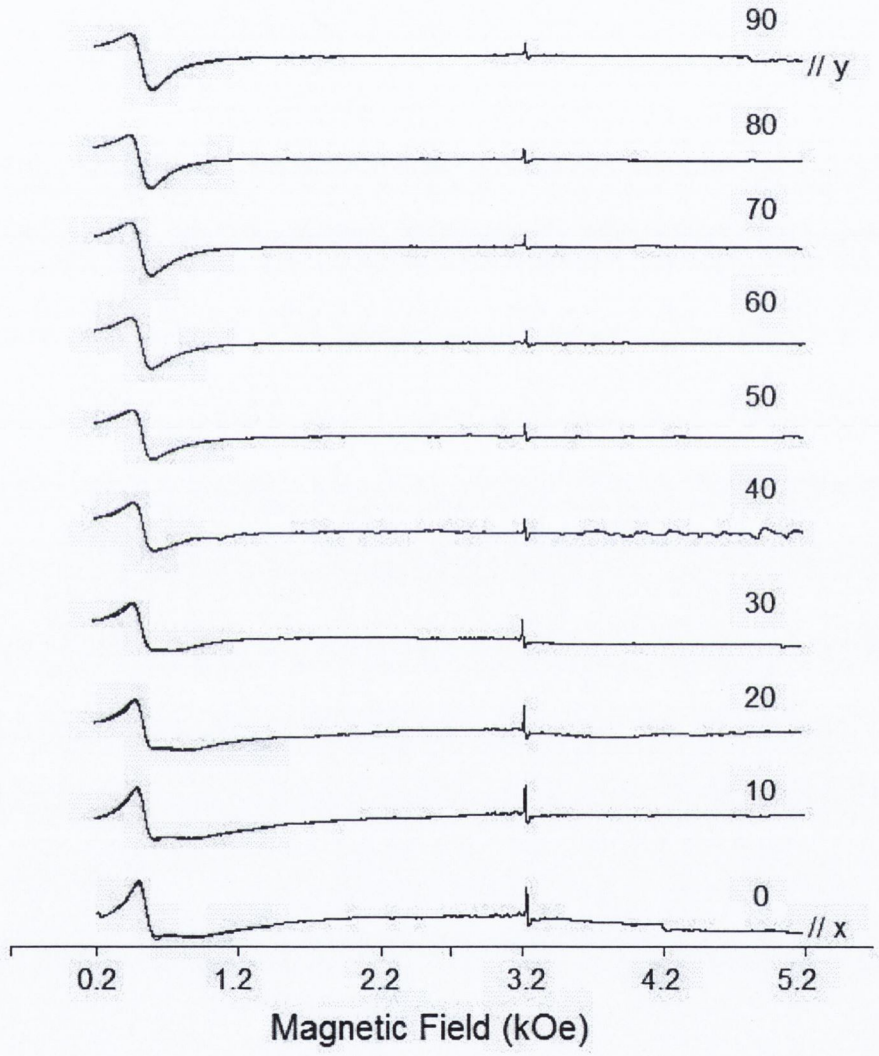

Figure 7.5: FMR spectra as a function of the direction of $\vec{H}$ within the x-y plane. Spectra are labeled with the ϕ_H value, as shown in Figure 7.4. The sharp line is from the MgO:F^+ field marker.

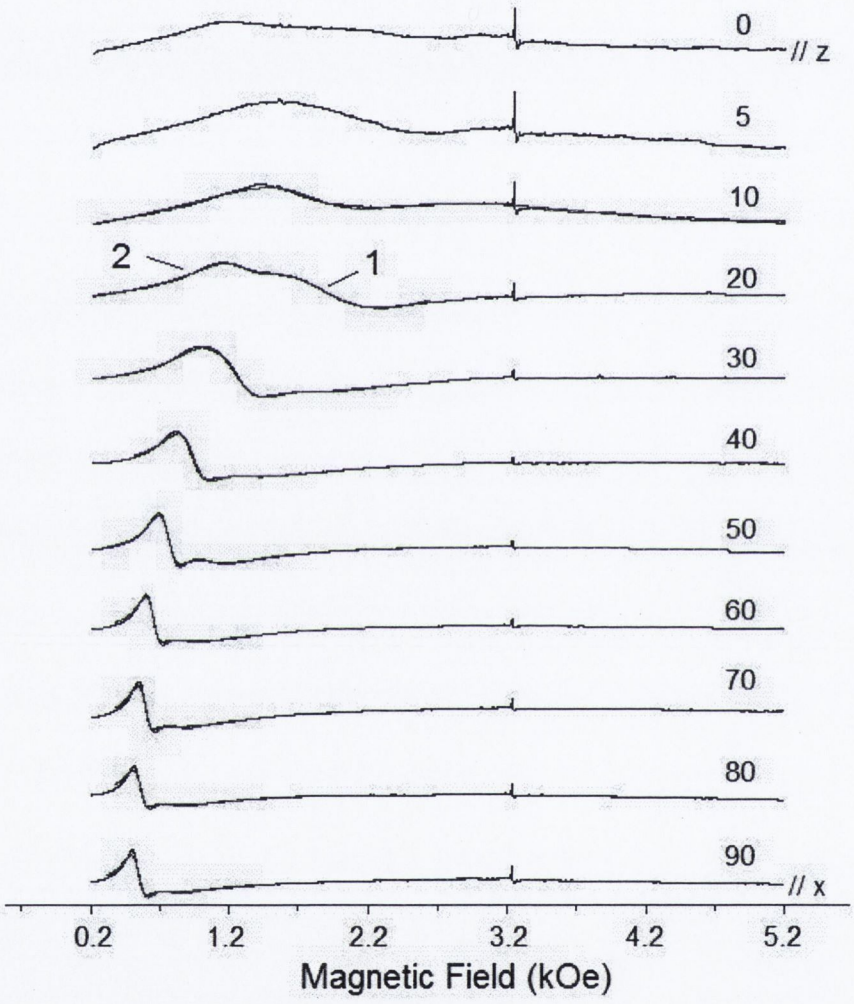

Figure 7.6: FMR spectra as a function of the direction of $\vec{H}$ within the x-z plane. Two lines, 1 and 2, are apparent in this case. Spectra are labeled with the θ_H value, as shown in Figure 7.4. The sharp line is from the MgO:F^+ field marker.

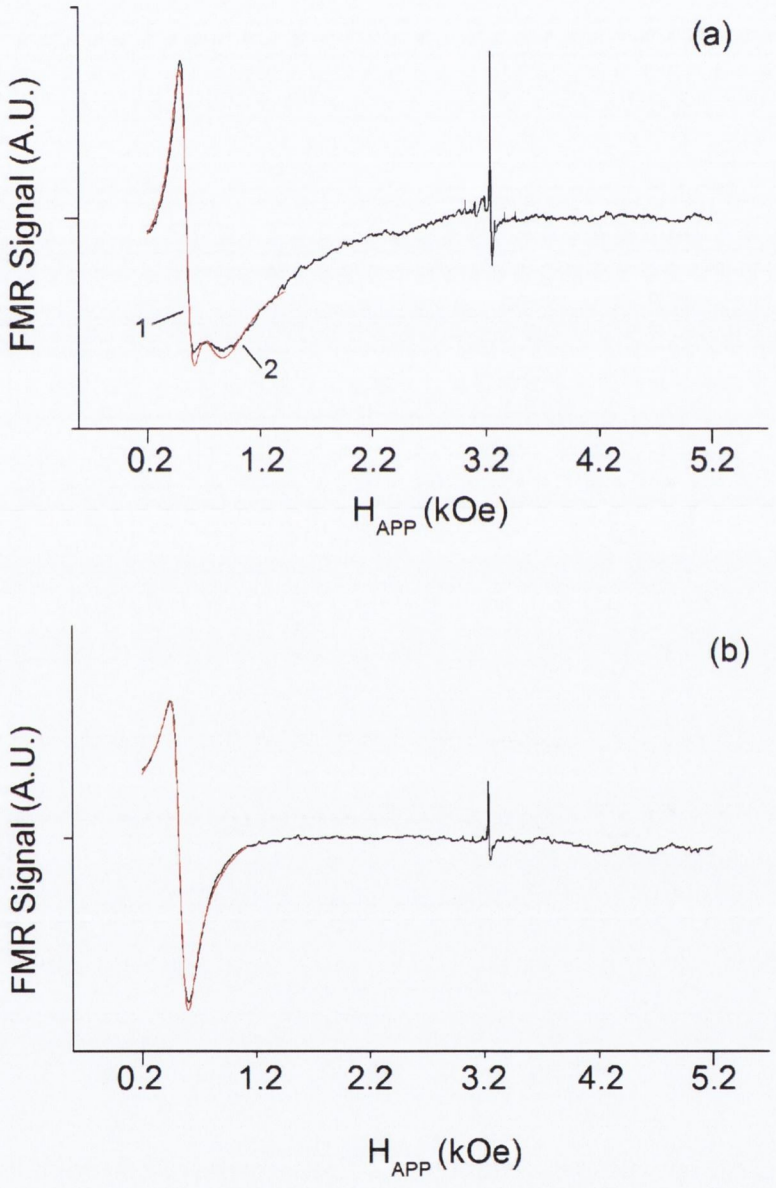

Figure 7.7: Spectra taken on sample S-1 while rotating in the x-y plane. Spectrum (a) was recorded with $\phi_H = 10°$, while spectrum (b) was recorded with $\phi_H = 80°$. The black lines show raw experimental data, while the red lines show the fits of the resonance line to a combination of two Lorentzian derivative lines.

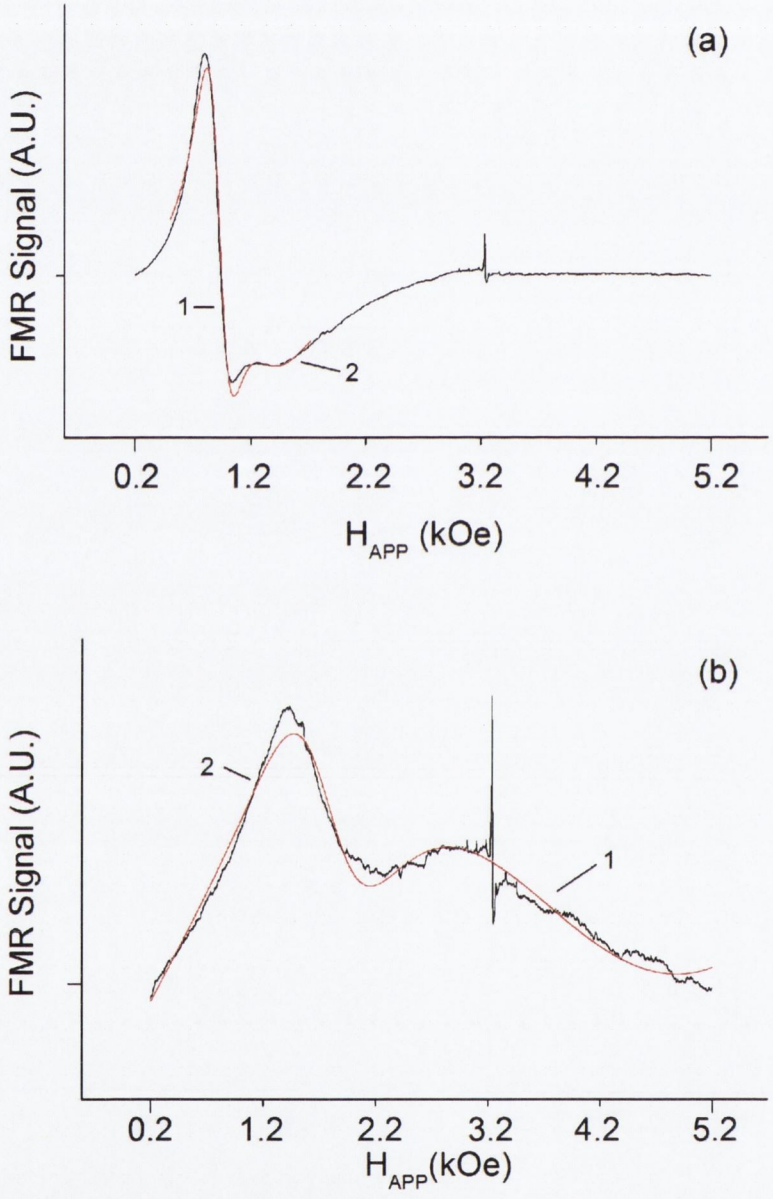

Figure 7.8: Spectra taken on sample S-1 while rotating in the x-z plane. Spectrum (a) was recorded with $\theta_H = 60°$, while spectrum (b) was recorded with $\theta_H = 10°$. The black lines show raw experimental data, while the red lines show the fits of the resonance line to a combination of two Lorentzian derivative lines.

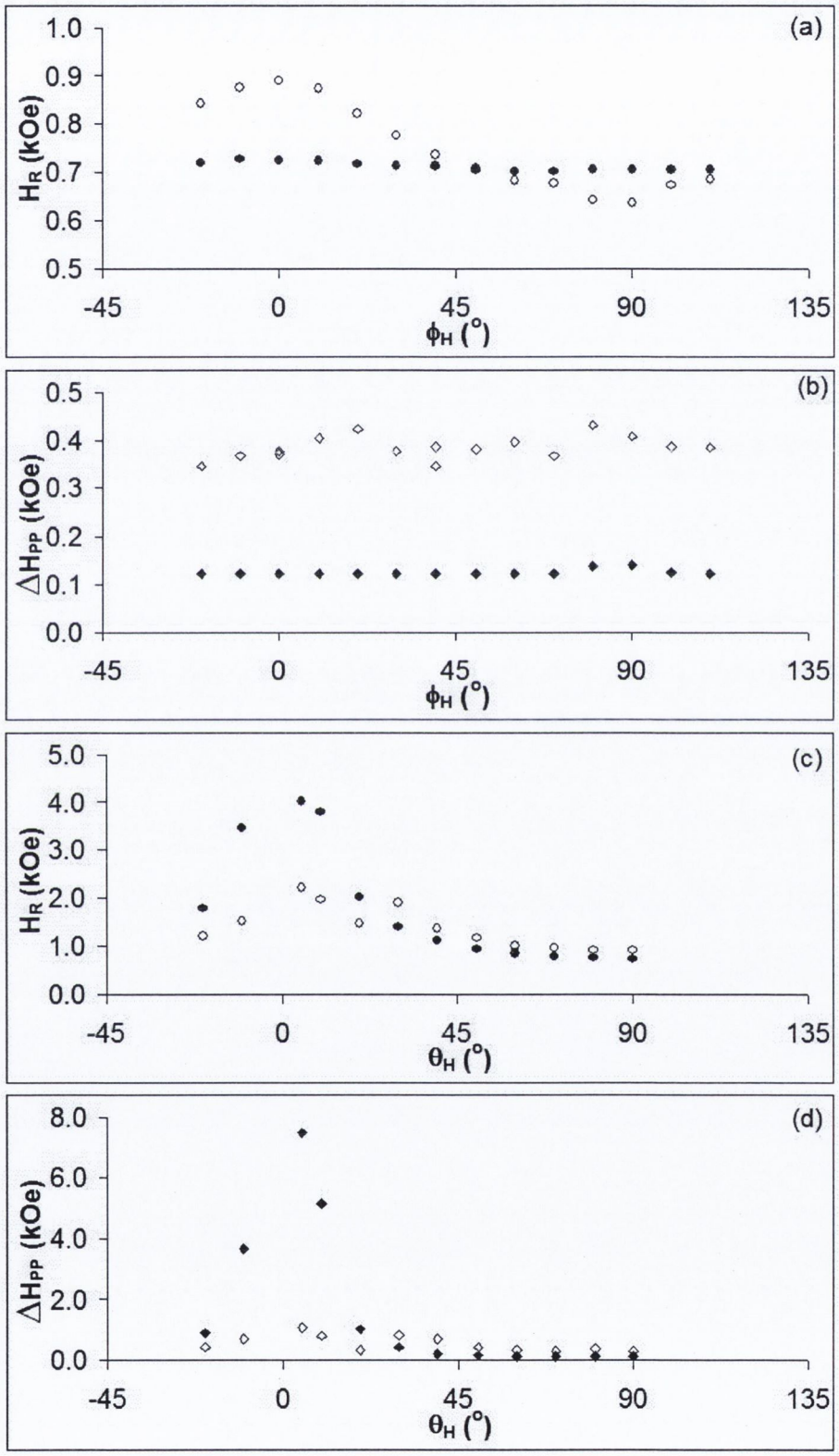

Figure 7.9: Resonance field and linewidth for lines 1 (•) and 2 (◇) in sample S-1 for rotation of $\vec{H}$ in plane x-y ((a) and (b)) and x-z((c) and (d))

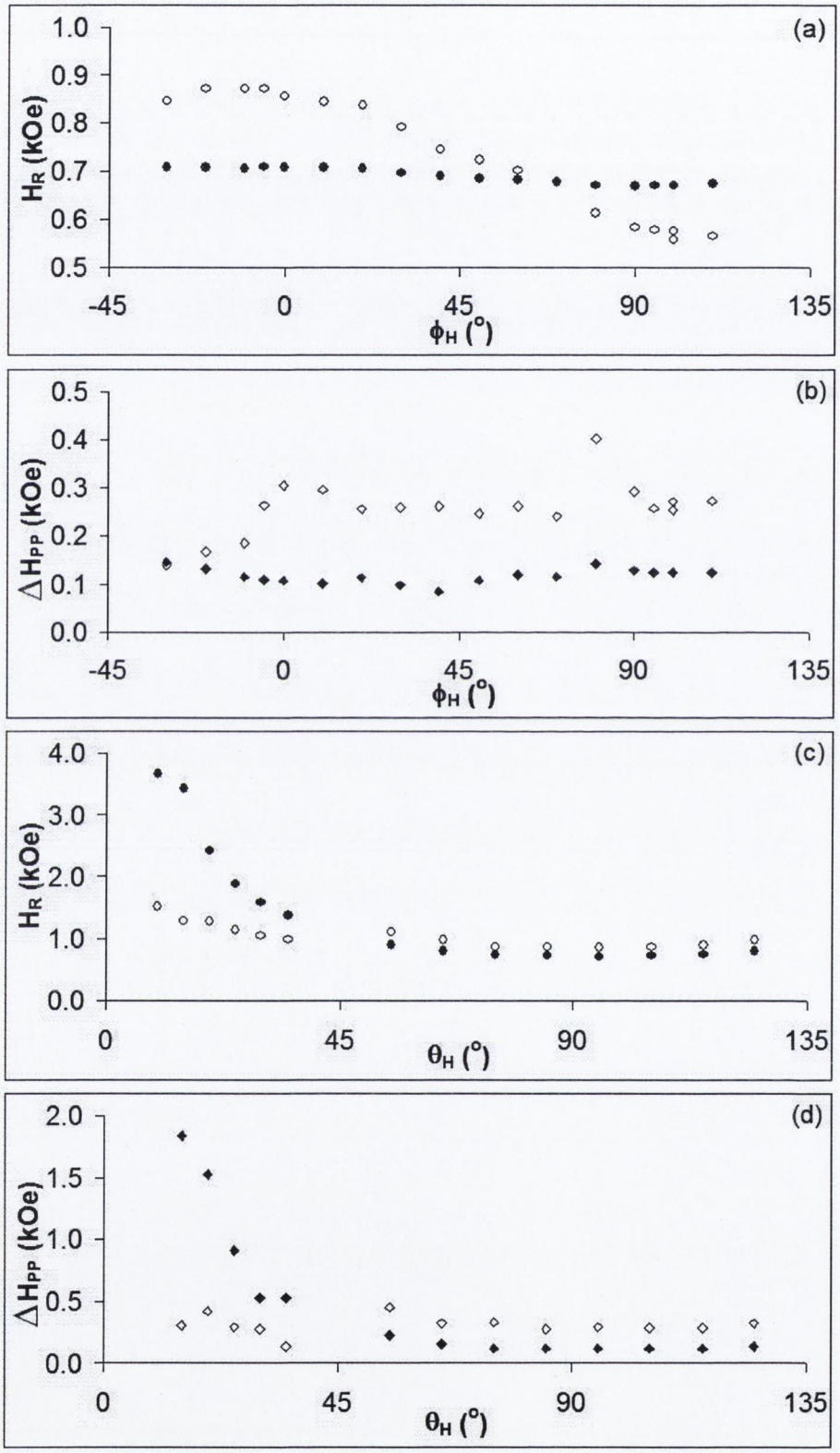

Figure 7.10: Resonance field and linewidth for lines 1 (•) and 2 (◇) in sample S-2 for rotation of $\vec{H}$ in plane x-y ((a) and (b)) and x-z((c) and (d))

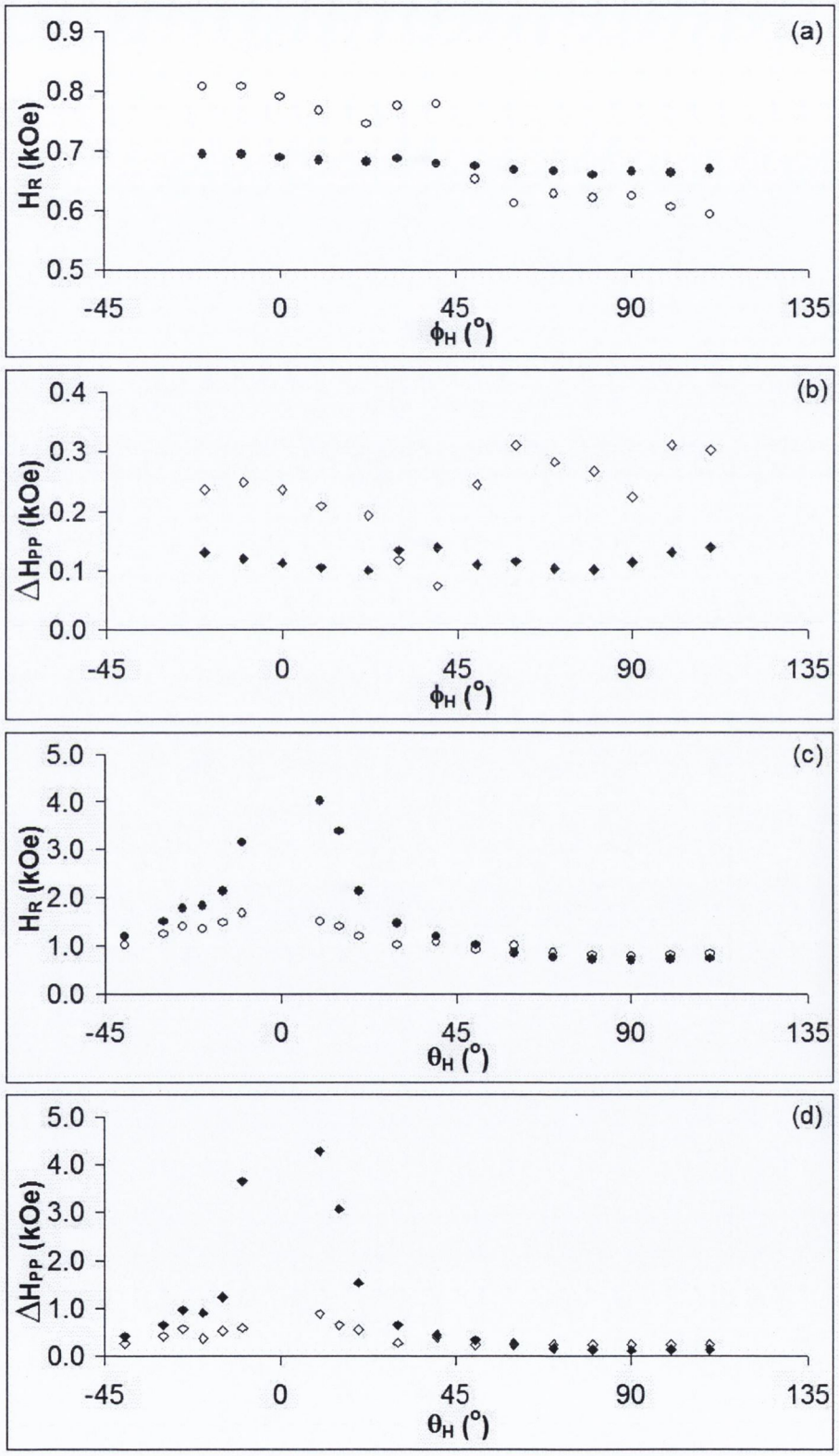

Figure 7.11: Resonance field and linewidth for lines 1 (•) and 2 (◇) in sample S-3 for rotation of $\vec{H}$ in plane x-y ((a) and (b)) and x-z((c) and (d))

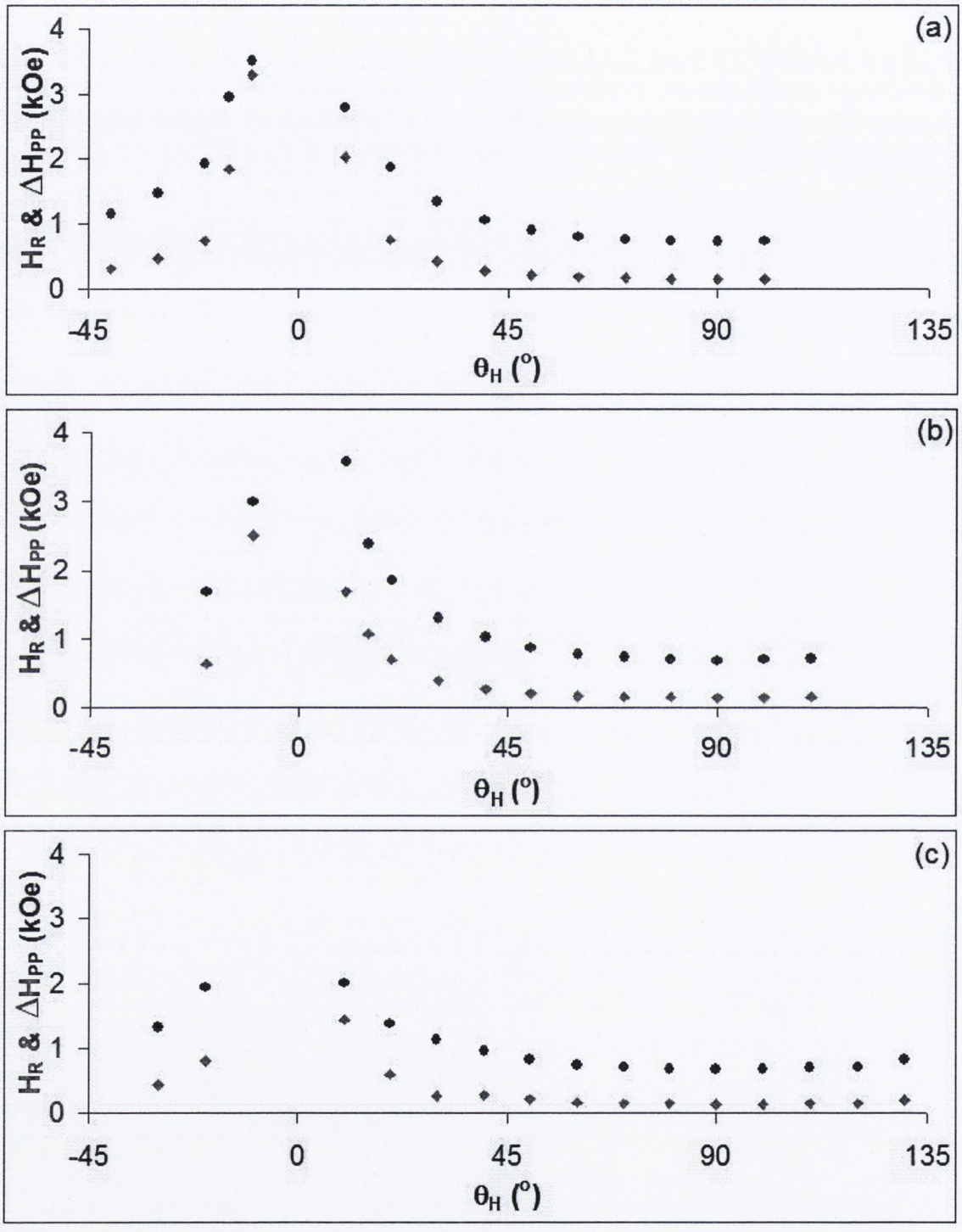

Figure 7.12: Angular dependence of H_R (•) and ΔH_{PP} (grey symbols) observed while varying the direction of $\vec{H}$ in the y-z plane. Figures (a), (b) and (c) show the angular dependencies for samples S-1, S-2 and S-3 respectively.

7.3.2 Field Rotation Within the y-z Plane

Figure 7.12 shows the dependence of the resonance field and peak-to-peak linewidth as a function of the field direction within the y-z plane. Only line 1 is present when the measurements were made several weeks after the nanowire deposition. It is clear that the results for all samples are very similar and that they are consistent with what was observed for field rotation in the x-y and x-z planes. The figure also clearly shows how the change in ΔH_{PP} follows that in H_R. As before it was not possible to measure H_R and ΔH_{PP} for $\theta_H \leq 8°$.

7.4 Analysis and Discussion

We will limit the analysis to that of line 1. Since the line exhibits axial symmetry about the z-axis, the direction in the film plane perpendicular to the wires, we will seek to fit its angular dependence to a model in which the energy density is given by

$$E = -\vec{M}.\vec{H} + K_Z \sin^2\theta \tag{7.1}$$

where the first term is the Zeeman energy and the second term represents a uniaxial energy term with axis parallel to z; θ is the angle between $\vec{M}$ and the z-axis. In view of the fact that the z-axis is a hard axis, we expect the fit to yield a K_Z value that is negative. If the fit is good then we will consider the significance of this.

With respect to polar coordinates (as given in Figure 7.4) equation 7.1 becomes

$$E = -MH[\sin\theta \sin\theta_H \cos(\phi - \phi_H) + \cos\theta \cos\theta_H] + \frac{1}{2}MH_Z \sin^2\theta \tag{7.2}$$

where, by definition, $H_Z = 2K_Z/M$.

The Smit and Beljers expression for the resonance condition (ignoring damping)

$$\left(\frac{\omega}{\gamma}\right)^2 = \left(\frac{1}{M\sin^2\theta}\frac{\partial^2 E}{\partial\theta^2}\right) \times \left(\frac{1}{M}\frac{\partial^2 E}{\partial\phi^2}\right) - \left(\frac{1}{M\sin\theta}\frac{\partial^2 E}{\partial\theta\partial\phi}\right)^2 \tag{7.3}$$

and the condition for the equilibrium position of $\vec{M}$ that $\partial E/\partial\theta = \partial E/\partial\phi = 0$ give

$$\left(\frac{\omega}{\gamma}\right)^2 = [H_Z \cos 2\theta + H\cos(\theta - \theta_H)] \times \left[H_Z \cos^2\theta + H\cos(\theta - \theta_H)\right] \quad (7.4)$$

$$0 = \frac{1}{2}H_Z \sin 2\theta + H\sin(\theta - \theta_H) \quad (7.5)$$

for rotation in both the x-z plane ($\phi = \phi_H = 0°$) and in the y-z plane ($\phi = \phi_H = 90°$).

For rotation in the x-y plane ($\theta = \theta_H = 90°$) the corresponding equations are

$$\left(\frac{\omega}{\gamma}\right)^2 = [H\cos(\phi - \phi_H)] \times [H\cos(\phi - \phi_H) - H_{EZ}] \quad (7.6)$$

$$0 = H\sin(\phi - \phi_H) \rightarrow \phi = \phi_H \quad (7.7)$$

Equations 7.6 and 7.7 imply that, for $\vec{H}$ within the x-y plane, at constant ω the resonance field is also constant and is given by

$$\left(\frac{\omega}{\gamma}\right)^2 = H\,(H - H_Z) \quad (7.8)$$

For samples S-1, S-2 and S-3 the measured values of resonance field and (for g = 2) the values of $(\omega/\gamma)^2$ are 0.70 ± 0.03 kOe, 0.69 ± 0.02 kOe, 0.68 ± 0.02 kOe and 11.6 kOe^2, 11.7 kOe^2 and 11.7 kOe^2 and hence equation 7.6 gives values for H_Z of 15.9 ± 0.7 kOe, 16.3 ± 0.5 kOe and 16.5 ± 0.5 kOe.

To obtain the best fit of the angular dependence of resonance field within the x-y and x-z planes we perform iteration of a calculation using equations 7.4 and 7.5. For a given value of H_Z, we began with by substituting the experimentally observed values for H into equation 7.5, which gave us an estimate of $\theta - \theta_H$. We then used this estimate to extract a value of H from equation 7.4, which we used as the starting value for the next iteration. We continued this process until we obtained a value of H for which equations 7.4 and 7.5 were mutually consistent. We then repeated this for different values of H_Z, seeking the value which gave us the best least-squares fit to the experimental data. These values and fits are those displayed in Table 7.2 and Figures 7.13, 7.14 and 7.15.

Figure 7.13 shows that, for sample S-1 good fits to the data are obtained with val-

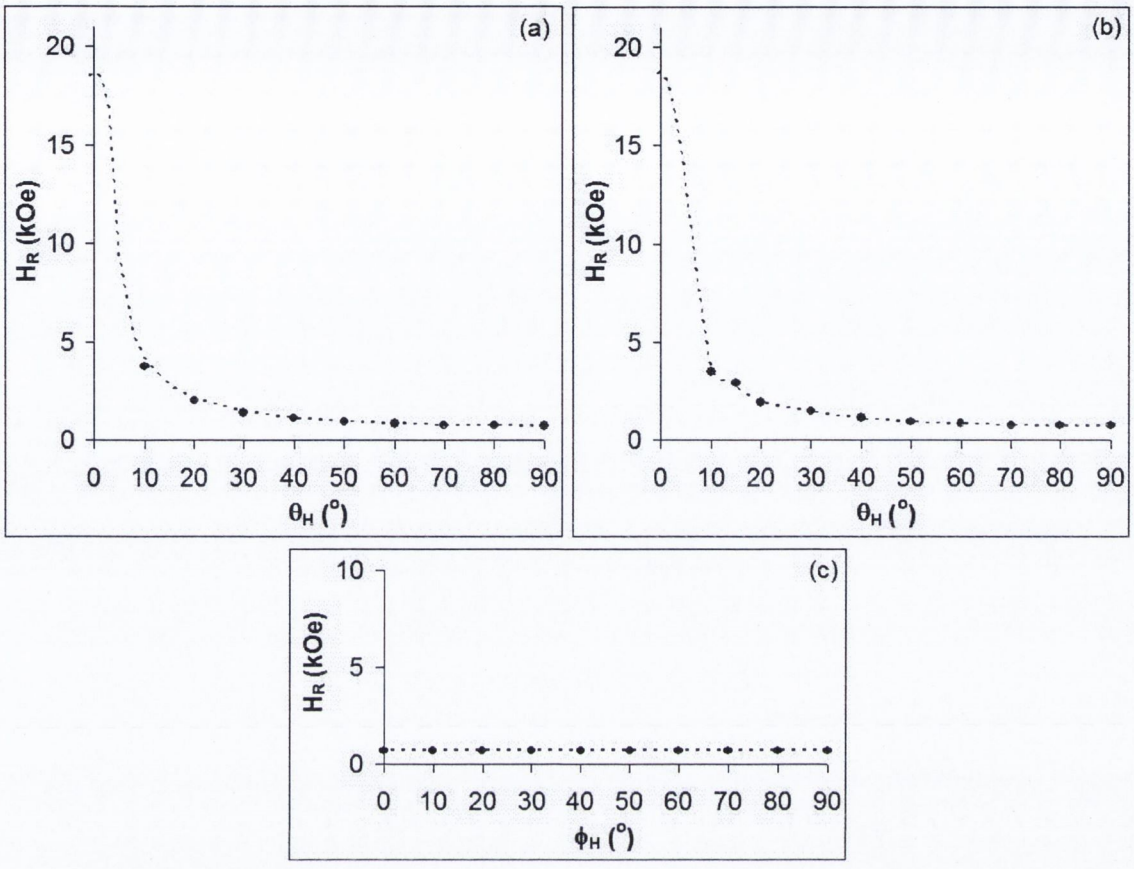

Figure 7.13: Fits of the angular dependence of H_R for S-1 to the theoretical model, using equations 7.4, 7.5, 7.6 and 7.7. The figures show the angular dependence as $\vec{H}$ is rotated (a) in the y-z plane, (b) in the x-z plane, and (c) in the x-y plane. Parameters used for the fits are given in table 7.2.

ues of H_Z given in Table 7.2. Figures 7.14 and 7.14 show that equally good fits are obtained for samples S-2 and S-3. It is clear from Table 7.2 that there is no significant difference between all the H_Z values; within error all plots can be fitted with a single value of H_Z = -16.1 ± 0.4 kOe. Figures 7.13, 7.14 and 7.15 show that below $\theta_H \approx 10°$ the resonance field is predicted to increase rapidly reaching a value of (ω/γ) - $H_Z \approx$ 19.3 kOe at $\theta_H = 0$. Unfortunately it was not possible to even follow the resonance to the magnet upper limit ($\approx$ 7 kOe) because before that the line had broadened so much it became indeterminate.

The above analysis has shown that the angular dependence of the resonance field can be accounted for by only one uniaxial term, $1/2(MH_Z\sin^2\theta)$, for the energy density in addition to the Zeeman energy and that its axis is in the plane of, and perpendicular to, the nanowires.

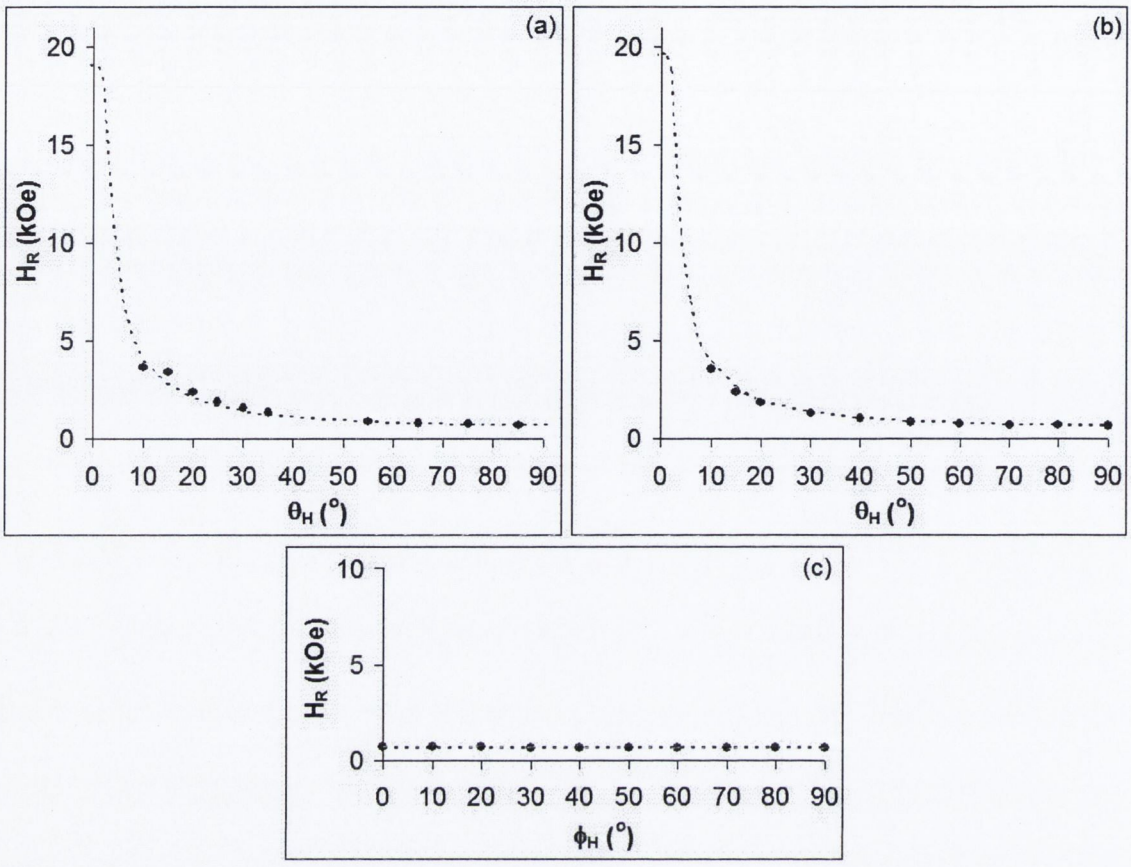

Figure 7.14: Fits of the angular dependence of H_R for S-2 to the theoretical model, using equations 7.4, 7.5, 7.6 and 7.7. The figures show the angular dependence as $\vec{H}$ is rotated (a) in the y-z plane, (b) in the x-z plane, and (c) in the x-y plane. Parameters used for the fits are given in table 7.2.

We now consider how this compares with what has been found for other nanowire arrays. We are not aware of any published FMR studies of nanowires deposited on vicinal substrates but there are several [29–34] of nanowires created in porous membranes. For Ni nanowires in polycarbonate membranes [29,30] and in alumina membranes [31], the angular dependence of the resonance field was described by the equation

$$\left(\frac{\omega}{\gamma}\right)^2 = [H_{EF}\cos 2\theta + H\cos(\theta - \theta_H)] \times [H_{EF}\cos^2\theta + H\cos(\theta - \theta_H)] \qquad (7.9)$$

derived from an energy density given by

$$E = \frac{1}{2}MH_EF\sin^2\theta - \vec{M}.\vec{H} \qquad (7.10)$$

These equations have exactly the same form as the equations 7.4 and 7.6 but with

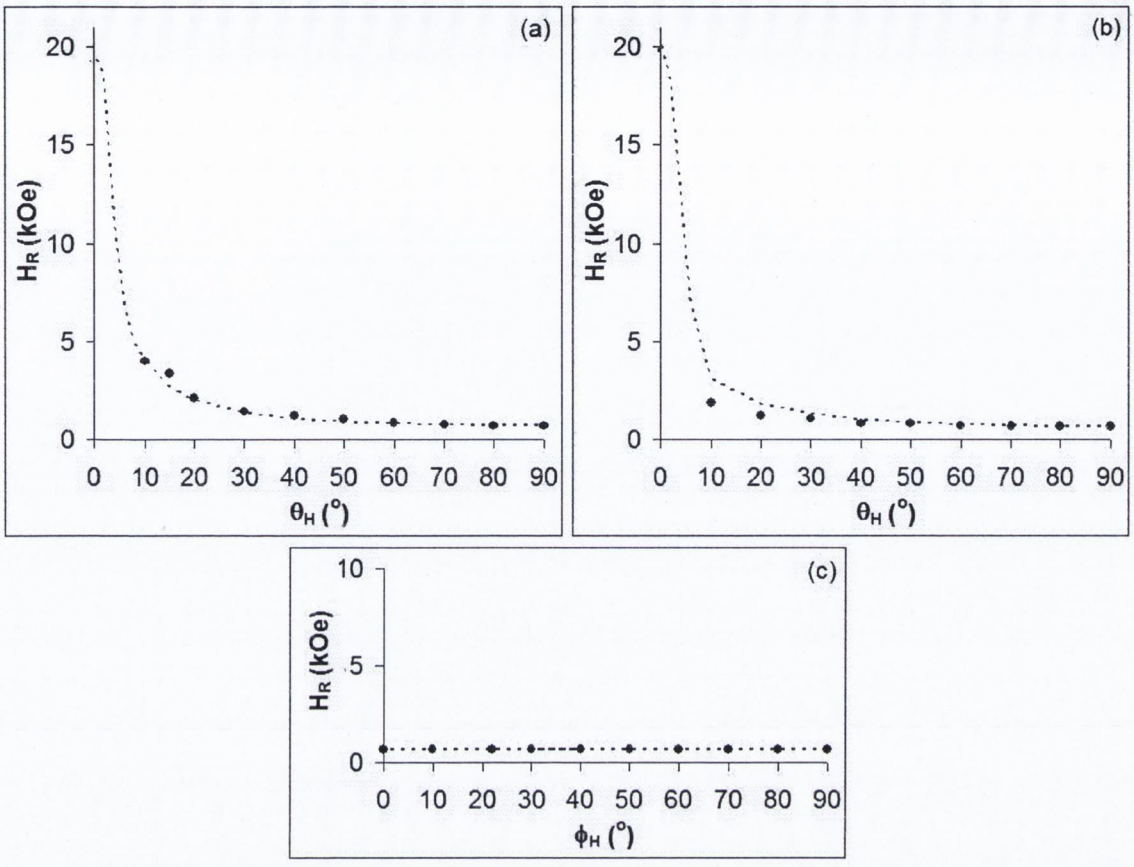

Figure 7.15: Fits of the angular dependence of H_R for S-3 to the theoretical model, using equations 7.4, 7.5, 7.6 and 7.7. The figures show the angular dependence as $\vec{H}$ is rotated (a) in the y-z plane, (b) in the x-z plane, and (c) in the x-y plane. Parameters used for the fits are given in table 7.2.

the major difference that θ, θ_H are the angles between the equilibrium directions of $\vec{M}$, $\vec{H}$ and the *axis of the nanotubes.*

Encinas-Oropesa et.al [30] found that their results were consistent with the phenomenological expression

$$H_{EF} = 2\pi M_S(1 - 3P) \tag{7.11}$$

where M_S is the saturation magnetisation and P the porosity (0 - 1) of the polycarbonate membrane. Carignan et. al. [31] used an effective field model to derive this expression for the case of nanowire length, L >> interwire distance, D. The first term comes from the shape magnetisation energy density, $\pi M_S^2 \sin^2\theta$, and the second from the dipolar interaction between the wires. These equations imply that for P<1/3 the easy axis is parallel to the wires and the angular dependence of the spectra has an axial symmetry about this axis; this is observed in [29–32]. However

Table 7.2: The parameter used in fitting the observed angular dependencies of H_R to equations 7.4, 7.5, 7.6 and 7.7, shown in Figures 7.13, 7.14 and 7.15.

Sample	H_{EZ} x-y rotation	H_{EZ} x-z rotation	H_{EZ} y-z rotation
S-6	-15.9 kOe	-15.4 kOe	-15.5 kOe
S-8	-16.3 kOe	-15.8 kOe	-16.3 kOe
S-11	-16.5 kOe	-16.1 kOe	-16.8 kOe

for P>1/3, H_{EF} is negative and the sample plane (perpendicular to the wires) corresponds to an easy plane [31,32]. This is to be expected since, for close packing, the nanowire array becomes almost equivalent to a thin film (with plane perpendicular to the wires) for which the shape anisotropy implies that the film is an easy plane.

For parallel nanowires all lying within one plane, as in our samples, one might expect that there would be an easy axis parallel to the wires. Studies on an array of Fe nanowires of width ≈150nm and periodicity of 300nm showed this result [90]; magneto-optical Kerr effect (MOKE) measurements on a nanowire array produced by patterning a thin Fe film by means of optical interference lithography found the easy axis of magnetisation to be parallel to the wires. Another study on Fe nanowire arrays produced by deposition on trenched templates [91] also found the easy axis to be in plane and along the axis of the wires - in this case wires had mean thickness and width 1nm and 7nm respectively.

For our wires, as the separation is much less than their length, it would be expected that the dipolar interactions are significant but only within the plane containing the wires. One might therefore expect the situation to approach that of a continuous thin film and that, as seen in [31,32], this would be an easy plane; this of course is not what is observed. However, the substrate is a vicinal surface, and so the film might nearly resemble the stepped plane as discussed in the previous chapter. There have been several studies [78–80] of Fe films on vicinal surfaces that show the existence of a uniaxial anisotropy associated with the steps. Both Kawakami et. al. [79] and Wu et.al. [78] found that for Fe on vicinal Ag(100) the easy axis was parallel to the step edges whereas Leeb et. al. [80] found that it could be in plane but perpendicular to the step edges in thin enough films. An easy axis parallel to the step edges of course implies that the in-plane direction perpendicular to the step edges is a hard axis, as we observe. It may be therefore that it is the interaction of the wires with the steps that gives rise to a hard axis in plane and perpendicular to the steps. As mentioned in section 6.5.1, previous studies undertaken on Fe_3O_4 films by Krug et.al [89] and Lu et. al. [88] found that magnetic anisotropies could be

induced due to interactions at the substrate-film interface, and so we suggest that this type of effect is also present here.

This, however, does not explain why the direction parallel to the wires and perpendicular to the wires but out of plane are equivalent, or nearly so, easy axes. Before attempting more detailed analysis it is surely worth extending the FMR measurements to nanowires of more uniform width and with several different uniform spacings, all on vicinal substrates.

7.5 Conclusions

Fe nanowire arrays deposited on vicinal sapphire substrates using the ATLAS procedure were found to exhibit a uniaxial anisotropy with axis within the plane of the array, but perpendicular to the wires(this axis being a hard axis of magnetisation). The angular dependence of H_R can be fit well to a model including only the Zeeman interaction and a single anisotropy field, directed along this axis. The magnitude of the anisotropy field, H_Z, was found to be -16.1 $\pm$ 0.4 kOe for all samples investigated, despite difference in wire width and spacing. It is likely that this effect is caused by the step edges at the substrate-iron interface, and we suggest that further study is necessary.

Chapter 8

Conclusions

In this thesis we have presented the results of FMR studies on thin magnetite films and iron nanowires. We examined three sets of magnetite (Fe_3O_4) films. The first aims of this study were to examine how the magnetic anisotropy of thin magnetite films is affected by the film thickness, and the deposition substrate; to examine how post-deposition annealing affects the film's magnetic anisotropy, and also to examine whether the deposition substrate had any impact on this; and to see whether depositing magnetite on a stepped substrate would induce a uniaxial anisotropy, and to examine whether this anisotropy was affected by the film thickness or miscut angle.

In order to achieve these aims, we examined a number of different types of samples. The first set examined consisted of five films of different thicknesses in the range 5nm to 700nm, deposited on flat MgO and $MgAl_2O_4$ substrates. The second set of samples studied consisted of six films, again deposited on flat MgO and $MgAl_2O_4$ substrates but all of 100nm thickness, which were annealed in air after deposition for periods between 4 and 160min. The third set of samples consisted of five films, of thickness between 30 and 70nm, deposited on substrates of MgO miscut by between 3 and 10 degrees. We will now give a summary of the results of these studies, and the conclusions reached.

In the study of films with varying thickness, we found that Fe_3O_4 films deposited on MgO show a decrease in cubic anisotropy with an increase in film thickness, with the cubic anisotropy field $H_{4||}$ decreasing from –315 Oe to –75 Oe with an increase in film thickness from 38 to 700nm. We propose that the decrease in cubic anisotropy is due to a decrease in film quality with increase in thickness, as is evidenced by an increase in the mean linewidth.

The Fe_3O_4 films from the same set which were deposited on $MgAl_2O_4$ showed the remarkable property of having their easy axis orientated along [100] type direction, as opposed to the [110] type directions expected. It is not clear what could cause this change. The cubic anisotropy in this case increased with an increase in the film thickness, with the cubic anisotropy field $H_{4||}$ increasing from 85 Oe to 168 Oe with an increase in film thickness from 5nm to 33nm. Again, we propose that the film exhibiting higher cubic anisotropy is of better quality, as is shown by the quality of the FMR signal observed.
High frequency measurements gave a g-value of 2.03 for the films, lower than the bulk value of 2.12 [38], and the value of 2.14 observed by Atkas [9]. This is further supported by fits of the in-plane and out-of-plane angular dependencies of the resonance field to the theoretical model.

In the study of the films which were annealed after deposition, we found that the Fe_3O_4 films deposited on MgO showed an increase in cubic anisotropy after even a brief period of annealing (4min at 250°C in air), with the cubic anisotropy parameter $K_{4||}$ increasing from -1.5 kJ/m^3 to -5.1 kJ/m^3. The linewidth simultaneously decreases, with the mean (in-plane) value decreasing from 280 Oe to 210 Oe after the 4min anneal. However, annealing for a further 160min shows no further change in $K_{4||}$ and only a small further change in the mean in-plane linewidth, to 180 Oe. This mirrors the changes in magnetisation reported previously [19,20].
For the films in this set which were deposited on $MgAl_2O_4$, we again observed the unexpected property of the easy axis lying along [100] type direction. Unlike the behaviour of the magnetisation with annealing for the films on $MgAl_2O_4$ (which increases by 10% after 4 minutes annealing and no further with extended annealing time), $K_{4||}$ remains unchanged after 5 min annealing but increases from 1.7 kJ/m^3 to 6.1 kJ/m^3 after 160min. Similarly, the in-plane linewidth shows only a small change after 5 min annealing, but decreases significantly after 160 minutes of annealing.
These results support the suggestion by Yang et.al [19,20] that the APB structure in the films on MgO can be significantly altered by even a rather gentle air anneal. Our results suggest that more extensive annealing is required to improve the quality of films on $MgAl_2O_4$.

In the study of films deposited on vicinal substrates, we found that Fe_3O_4 films on vicinal MgO(100) with step edges parallel to $[0\bar{1}1]$ have an in-plane uniaxial anisotropy with easy axis perpendicular to the step edge. The strength of this anisotropy varies approximately quadratically with the vicinal angle. As regards its

dependence on film thickness, d, it can be represented by the sum of two terms, one of which is independent of d and the other one proportional to 1/d. The latter is associated with an anisotropy localized at the interface, most likely at the steps, and the first may be associated with APBs preferentially aligned with the step edges. A second, weaker, in-plane uniaxial anisotropy is present in the film on the 10° miscut substrate, which we attribute to an uneven step edge configuration. The FMR linewidth also exhibits an in-plane anisotropy that increases in magnitude as the vicinal angle increases but is almost independent of thickness, in the range 30-70nm, of films on the 2° miscut substrate.

The final aim of the studies presented here was to characterise the magnetic anisotropy of arrays of Fe nanowires deposited on stepped sapphire substrates. In order to do this, we examined three nanowire arrays, produced by the ATLAS method [24,36]. We found the arrays exhibited a uniaxial anisotropy with axis within the plane of the array, but perpendicular to the wires – this axis being is a hard axis of magnetisation. The angular dependence of H_R can be fit well to a model including only the Zeeman interaction and a single anisotropy field, directed along this axis. The magnitude of the anisotropy field, H_Z, was found to be -16.1 $\pm$ 0.4 kOe for all samples investigated, despite differences in wire width and spacing. We suggest that this effect is caused by the step edges at the substrate-iron interface, although further study is necessary.

Bibliography

[1] H. Katayama-Yoshida and K. Sato. Spin and charge control method of ternary II-VI and III-V magnetic semiconductors for spintronics: theory vs. experiment. *J. Phys. Chem. Solids*, 64:1447 – 1452, 2003. 13th International Conference on Ternary and Multinary Compounds.

[2] S. Sugahara and M. Tanaka. Tunneling magnetoresistance in fully epitaxial MnAs/AlAs/MnAs ferromagnetic tunnel junctions grown on vicinal GaAs (111) b substrates. *Appl. Phys. Lett*, 80:1969, 2002.

[3] T. Bland and K. Lee. The spintronics challenge. *Physics World*, January, 2008.

[4] A. A. Tulapurkar, Y. Suzuki, A. Fukushima, H. Kubota, H. Maehara, K. Tsunekawa, D. D. Djayaprawira, N. Watanabe, and S. Yuasa. Spin-torque diode effect in magnetic tunnel junctions. *Nature*, 438:339, 2005.

[5] R. L. Comstock and E. B. Moore. Ferrite film recording surfaces for disk recording. *IBM J. Res. Develop.*, 1974.

[6] R. L. Comstock and Mason L. Williams. Frequency response in digital magnetic recording. *IEEE Trans. Magn.*, MAG-9:342, 1973.

[7] W. Kim, K. Kawaguchi, N. Koshizaki, M. Sohma, and T. Matsumoto. Fabrication and magnetoresistance of tunnel junctions using half-metallic FeO. *J. Appl. Phys*, 93:8032, 2003.

[8] H. Matsuda, S. Okamura, T. Shiosaki, H. Adachi, and H. Sakakima. Magnetic and magnetoresistance properties of spin valves using epitaxial Fe_3O_4 (110) as the pinning layer. *J. Appl. Phys*, 98:063903, 2005.

[9] B. Atkas. Fmr properties of epitaxial Fe_3O_4 films on MgO(100). *Thin Solid Films*, 307:250–259, 1997.

[10] D. T. Margulies, F. T. Parker, F. E. Spada, R. S. Goldman, J. Li, R. Sinclair, and A. E. Berkowitz. Anomalous moment and anisotropy behavior in Fe_3O_4 films. *Phys. Rev. B*, 53:9175–9187, 1996.

[11] K Balakrishnan, S K Arora, and I V Shvets. Strain relaxation studies of the Fe_3O_4/MgO (100) heteroepitaxial system grown by magnetron sputtering. *J. Phys. Cond. Matter*, 16:5387–5393, 2004.

[12] Sangeeta Kale, S. M. Bhagat, S. E. Lofland, T. Scabarozi, S. B. Ogale, A. Orozco, S. R. Shinde, T. Venkatesan, B. Hannoyer, B. Mercey, and W. Prellier. Film thickness and temperature dependence of the magnetic properties of pulsed-laser-deposited Fe_3O_4 films on different substrates. *Phys. Rev. B*, 64:205413, 2001.

[13] P. A. A. van der Heijden, M. G. van Opstal, C. H. W. Swüste, P. H. J. Bloemen, J. M. Gaines, and W. J. M. de Jonge. A ferromagnetic resonance study on ultrathin Fe_3O_4 layers grown on (001) MgO. *J. of Magn. Magn. Mat.*, 182:71–80, 1998.

[14] F. C. Voogt, T. Fujii, P. J. M. Smulders, L. Niesen, M. A. James, and T. Hibma. NO_2-assisted molecular-beam epitaxy of Fe_3O_4, $Fe_{3-\delta}O_4$, and γ-Fe_2O_3 thin films on MgO (100). *Phys. Rev. B*, 60:11193–11206, 1999.

[15] W. F. J. Fontijn, P. A. A. van der Heijden, F. C. Voogt, T. Hibma, and P. J. van der Zaag. Comparison of a stoichiometric analysis of $Fe_{3-\delta}O_4$ layers by magneto-optical kerr spectroscopy with mossbauer results. *J. Magn. Magn. Mat.*, 165:401–404, 1997.

[16] S. K. Arora, R. G. S. Sofin, and I. V. Shvets. Magnetoresistance enhancement in epitaxial magnetite films grown on vicinal substrates. *Phys. Rev. B*, 72:134404, 2005.

[17] S. K. Arora, R. G. S. Sofin, I. V. Shvets, R. Kumar, M. Wasi Khan, and J. P. Srivastava. Influence of antiphase boundary density on the conduction noise properties of epitaxial magnetite thin films. *J. Appl. Phys.*, 97:10C310, 2005.

[18] S. K. Arora, R. G. S. Sofin, I. V. Shvets, and M. Luysberg. Anomalous strain relaxation behavior of Fe_3O_4/MgO (100) heteroepitaxial system grown using molecular beam epitaxy. *J. Appl. Phys.*, 100:073908, 2006.

[19] Y. Zhou, X. Jin, and I. V. Shvets. Enhancement of the magnetization saturation in magnetite (100) epitaxial films by thermo-chemical treatment. *J. Appl. Phys.*, 95:7357, 2004.

[20] Y. Zhou, X. Jin, and I. V. Shvets. Effect of thermo-chemical treatment on magnetic and spin-transport properties of epitaxial Fe_3O_4(100)/MgO films. *J. Magn. Magn. Mat.*, 286:346, 2005.

[21] Y. Zhou, C. McEvoy, and I. V. Shvets. The magnetic and magnetoresistance properties of ultrathin magnetite films grown on MgO substrate. *J. Magn. Magn. Mat.*, 290-291:1033, 2005.

[22] W. Eerenstein, T. Hibma, and S. Celotto. Mechanism for superparamagnetic behavior in epitaxial Fe_3O_4 films. *Phys. Rev. B*, 70:184404, 2004.

[23] D. T. Margulies, F. T. Parker, M. L. Rudee, F. E. Spada, J. N. Chapman, P. R. Aitchison, and A. E. Berkowitz. Origin of the anomalous magnetic behavior in single crystal Fe_3O_4 films. *Phys. Rev. Lett.*, 79:5162–5165, 1997.

[24] I. V. Shvets, H. C. Wu, V. Usov, F. Cuccureddu, S. K. Arora, and S. Murphy. Concept of a nanowire array magnetoresistance device. *Appl. Phys. Lett.*, 92:023107, 2008.

[25] H. J. Elmers, J. Hauschild, and U. Gradmann. Morphology and magnetism of Fe on vicinal W (110) surfaces with different step orientation. *J. Magn. Magn. Mater.*, 221:219, 2000.

[26] J. Shen, R. Skomski, M. Klaua, H. Jenniches, S. Sundar Manoharan, and J. Kirschner. Magnetism in one dimension: Fe on Cu (111). *Phys. Rev. B*, 56:2340–2343, 1997.

[27] J. Shen, M. Klaua, P. Ohresser, H. Jenniches, J. Barthel, Ch. V. Mohan, and J. Kirschner. Structural and magnetic phase transitions of Fe on stepped Cu (111). *Phys. Rev. B*, 56:11134–11143, 1997.

[28] S. Shiraki, H. Fujisawa, M. Nantoh, and M. Kawai. Confining barriers for surface state electrons tailored by monatomic Fe rows on vicinal Au (111) surfaces. *Phys. Rev. Lett.*, 92:096102, 2004.

[29] U. Ebels, J. L. Duvail, P. E. Wigen, L. Piraux, L. D. Buda, and K. Ounadjela. Ferromagnetic resonance studies of Ni nanowire arrays. *Phys. Rev. B*, 64:144421, 2001.

[30] A. Encinas-Oropesa, M. Demand, L. Piraux, I. Huynen, and U. Ebels. Dipolar interactions in arrays of nickel nanowires studied by ferromagnetic resonance. *Phys. Rev. B*, 63:104415, 2001.

[31] L. P. Carignan, C. Lacroix, A. Ouimet, M. Ciureanu, A. Yelon, and D. Ménard. Magnetic anisotropy in arrays of Ni, CoFeB, and Ni/Cu nanowires. *J. of Appl. Phys.*, 102:023905, 2007.

[32] M. Pardavi-Horvath, P. E. Si, M. Vazquez, W. O. Rosa, and G. Badini. Interaction effects in permalloy nanowire systems. *J. Appl. Phys.*, 103:07D517, 2008.

[33] X. Kou, X. Fan, H. Zhu, and J. Q. Xiao. Tunable ferromagnetic resonance in NiFe nanowires with strong magnetostatic interaction. *Appl. Phys. Lett.*, 94:112509, 2009.

[34] L. P. Carignan, V. Boucher, T. Kodera, C. Caloz, A. Yelon, and D. Ménard. Double ferromagnetic resonance in nanowire arrays. *Appl. Phys. Lett.*, 95:062504, 2009.

[35] N. N. Negulyaev, V. S. Stepanyuk, W. Hergert, P. Bruno, and J. Kirschner. Atomic-scale self-organization of Fe nanostripes on stepped Cu(111) surfaces: Molecular dynamics and kinetic monte carlo simulations. *Phys. Rev. B*, 77:085430, 2008.

[36] F. Cuccureddu, V. Usov, S. Murphy, C. O. Coileain, and I. V. Shvets. Planar nanowire arrays formed by atomic-terrace low-angle shadowing. *Rev. Sci. Instr.*, 79:053907, 2008.

[37] F. Walz. The verwey transition-a topical review. *J. Phys.: Cond. Matter*, 14:R285, 2002.

[38] L. R. Bickford Jr. Ferromagnetic resonance absorption in magnetite single crystals. *Phys. Rev.*, 78:499–457, 1950.

[39] E.J.W. Verwey and P.W. Haayman. Electronic conductivity and transition point of magnetite. *Physica*, 9:979, 1941.

[40] F. C. Voogt, T. T. M. Palstra, L. Nielsen, O. C. Niesen, O. C. Rogojanu, M. A. James, and T. Hibma. Superparamagnetic behavior of structural domains in epitaxial ultrathin magnetite films. *Phys. Rev. B*, 57:R8107, 1998.

[41] S. Celotto, W. Erenstein, and T. Hibma. Characterization of anti-phase boundaries in epitaxial magnetite films. *Eur. Phys. J. B*, 36:271–279, 2003.

[42] W. Eerenstein, T. T. M. Palstra, T. Hibma, and S. Celotto. Diffusive motion of antiphase domain boundaries in Fe_3O_4 films. *Phys. Rev. B*, 68:014428, 2003.

[43] R. G. S. Sofin, S. K. Arora, and I. V. Shvets. Study of magnetoresistance of epitaxial magnetite films grown on vicinal MgO (100) substrate. *J. Appl. Phys.*, 97:10D3115, 2005.

[44] W. Eerenstein, T. T. M. Palstra, T. Hibma, and S. Celotto. Origin of the increased resistivity in epitaxial Fe_3O_4 films. *Phys. Rev. B*, 66:201101, 2002.

[45] G. A. Basset. *Phil. Mag.*, 3:1042, 1958.

[46] H. Bethge. Surface structures and crystal defects in electron microscopic pictures investigated on NaCl. *Phys. Status Solid.*, 2:775, 1962.

[47] J.-L. Lin, D. Y. Petrovykh, J. Viernow, F. K. Men, D. J. Seo, and F. J. Himpsel. Formation of regular step arrays on Si(111)77. *J. Appl. Phys.*, 84:255–260, 1998.

[48] J. Smit and H.G. Beljers. Ferromagnetic resonance absorption in $BaFe_{12}O_{19}$, a highly anisotropic crystal. *Philips Res. Rep.*, 10:113–130, 1955.

[49] A. Abragam and B. Bleaney. *Electron Paramagnetic Resonance of Transition Ions.* Clarendon Press, Oxford, 1970.

[50] G. E. Pake and T. L. Estle. *The Physical Principles of Electron Paramagnetic Resonance.* W.A Benjamin, Reading, 1973.

[51] L.D. Landau and E.M. Lifshitz. On the theory of the dispersion of magnetic permeability in ferromagnetic bodies. *Phys. Z. Sowietunion*, 8:153, 1935.

[52] T. L. Gilbert. A lagrangian formulation of gyromagnetic equation of the magnetization field. *Phys. Rev*, 100:1243, 1955. [Abstract only; full report, Armor Research Foundation Project No. A059, Supplementary Report, May 1, 1956] (unpublished).

[53] M. Farle. Ferromagnetic resonance of ultrathin metallic layers. *Rep. Prog. Phys.*, 61:755–826, 1998.

[54] M. Sparks. *Ferromagnetic Relaxation Theory.* McGraw Hill, New York, 1964.

[55] C. Kittel. On the theory of ferromagnetic resonance absorption. *Phys. Rev.*, 73:155–161, 1948.

[56] R. C. O'Handley. *Modern Magnetic Materials, Principles and Applications.* Wiley, New York, 2000.

[57] C. Kittel. *Introduction to Solid State Physics, Seventh Edition.* John Wiley & Sons, New York, 1996.

[58] O. Kohmoto. Effective demagnetizing factors in ferromagnetic resonance equations. *J. Magn. Magn. Mat.*, 262:280–288, 2003.

[59] H. Suhl. Ferromagnetic resonance in nickel ferrite between one and two kilomegacycles. *Phys. Rev.*, 97:555–557, 1955.

[60] X. Liu and J.K. Furdyna. Ferromagnetic resonance in $Ga_{1-x}Mn_xAs$ dilute magnetic semiconductors. *J. Phys.: Cond. Matter*, 18:R245, 2006.

[61] W. Platow, A. N. Anisimov, G. L. Dunifer, M. Farle, and K. Baberschke. Correlations between ferromagnetic-resonance linewidths and sample quality in the study of metallic ultrathin films. *Phys. Rev. B*, 58:5611–5621, 1998.

[62] C. Chappert, K. Le Dang, P. Beauvillain, H. Hurdequint, and D. Renard. Ferromagnetic resonance studies of very thin cobalt films on a gold substrate. *Phys. Rev. B*, 34:3192–3197, 1986.

[63] B. A. Calhoun. Magnetic and electric properties of magnetite at low temperatures. *Phys. Rev.*, 94:1577–1585, 1954.

[64] C. Lai, P. Huang, Y. Wang, and R. T. Huang. Room-temperature growth of epitaxial FeO films by ion beam deposition. *J. Appl. Phys.*, 95:7222, 2004.

[65] J. J. Krebs, D. M. Lind, and S. D. Berry. Ferromagnetic resonance and spin anisotropy in iron oxide thin films and iron oxide/nickel oxide superlattices. *J. Appl. Phys.*, 73:6457–6459, 1993.

[66] S. K. Arora, R. G. S. Sofin, A. Nolan, and I. V. Shvets. Antiphase boundaries induced exchange coupling in epitaxial Fe_3O_4 thin films. *J. Magn. Magn. Mat.*, 286:463, 2005.

[67] Y. Zhou, C. McEvoy, R. Ramos, and I. V. Shvets. The magnetic and magnetoresistance properties of ultrathin magnetite films grown on MgO substrate. *J. Appl. Phys.*, 99:08J111, 2006.

[68] G. M. Smith, J. C. G. Lesurf, R. H. Mitchell, and P. C. Riedi. Quasi-optical cw mm-wave electron spin resonance spectrometer. *Rev. Sci. Instr.*, 69:3924–3937, 1998.

[69] J. O. Rantschler, R. D. McMichael, A. Castillo, A. J. Shapiro, Jr. W. F. Egelhoff, B. B. Maranville, D. Pulugurtha, A. P. Chen, and L. M. Connors. Effect of 3d, 4d, and 5d transition metal doping on damping in permalloy thin films. *J. Appl. Phys.*, 101:033911, 2007.

[70] V. Seshu Bai, S. M. Bhagat, R. Krishnan, and M. Seddat. Ferromagnetic resonance in sputtered $Co_{100-x}Cu_x$ composite films. *J. Magn. Magn. Mat.*, 147:97–100, 1995.

[71] R. Naik, C. Kota, J. S. Payson, and G. L. Dunifer. Ferromagnetic-resonance studies of epitaxial Ni, Co, and Fe films grown on Cu(100)/Si(100). *Phys. Rev. B*, 48:1008, 1993.

[72] B. Heinrich, S. T. Purcell, J. R. Dutcher, K. B. Urqhart, J. F. Cochran, and A. S. Arrott. Structural and magnetic properties of ultrathin Ni/Fe bilayers grown epitaxially on Ag(001). *Phys. Rev. B*, 38:12879, 1988.

[73] M. Farle, Y. Henry, and K. Ounadjela. Magnetic anisotropy of epitaxial Co/Mn superlattices: An angular-dependent ferromagnetic resonance study. *Phys. Rev. B*, 53:11562–11567, 1996.

[74] R. Arias and D. L. Mills. Extrinsic contributions to the ferromagnetic resonance response of ultrathin films. *Phys Rev. B*, 60:7395, 1999.

[75] S. Sugahara and M. Tanaka. Tunneling magnetoresistance in fully epitaxial MnAs/AlAs/MnAs ferromagnetic tunnel junctions grown on vicinal GaAs (111) b substrates. *Appl. Phys. Lett.*, 80:1969, 2002.

[76] B. Degroote, M. Major, J. Meersschaut, J. Dekoster, and G. Langouche. Conservation of uniaxial symmetry in Fe/Ag multilayers grown on stepped Ag(001). *Surf. Sci.*, 482-485:1090, 2001.

[77] D. Zhao, F. Liu, D. L. Huber, and M. G. Lagally. Step-induced magnetic-hysteresis anisotropy in ferromagnetic thin films. *J. Appl. Phys.*, 91:3150, 2002.

[78] Y. Z. Wu, C. Won, and Z.Q. Qiu. Magnetic uniaxial anisotropy of Fe films grown on vicinal Ag (001). *Phys. Rev. B*, 65:184419, 2002.

[79] R. K. Kawakami, E. J. Escorcia-Aparicio, and Z. Q. Qiu. Symmetry-induced magnetic anisotropy in Fe films grown on stepped Ag (001). *Phys. Rev. Lett.*, 77:2570, 1996.

[80] T. Leeb, M. Brockmann, F. Bensch, S. Miethaner, and G. Bayreuther. In-plane magnetic anisotropies in Fe films on vicinal Ag (001) and Au (001) surfaces. *J. Appl. Phys*, 85:4964, 1999.

[81] J. Chen and J. L. Erskine. Surface-step-induced magnetic anisotropy in thin epitaxial Fe films on W(001). *Phys. Rev. Lett.*, 68:1212, 1992.

[82] J. Choi, Z. Q. Qiu, J. Pearson, J. S. Jiang, Dongqi Li, and S. D. Bader. Magnetic anisotropy of epitaxial Fe films grown on curved W (001) with a graded step density. *Phys. Rev. B*, 57:R12713, 1998.

[83] V. Usov, S. Murphy, and I. V. Shvets. Study of in-plane magnetic anisotropy of ultrathin epitaxial Fe films grown on vicinal Mo (110) surface. *J. Appl. Phys.*, 95:7312, 2004.

[84] D. M. Engebreston, J. Berezovsky, J. P. Park, L. C. Chen, C. J. Palmstrom, and P. A. Crowell. Time-domain ferromagnetic resonance in epitaxial thin films. *J. Appl. Phys.*, 91:8040, 2002.

[85] A. Berger, U. Linke, and H. P. Oepen. Symmetry-induced uniaxial anisotropy in ultrathin epitaxial cobalt films grown on Cu (1 1 13). *Phys. Rev. Lett.*, 68:839, 1992.

[86] B. B. Maranville, A. L. Shapiro, and F. Hellman. Miscut-angle dependence of perpendicular magnetic anisotropy in thin epitaxial CoPt films grown on vicinal MgO. *Appl. Phys. Lett.*, 81:517, 2002.

[87] Par M. Louis Neel. Anisotropie superficielle et surstructures d'orientation magntique. *J. Phys. Rad*, 4:15, 1954.

[88] Y. X. Lu, J. S. Claydon, Y. B. Xu, S. M. Thompson, K. Wilson, and G. van der Laan. Epitaxial growth and magnetic properties of half-metallic Fe_3O_4 on GaAs(100). *Phys. Rev. B*, 70:233304, Dec 2004.

[89] I. P. Krug, F. U. Hillebrecht, M. W. Haverkort, A. Tanaka, L. H. Tjeng, H. Gomonay, A. Fraile-Rodríguez, F. Nolting, S. Cramm, and C. M. Schneider. Impact of interface orientation on magnetic coupling in highly ordered systems: A case study of the low-indexed Fe_3O_4/NiO interfaces. *Phys. Rev. B*, 78(6):064427, Aug 2008.

[90] T. Schmitte, K. Theis-Brohl, H. Zabel V. Leiner, S. Kirsch, and A. Carl. Magneto-optical study of the magnetization reversal process of Fe nanowires. *J. Phys. Cond. Matter*, 14:7525–7538, 2002.

[91] B. Borca, O.Fruchart, Ph. David, A. Rousseau, and C. Meyer. Kinetic self-organization of trenched templates for the fabrication of versatile ferromagnetic nanowires. *Appl. Phys. Lett.*, 90:142507, 2007.